5-2008

Vibration Analysis of Piezoelectric Microcantilever Sensors

Amin Salehi-khojin
Clemson University, asalehi@clemson.edu

VIBRATION ANALYSIS OF PIEZOELECTRIC MICROCANTILEVER SENSORS

A Dissertation
Presented to
the Graduate School of
Clemson University

In Partial Fulfillment
of the Requirements for the Degree
Doctor of Philosophy
Mechanical Engineering

---

by
Amin Salehi-Khojin

Accepted by:
Dr. Nader Jalili, Committee Chair
Dr. Paul F. Joseph
Dr. Mohammad Daqaq
Dr. Alexey Vertegel

ABSTRACT

The main objective of this dissertation is to comprehensively analyze vibration characteristics of microcantilever-based sensors with application to ultra small mass detection and low dimensional materials characterization. The first part of this work focuses on theoretical developments and experimental verification of piezoelectric microcantilevers, commercially named Active Probes®, which are extensively used in most today's advanced Atomic Force Microscopy (AFM) systems. Due to special geometry and configuration of Active Probes®, especially multiple jump discontinuities in their cross-section, a general and comprehensive framework is introduced for forced vibration and modal analysis of discontinuous flexible beams. More specifically, a general formulation is obtained for the characteristics matrix using both boundary and continuity conditions. The formulation is then reduced to the special case of Active Probes® with intentional geometrical discontinuities. Results obtained from experiment are compared with the commonly used uniform beam model as well as the proposed discontinuous beam model. It is demonstrated that a significant enhancement on sensing accuracy of Active Probes® can be achieved using the proposed discontinuous beam model compared to a uniform model when a multiple-mode operation is desired.

In the second part of this dissertation, a comprehensive dynamic model is proposed for vector Piezoforce Microscopy (PFM) system under applied electrical loading. In general, PFM is considered as a suspended microcantilever beam with a tip mass in contact with a piezoelectric material. The material properties are expressed in two forms; Kelvin-Voigt model for viscoelstic representation of the material and

piezoelectric force acting on the tip as a result of response of material to applied electric field. Since the application of bias voltage to the tip results in the surface displacement in both normal and in-plane directions, the microcantilever is considered to vibrate in all three directions with coupled transversal/longitudinal and lateral/torsional motions. In this respect, it is demonstrated that the PFM system can be governed by a set of partial differential equations along with non-homogeneous and coupled boundary conditions. Using the method of assumed modes, the governing ordinary differential equations of the system and its state-space representation are derived under applied external voltage. The formulation is then reduced to vertical PFM, in which low dimensional viscoelestic and piezoelectric properties of periodically poled lithium niobate (PPLN) material can be detected. For this purpose, the experimental and theoretical frequency responses along with a minimization strategy for the percentage of modeling error are utilized to obtain optimal spring constant of PPLN. Finally, the step input responses of experiment and theory are used to estimate the piezoelectric and damping coefficients of PPLN.

Overall in this dissertation, a precise dynamic model is developed for piezoelectric microcantilever for ultra small mass detection purpose. This model can also be utilized in AFM systems to replace laser-based detection mechanism with other alternative transductions. Moreover, a comprehensive model is proposed for PFM system to simultaneously detect low dimensional viscoelastic and piezoelectric properties of materials. This model can also be utilized for data storage purpose in ferroelectric materials.

DEDICATION

I dedicate this to the spirits of my dear father who has been watching and guiding me from above, and to my lovely Mom whose unconditional love and sacrifices have made me the person I am today.

ACKNOWLEDMENTS

I gratefully acknowledge my committee members, Dr. Nader Jalili, Dr. Mohammad Daqaq, Dr. Paul Joseph, and Dr. Alexey Vertegel for their insightful guidance and patience. Thank you Dr. Jalili. You have been more than an advisor, you have been a friend. Your passion for research and willingness to help were the reasons that I exceeded in research as much as I did.

Thanks are due to my past and current members of my research group, Dr. Nima Mahmoodi, Saeid Bashash, Reza Saeidpour Azar, Mahmood Reza Hosseini, and Calvin Bradely. Thank you for all the useful discussions and all the laughs. I am specifically thankful to my dear friends, Saeid Bashash, and Behrang Asadi for all the great memories. I appreciate all the indispensable help of the staff of the Department of Mechanical Engineering.

Special thanks go to my family for their continuous guidance, love, and support. I would have never gotten to this point in my life without the love and support of my sister, Sima, her husband, Dr. Reza Bashirzadeh, and my brother, Rahmatollah. Also, I would have probably not had the opportunity to pursue my PhD without the help and support of my dear friends, Dr. Mohammad Mahinfalah and his dear wife.

I greatly appreciate the financial support of National Science Foundation (NSF) and NASA during my PhD program, and more importantly I thank God for giving me the privilege to be useful to the academic society.

TABLE OF CONTENTS

Page

Table of Contents (Continued)

Page

Table of Contents (Continued)

Page

LIST OF TABLES

LIST OF FIGURES

List of Figures (Continued)

List of Figures (Continued)

List of Figures (Continued)

Figure Page

CHAPTER ONE

MOTIVATION AND PROBLEM STATEMENT

1.1. Motivation

Microcantilever beams with their structural flexibility, sensitivity to atomic and molecular forces, and ultra-fast responsiveness have recently attracted widespread attention in a variety of applications including, but not limited to, atomic force and friction microscopy, piezoresponse force microscopy, biomass sensing, thermal scanning microscopy, and MEMS switches. Their extreme sensitivity and ultra-fast responsiveness can be largely attributed to their extremely small size, and the recent efforts devoted into making much smaller cantilevers.

Due to small scale displacement and motion of microcantilever in the aforementioned applications, a comprehensive vibration analysis and experimental characterization of these systems play a key role when accurate measurement is needed. In this respect, the shape and geometry of microcantilever as well as tip-sample interaction should be accurately considered in the dynamic and vibration analysis of the whole system.

1.2. Problem Statement

The objective of this work is to study vibration analysis of microcantilever-based sensors (MSC) for; (a) ultra small mass detection applications utilizing piezoelectric microcantilever (commercially so-called Active Probes®), and (b) materials

characterization by means of piezoresponse force microscopy (PFM). The common feature is the piezoelectric properties of materials which is used as a source of beam's MCS actuation or material stimulation.

(a) Piezoelectric Microcantilevers (Commercially Called Active Probes®)

In recent years, a new generation of microcantilevers so-called "Active Probes" has been introduced and received great attention due to its unique configuration (see Figure 1.1). The probe is covered by a piezoelectric layer on the top surface. This layer is utilized as a potential source of actuation, or as an alternative transduction for the laser interferometer in the next-generation laserless AFMs. The Active Probes® consist of a silicon beam partially covered with a ZnO piezoelectric layer which acts as a source of actuation. To increase the sensitivity of the probe, the tip zone of the probe is designed narrower than the body (see Figure 1.1). Current modeling practices call for a uniform cantilever beam without considering the intentional jump discontinuities associated with the piezoelectric layer attachment and the microcantilever cross-sectional step.

In order to investigate the effect of discontinuities on the dynamic response and modal characterization of Active Probes®, this problem has been generalized to a flexible Euler-Bernoulli beam with multiple jumps in the cross section. For this purpose, the entire length of beam is partitioned into uniform segments between any two successive discontinuity points. A closed-form formulation is then derived for the beam vibration characteristics matrix based on the boundary conditions and the continuity conditions applied at the partitioned points. This matrix is particularly used to find beam natural frequencies and mode shapes. The governing equations of motion and their state-space

representation are then derived for the beam under a distributed dynamic loading. To clarify the implementation of the proposed method, a beam with two stepped discontinuities in the cross section is studied, and numerical simulations are provided to demonstrate the mode shapes and frequency response of beam for different stepped values. Results indicate that the added mass and stiffness significantly affects the mode shapes and natural frequencies, particularly in the modes that the thicker part covers the extremum points of the mode shapes.

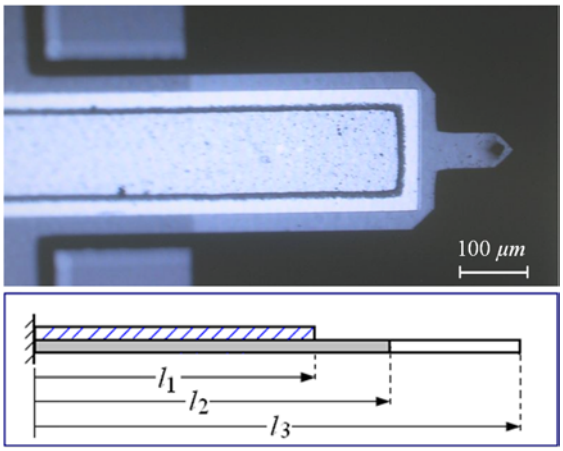

Figure 1.1. piezoelectrically-driven microcantilever (Active Probe®) beam with cross-sectional discontinuity.

The proposed model is then applied for the special case of Active Probe® with only three cross-sectional discontinuities. Using the pin-force model for the electromechanical coupling of piezoelectric layer, forced motion analysis of the system is carried out. An experimental setup consisting of a commercial Active Probe® from Veeco and a state-of-the-art microsystem analyzer, the MSA-400 from Polytec, for non-contact vibration measurement is developed to verify the theoretical derivations. Using a parameter

estimation technique based on minimizing the percentage of modeling error, optimal values of system parameters are identified. Mode shapes and modal frequency response of system for the first three modes obtained from the proposed model are compared with those obtained from the experiment and commonly used theory for uniform beams. Results indicate that the uniform beam model fails to accurately predict the actual system response in multiple-mode operation, while the proposed discontinuous beam model demonstrates good agreement with the experimental data. Such novel modeling framework could pave the pathway to the development of next-generation laserless Atomic Force Microscopy (AFM) systems used in variety of imaging and nanomanipulation applications. Furthermore, such detailed modeling and exact sensing framework can serve as an attractive attention to bulky laser-based or limited piezoresistive-based MCS.

(b) Piezoresponse Force Microscopy (PFM)

On the other hand, microcantilevers have been employed in PFM system. The PFM functions based on applied external bias electrical field between a rear electrode on the sample and a conducting AFM tip. The periodic bias voltage induces local piezoelectric vibration which can be detected by AFM tip. These vibrations depend on the orientation of polarization vector, and arise due to converse piezoelectric effect. In order to utilize PFM for quantifying a wide range of piezoelectric materials, a comprehensive, yet straightforward analytical theory is required. In this study, we aim at acquiring a new dynamic modeling framework for a vector PFM system. For this purpose, PFM is modeled as a suspended microcantilever beam with a tip mass. The microcantilever is

considered to vibrate in all three directions while subjected to the bias voltage. The mechanical properties of sample are divided into viscoelastic and piezoelectric parts. The viscpoelastic part is modeled as a spring and damper in the longitudinal, transversal and lateral directions, while the piezoelectric part is replaced with resistive forces acting at the end of microcantilever. It is shown that there is a geometrical coupling between transversal/longitudinal and lateral/torsional vibration of microcantilever. Moreover, assuming friction between AFM tip and sample, another coupling effect is also taken into account. The PFM system is then modeled as a set of partial differential equations (PDE) along with non-homogeneous and coupled boundary conditions. A general formulation is derived for the mode shape, frequency response, and state-space representation of system. Finally, for the proof of the concept, the obtained model is applied for a special case of vertical PFM. The results obtained from theory are used along with experimental data to identify the spring constant, damping coefficient, and piezoelectric properties of the Periodically Poled Lithium Niobate (PPLN) material. In this regard, a parameter estimation technique based on minimizing the percentage of modeling error is utilized to obtain the optimal values of materials.

1.3. Overview of the Dissertation

The dissertation is organized as follow: In Section 2, the principle of operation for MCS and microcantilever-based integrated systems are presented. In Section 3, modal analysis and forced vibration of flexible Euler-Bernoulli beam with multiple cross-sectional discontinuities are studied. Section 4 expresses modeling and experimental vibration analysis of microcantilever Active Probe® . In Section 5, vibration analysis of

vector PFM with coupled motion is studied, and finally Section 6 presents a procedure for measuring low dimensional properties of piezoelectric material utilizing vertical PFM.

CHAPTER TWO

PRINCIPLE OF OPERATION FOR MICROCANTILEVER BASED SENSORS

2.1. Introduction

In the recent years, MCS have been steadily gaining popularity in many scientific applications due to their potential as a platform for the development of large verity of sensors. There have been a number of research works in this field for biological [1-9], chemical [10-18], physical [19-20], and rheological [21] applications. It has been shown that microcantilever-based sensing technology can be useful in developing "artificial noses" which have the potential of detecting a wide variety of biochemical agents for many applications [22]. This sensing platform can prove to be ideal for real-time, *in situ* sensing with very high sensitivity and significant reduction in the cost [23].

The main feature of MCS is transducing the mechanical deflection of the cantilever arising from external field into detectable signals. The MCS are able to detect differences in the applied force in the order of a pico-newton and displacement at level of an Angstrom with a response time on the order of milliseconds. MCS have been shown to display much higher absolute sensitivity compared to other available sensors such as quartz crystal microbalances [24], surface acoustic wave devices [25], acoustic plate mode devices [26], thickness shear mode resonataor [27] and flexural plate wave ossilators [26]. This extreme sensitivity of MCS can be largely attributed to their

extremely small size and the recent research efforts devoted into making much smaller cantilevers.

Typical microcantilever beams have thicknesses of a few micrometers, widths of few tens of micrometers and lengths from tens to hundreds of micrometer (see Figure 2.1). Their sizes and shapes depend on the type of application and sensitivity is progressively making way to even smaller nanocantilevers. Microcantilever are commonly fabricated from silicon/silicon nitride, although microcantilevers have also been fabricated from polymers [24] and used in sensing applications [29]. They are fabricated using conventional thin film processing techniques which include thin layer deposition, photolithographic pattering, etching and surface/bulk micromachining. Such fabrication process could result in high precision, low cost and good reproducibility of microcantilevers.

In summary, the advantages of using microcantilever beam for sensing can be itemized as follows: (i) It offers an improvement in precision and reliability as well as decrease in the overall dimensions; (ii) It is the simplest MEMS that can be mass produced; (iii) It can easily be incorporated on integrated circuits with readout techniques, and finally; (iv) It can be heated and cooled within microseconds, which is advantageous when utilized in reversal molecular adsorption utilized in rapid detection techniques.

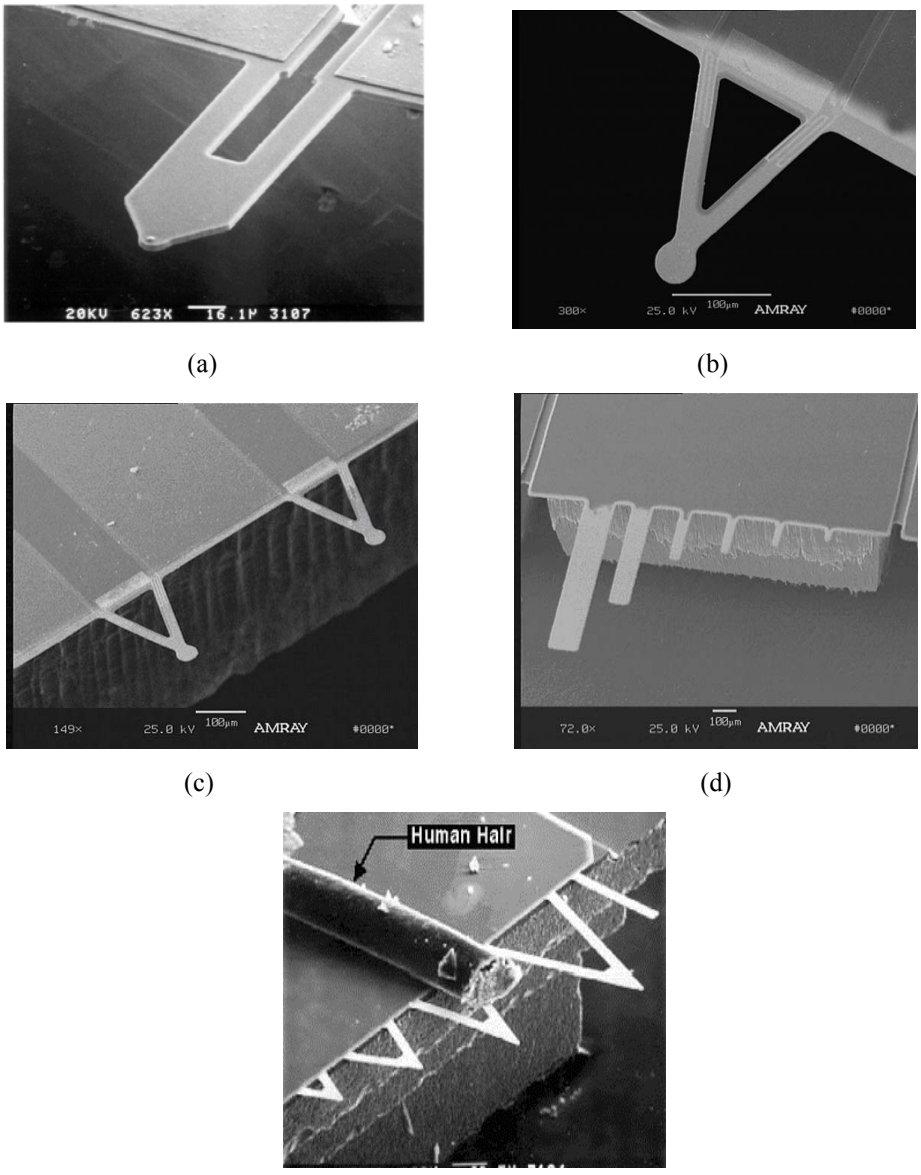

Figure 2.1. (a and b): Microcantilever beams of different shape, (c and d): microcantilever arrays, and (e): comparison of microcantilever beam size with a human hair [30].

In order to highlight the importance of MCS in MEMS and nanotechnology, a review of conceptual design and recent developments in this field is presented in this study in the following format. Section 2.2 describes the principle of operation for MCS. Section 2.3 presents the mathematical modeling for static and dynamic operation modes of MCS.

Section 2.4 explains the principle of operation for microcantilever based integrated systems and Section 2.5 introduces different types of transducers utilized in MCS.

2.2. MCS Principle of Operation

MCS can be operated in two different modes, static and dynamic modes. In the static mode, if an external force is applied to a beam, the extent of deflection is proportional to the type of loading, spring constant, modulus of elasticity and dimensions, and any change in the system parameters for a given condition can results in the deflection of the beam. This forms the basis of the static mode of operation for the MCS. In this respect, presence of external force or matter particles on a microcantilever beam affects its loading, and therefore changes the deflection by a small but detectable amount. However, in the dynamic mode, the shift in the resonance frequency of microcantilever as result of aforementioned parameters is used as sensing element. In this approach, four parameters of resonance frequency, amplitude, deflection and quality factor (which is a measure of the resonance peak bandwidth) can be measured simultaneously [31]. Moreover, by measuring the damping in the system more information can be accessed which is impossible to detect them in the static mode.

In MCS, the matter particle can be a biological or chemical agent. Depending on the type of application, microcantilever beam surface can be processed by depositing an analyte layer which selectively adsorbs matter particles of specific types of biochemical agents. In the static mode, the adsorbed species on the microcantilever surface induces variation in the surface stress. Since the surface stress changes only on one side of the sensor, a differential stress between the top and bottom surfaces results in bending of the

beam. However, in the dynamic mode, the desired species do not have to be adsorbed to only one side of the microcantilever. In this approach, the change in the both surface stress and mass can be simultaneously used as a sensing element. The following section will focus on the mathematical modeling for static and dynamic modes of MSC.

2.3. Static and Dynamic Modes Models

2.3.1. Static Deflection Model:

In general, when matter particles are absorbed on the one surface of microcantilever, the intermolecular forces arise on that side, and induce differential surface stress $\Delta S = S_1 - S_2$ which generates a bending moment along its length (see Figure 2.2). For the case of elastically deflection of microcantilever with rectangular shape, the bending moment is given by [[32]:

$$M = \Delta S \frac{bh}{2} \tag{2.1}$$

where b is the beam width and h is its thickness. If the length of the microcantilever is assumed to be much larger than its width, the curvature of the beam for the small deflection can be expressed as a function of effective modulus $\hat{E}$ and bending moment M and moment of inertia I as follow:

$$\frac{d^2 w}{dx^2} = \frac{M}{\hat{E}I} \tag{2.2}$$

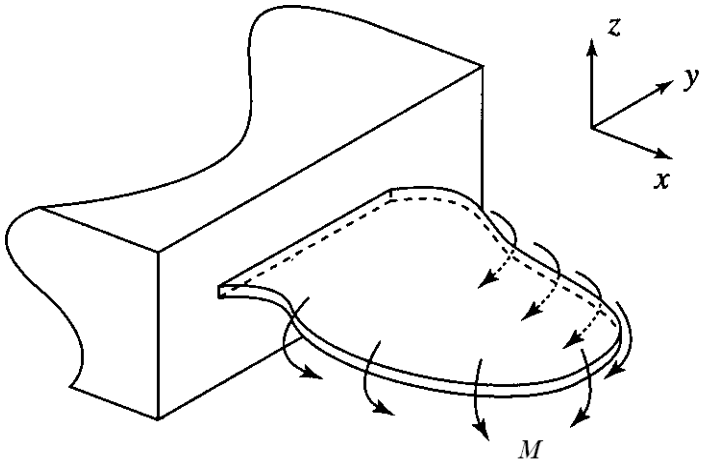

Figure 2.2. The schematic of induced bending moment due to surface stress in a cantilever with arbitrary geometry [33].

where $\hat{E} = E/(1-\upsilon^2)$, E and υ are the respective Young's modulus of elasticity and Poisson's ratio of the beam and $I = bh^3/12$. Substituting Eq. (2.1) into Eq. (2.2), the Stoney's equation for the radius of curvature of deflected microcantilever due to adsorption can be expressed as:

$$\frac{1}{\mathrm{R}} = \frac{6(1-\upsilon)}{Eh^2}\Delta S \tag{2.3}$$

where R is the radius of curvature, reciprocal of which is equal to $\frac{d^2w}{dx^2}$ (for small amplitude vibrations), and ΔS is the differential surface stress. Using a geometrical approach, a relationship between the microcantilever displacement and differential surface stress can be expressed as:

$$z = \frac{3L^2(1-\upsilon)}{Eh^2}\Delta S \tag{2.4}$$

Applying the first law of thermodynamic, the surface stress and surface free energy can be related with the following equation:

$$S = \gamma + \frac{\partial \gamma}{\partial \varepsilon} \tag{2.5}$$

Due to very small bending, the contribution made by the surface strain effects ($\partial \varepsilon = \delta A / A$) can be neglected and the change in surface stress variations S can be equated entirely to changes in free surface energy γ.

In the derivation of Stoney's equation (Eq. (2.3)) it is assumed that the plate bends with the uniform curvature which is valid for the unrestrained conditions at all edges of plate. However, in MCS this condition is not satisfied and the effect of specified displacement at its clamped end should be taken into account. Figure 2.3 depicts the decomposition of such problem into the free plate problem (Stoney's problem) plus correction problem arising from specified displacement at the clamped end of microcantilever [33].

Considering all these points, Sader proposed a more accurate equation for the deflection of a given point of a rectangular microcantilever due to the effect of surface stress as follow [33]:

$$\begin{aligned} w(X,Y) = \Omega L^2 \{ & X^2 + 2\upsilon X [\frac{1}{\tau_1} + \frac{1}{\tau_2}](\frac{b}{L}) - [\frac{1}{12} + 2\upsilon(\frac{1}{\tau_1^2} + \frac{1}{\tau_2^2} + \frac{1}{\tau_1 \tau_2}) - \\ & \sum_{i=1}^{2} d_i (\frac{1}{12} + \frac{2\upsilon}{\tau_i^2}) \exp(-\tau_i X L w^{-1})](\frac{b}{L})^2 + Y^2 [1 - d_i \exp(-\tau_i X L w^{-1})] \} \end{aligned} \tag{2.6}$$

where

$$X = xL^{-1},\ Y = yL^{-1},\ d_i = \frac{\tau_{3-i}}{(\tau_{3-i} - \tau_i)},\ \Omega = \frac{(\Delta S)h}{[4D(1+\upsilon)]},\ D = \frac{Et^3}{[12(1-\upsilon^2)]} \text{ and}$$

$$\tau_i = 2\sqrt{3}[5(1-\upsilon + (-1)^i \sqrt{10(1-\upsilon)(2-3\upsilon)}]$$

The similar formulation was obtained for V-shaped microcantilever [34].

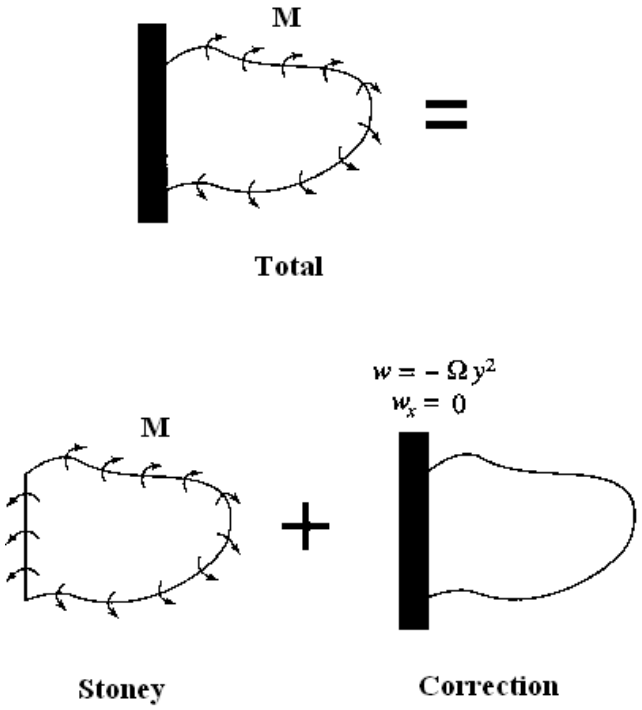

Figure 2.3. Decomposition of MCS problem into Stoney and correction problems [33].

Up to now, the mathematical models presented in this section for the deflection of microcantilever were developed based on the energy transferred between surface free energy and bending elastic energy of the beam. However, the mechanism of bending of the microcantilever can be explained in terms of atomic and elastic energy. In this approach, the interactive potential of adsorbate and adsorbent (microcantilever surface) atoms are related to the beam curvature. It is assumes that bending of the microcantilever

is a result of interactions of the first layer of surface atoms with the adsorbate atoms (see Figure 2.4). According to Lennard-Jones formula, the potential of interaction in the attached film can be given by [35]:

$$P(r) = -\frac{A}{r^6} + \frac{B}{r^{12}} \tag{2.7}$$

where A and B are Lennard-Jones constants chosen to fit the physical properties of the beam material and r is the spacing between the atoms. Assuming the uniform curvature along the microcantilever and neglecting the role of the second and higher layers of atom on the deflection of beam, the potential energy in the near surface layer of atoms based on Lennard-Jones potential can be expressed in terms of beam curvature as follow [35]:

$$U_s = -\frac{A}{(b-z)^6} + \frac{B}{(b-z)^{12}} + 2\left[\frac{-A}{(\frac{1}{4}(b-z)^2 + a^2)^3} + \frac{B}{(\frac{1}{4}(b-z)^2 + a^2)^6}\right] \tag{2.8}$$

where $z = \frac{b}{R}(c+a)$ can be obtained from the geometry shown in Figure (2.4(a)). On the other hand, the elastic bending potential U_b over atomic length b can also be given by [35]:

$$U_b = \frac{1}{2} EI(\frac{1}{R})^2 b \tag{2.9}$$

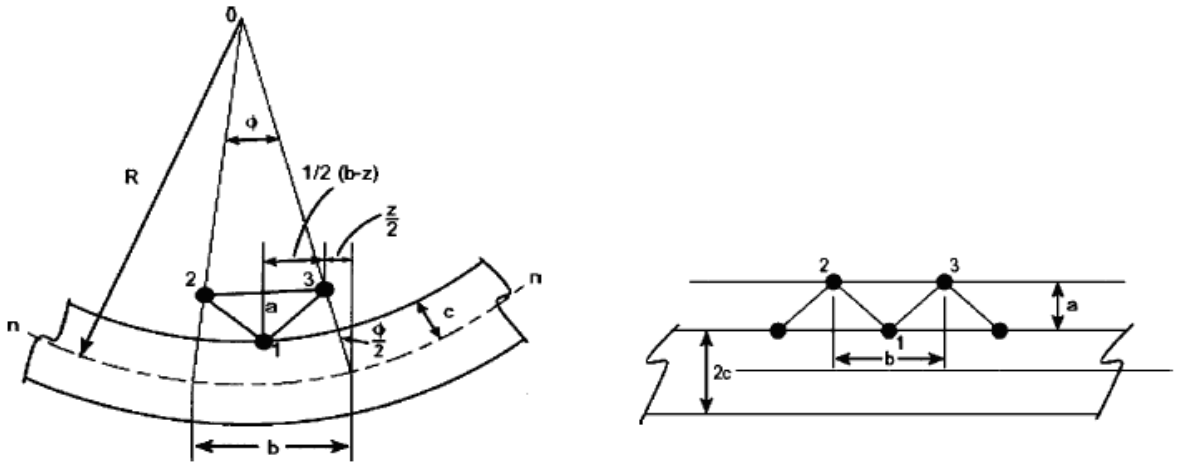

(a) **(b)**

Figure 2.4. (a) Curvature of beam over distance *b*, and (b) schematic of near surface layer of atoms [35].

In order to obtain an expression for the curvature of the beam due to molecular interactions, the relative minimum of the total potential $U = U_s + U_b$ with respect to the curvature can be expressed as [35]:

$$\frac{EI}{c^2}\left(\frac{c}{R}\right) = \frac{\frac{A}{b^7}6\left(1+\frac{a}{c}\right)}{\left[1-\frac{c}{R}\left(1+\frac{a}{c}\right)\right]^7} - \frac{\frac{B}{b^{13}}12\left(1+\frac{a}{c}\right)}{\left[1-\frac{c}{R}\left(1+\frac{a}{c}\right)\right]^{13}} + 2\frac{\frac{A}{b^7}\frac{3}{2}\left[1-\frac{c}{R}\left(1+\frac{a}{c}\right)\right]\left(1+\frac{a}{c}\right)}{\left[\frac{1}{4}\left[1-\frac{c}{R}\left(1+\frac{a}{c}\right)\right]^2+\left(\frac{a}{b}\right)^2\right]^4} - 2\frac{\frac{B}{b^{13}}3\left[1-\frac{c}{R}\left(1+\frac{a}{c}\right)\right]\left(1+\frac{a}{c}\right)}{\left[\frac{1}{4}\left[1-\frac{c}{R}\left(1+\frac{a}{c}\right)\right]^2+\left(\frac{a}{b}\right)^2\right]^7} \tag{2.10}$$

The values of $(\frac{c}{R})$ which satisfy Eq. (2.10) is the curvature of microcantilever. Applying simple trigonometry, the transverse deflection of the end of the microcantilever can be obtained as (see Figure 2.5):

$$\delta = R(1 - \cos\theta) \tag{2.11}$$

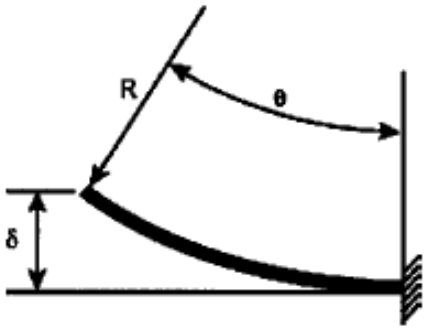

Figure 2.5. Calculation of beam deflection [35].

2.3.2. Dynamic Models

As mentioned earlier, in the dynamic mode, the changes in the resonant frequency of the microcantilever is used to detect the effect of surface stress and added mass to the system. In this respect, the dynamic mode of MCS has been developed based on 1D oscillator approach and/or a flat thin homogenous beam. The following subsection will focus on the detail of each approach. Moreover, the effect of distributed and concentrated added mass on the resonant frequency and the mass sensitivity of MCS will be discussed in more detail.

2.3.2.1. String Model Approximation of Microcantilever

This model approximates the microcantilever beam by a taut string, as shown in Figure 2.6, [36]. In general, if the microcantilever is modeled as a 1D oscillator, the natural frequency can be given by [32]:

$$f = \frac{1}{2\pi}\sqrt{\frac{K}{m_b}} \tag{2.12}$$

where K is the spring constant and $m_b = nm_{beam}$ is the effective beam mass with m_{beam} being it's actual mass and n being a geometric parameter accounting for the non point-mass distribution. n has a typical value of 0.24 for a rectangular microcantilever beam.

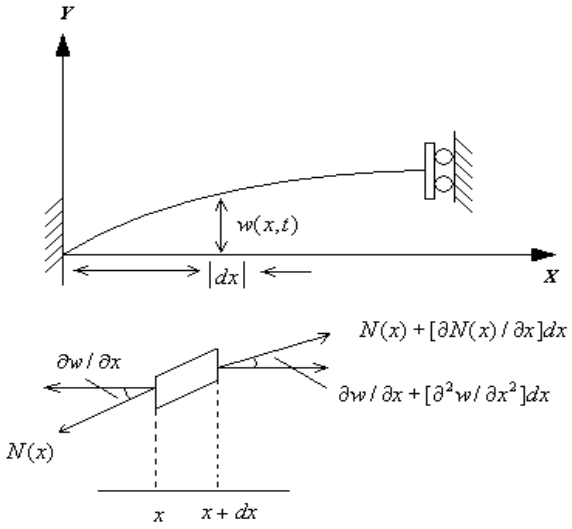

Figure 2.6. Approximation of microcantilever beam by a taut string [36].

Presence of mass on the microcantilever surface results in the generation of differential surface stress. This changes the spring constant, which also changes the resonant frequency given by:

$$f_\delta = \frac{1}{2\pi}\sqrt{\frac{K + \delta K}{m_b + n\delta m}} \tag{2.13}$$

where δK is the change in the spring constant attributed to adsorption induced surface stress and δm being the added mass.

If the microcantilever is approximated by a taut string, stretched under tension N, the equation of transverse free vibration can be given by [36]:

$$N\frac{\partial^2 w(x,t)}{\partial x^2}+\rho A\frac{\partial^2 w(x,t)}{\partial t^2}=0 \tag{2.14}$$

where $w(x,t)$ is the transversal deflection, x is the distance along the length, t is the time, ρ is the volumetric mass density, and A is the area of cross section. Moreover, the axial force generated by surface stress can be expressed as [32]:

$$N=(S_1+S_2)L \tag{2.15}$$

where S_1 and S_2 are the surface stresses on the two sides of the microcantilever, and L is the microcantilever length. The propagation speed of the transverse wave can then be given by:

$$C=\sqrt{\frac{N}{\rho A}}=\sqrt{\frac{NL}{m_b}} \tag{2.16}$$

Since $C=f\lambda$, where λ is the fundamental mode transverse wavelength equal to $4L$, the resonance frequency due to surface stresses can be written as [37]:

$$f=\frac{1}{\lambda}\sqrt{\frac{NL}{nm_{beam}}}=\frac{1}{4}\sqrt{\frac{S_1+S_2}{nm_{beam}}} \tag{2.17}$$

From equation (2.17) and taking into account equation (2.14) it could be concluded that [37]:

$$K_s=\frac{\pi^2}{4}(S_1+S_2) \tag{2.18}$$

where K_s is the spring constant due to the surface stress. Hence,

$$\delta K = \frac{\pi^2}{4}(\delta S_1 + \delta S_2) \tag{2.19}$$

where δK is the change in the spring constant attributed to adsorption induced surface stress and δS_1 and δS_2 are the changes in the surface stresses on each side of the microcantilever due to the mass adsorption.

It has been shown that if adsorption is localized (end loading), the change in resonance frequency due to change in spring constant can be neglected. If the spring constant K is given by [23]:

$$K = \frac{Ebh^3}{4L^3} \tag{2.20}$$

with E being the Young's modulus of elasticity for the microcantilever beam material and b, h, and L being width, thickness and length of the beam, respectively, then, the resonance frequency f of the microcantilever beam can be given by [23]:

$$f = \frac{h}{2\pi(0.98)L^2}\sqrt{\frac{E}{\rho}} = \frac{1}{2\pi}\sqrt{\frac{K}{m_{eq}}} \tag{2.21}$$

where m_{eq} is the equivalent mass consisting of mass of microcantilever beam and adsorbed mass. If m_d is the added mass at the end of the microcantilever beam, then $m_{eq} = nm_d + m_b$.

Moreover, the shifted resonance frequency f_δ can be given by [23]:

$$f_\delta = \frac{1}{2\pi}\sqrt{\frac{Ebh^3}{4nL^3(m_d + \rho bhL)}} \tag{2.22}$$

The adsorbed mass δm can then be determined from the change in the resonance frequency as:

$$\frac{f^2 - f_\delta^{\,2}}{f^2} = \frac{\delta m}{m} \tag{2.23}$$

If the mass sensitivity for a sensor is defined as the fractional change in the resonant frequency with addition of mass;

$$S_m = \lim_{\Delta m \to 0} \frac{1}{f}\frac{\Delta f}{\Delta m} = \frac{1}{f}\frac{df}{dm}, \quad \Delta m = \frac{\delta m}{A_s} \tag{2.24}$$

where A_s is the active area of the sensor, the expression for the mass sensitivity of MCS can be obtained as [23]:

$$S_m = \begin{cases} \dfrac{1}{\rho h} & \text{for distributed load} \\ \dfrac{-\zeta_1}{2\rho(\zeta_1 h_{\mathrm{d}} + 0.24h)} & \text{for end load} \end{cases} \tag{2.25}$$

where ζ_1 and h_d are the fractional area coverage and thickness of the deposited mass at the end loaded microcantilever beam. The smallest detectable change in the resonator mass per unit area mas, $\Delta m_{\min}$, can be expressed as [38]:

$$\Delta m_{\min} = 8\sqrt{\frac{2\pi^5 K K_B T B}{f^5 Q}} \tag{2.26}$$

where K is the spring constant, K_B is the Boltzmann constant (1.38×10^{-23} J/K), T is the absolute temperature, B is the bandwidth of measurement, f is the resonant frequency of the microcantilever beam and Q is the quality factor.

A few points need to be noted. (i) If a microcantilever beam is end-loaded, then the resonant frequency decreases with increase in the load; (ii) If the microcantilever beam is uniformly loaded, then the resonance frequency actually *increases* with increase in the load; (iii) Sensitivity increases with decrease in spring constant, however decrease in spring constant results in increase in the thermal noise; (iv) Longer microcantilevers with smaller spring constants are attractive for bending mode; (v) Sensitivity will increase with increase in the resonance frequency and the resonance frequency will increase with decrease in size, and finally; (vi) If the same microcantilever is to be used for sensing in both static and dynamic modes, then a compromise needs to be made with regards to the dimensions and sensitivity of each mode.

2.3.2.2. Beam Model Approximation

If the microcantilever is modeled as a flat thin homogenous cantilever beam, (see Figure 2.7), then the governing differential equation for negligible surface stress is can be given by:

$$\hat{E}I\frac{\partial^4 w(x,t)}{\partial x^4}+(\rho A+\chi)\frac{\partial^2 w(x,t)}{\partial t^2}+C\frac{\partial w(x,t)}{\partial t}=q(x,t) \tag{2.27}$$

where $\hat{E}=E/(1-\upsilon^2)$ is the apparent Young's modulus of the beam with E being the Young's modulus of the beam and υ being the Poisson's ratio. $I=bh^3/12$ is the cross-sectional area moment of inertia, w is the linear transverse deflection, x is the distance measured along the length of the beam, t is time, ρ is the volumetric mass density of the material, A is the area of beam cross section, C is the damping coefficient per unit

length per unit velocity, χ is the additional mass per unit length and $q(x,t)$ represents the external load per unit length.

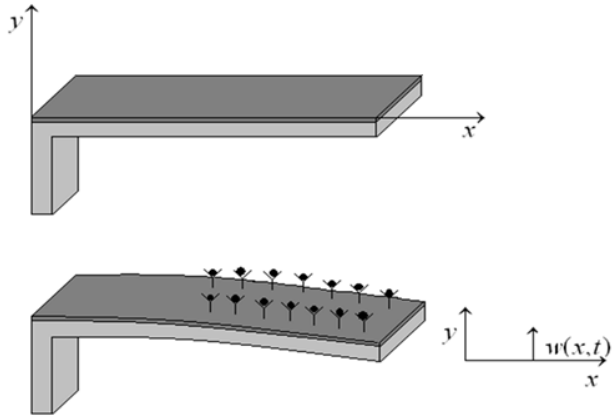

Figure 2.7. Microcantilever modeled as prismatic beam.

Assuming variables are separable, i.e., $w(x,t) = W(x)T(t)$, the equation of motion for the case of free vibration can be represented by:

$$\frac{\hat{E}I}{\rho A + \chi}\frac{\frac{d^4W(x)}{dx^4}}{W(x)} = -\frac{C}{\rho A + \chi}\frac{\frac{dT(t)}{dt}}{T(t)} - \frac{\frac{d^2T(t)}{dt^2}}{T(t)} = \omega_0^2 = const. \tag{2.28}$$

The equation governing the time-function, $T(t)$ can be written as:

$$\frac{d^2T(t)}{dt^2} + \frac{C}{\rho A + \chi}\frac{dT(t)}{dt} + {\omega_0}^2 T(t) = 0 \tag{2.29}$$

which is a general second order ordinary differential equation of the form

$$\frac{d^2T(t)}{dt^2} + 2\zeta\omega_0\frac{dT(t)}{dt} + {\omega_0}^2 T(t) = 0 \tag{2.30}$$

and the solution being given as:

$$T(t) = Be^{-\zeta\omega_0 t}\sin(\omega_d t + \varphi) \tag{2.31}$$

with B and φ are constants determined using initial conditions and $\omega_d = \omega_n\sqrt{1-\zeta^2}$ is the damped natural frequency. The equation governing spatial-function $W(x)$ can be also written as:

$$\frac{\hat{E}I}{\rho A+\chi}\frac{d^4W(x)}{dx^4} - {\omega_0}^2 W(x) = 0 \tag{2.32}$$

with the solution being given by:

$$W(x) = c_1\cos(\frac{\lambda}{L}x) + c_2\sin(\frac{\lambda}{L}x) + c_3\cosh(\frac{\lambda}{L}x) + c_4\sinh(\frac{\lambda}{L}x) \tag{2.33}$$

where constants c_1, c_2, c_3 and c_4 are to be determined from the boundary conditions:

$$W(0) = 0, \quad \left.\frac{dW(x)}{dx}\right|_{x=0} = 0, \quad \left.\frac{d^2W(x)}{dx^2}\right|_{x=0} = 0, \quad \left.\frac{dW^3(x)}{dx^3}\right|_{x=L} = 0 \tag{2.34}$$

and,

$$(\frac{\lambda}{L})^4 = \frac{\rho A{\omega_0}^2}{\hat{E}I} \tag{2.35}$$

The first two boundary conditions are due to the fact that one end of the beam is clamped. The third excludes any bending moment at the free end of the cantilever and the fourth excludes any shear force. The characteristic equation can then be given:

$$\cos\lambda\cosh\lambda = -1 \tag{2.36}$$

with discrete values of λ for the first four modes given by λ_0=1.875, λ_1= 4.69, λ_2=7.68 and λ_3=11.00. Substitution of these parameters into Eq. (2.35), the resonance frequency of a clamped-free beam with rectangular cross section can be given as [38]:

$$\omega_{a,0} = 2\pi f_{a,0} = \frac{\lambda_a{}^2 h}{\sqrt{12}L^2}\sqrt{\frac{E}{\rho(1-\nu^2)+\chi}} = \frac{\lambda_a{}^2}{L^2}\sqrt{\frac{\hat{E}I}{\rho A+\chi}},\ a = 0,\ 1,\ 2,\ \ldots \tag{2.37}$$

where $\omega_{a,0}$ is the resonance frequency in the undamped case ($\zeta = 0$).

If the magnitude of surface stress is sufficiently great, the axial normal force distributed along the microcantilever length arising from the surface stress has to be considered in the Eq. (2.27). Assuming non-unifrom distribution of normal axial force, the governing equation for undamped of motion of microcantilever case can be given by [36]:

$$EI\frac{\partial^4 w(x,t)}{\partial x^4} - \frac{\partial}{\partial x}(N\frac{\partial w(x,t)}{\partial x}) + \rho A\frac{\partial^2 w(x,t)}{\partial t^2} = 0 \tag{2.38}$$

where the axial force N varies along the microcantilever and can be given by (see Figure 2.8):

$$N = SLf(x),\ \text{ with } f(x) = \begin{cases} \frac{x_2}{L} - \frac{x_1}{L} & 0 < x < x_1 \\ \frac{x_2}{L} - \frac{x}{L} & x_1 < x < x_2 \end{cases} \tag{2.39}$$

and S is the stress on the microcantilever surface. The microcantilever frequency can then be expressed as [36]:

$$f = \frac{9}{2\pi}\sqrt{\frac{2}{13}}\sqrt{1+\beta(\frac{x_1}{L},\frac{x_2}{L})\Pi_1}\sqrt{\frac{EI}{m_{beam}L^4}} \tag{2.40}$$

where,

$$\beta = 5\left[\frac{1}{12}(\frac{x}{L})^4 - \frac{1}{10}(\frac{x}{L})^5 + \frac{1}{18}(\frac{x}{L})^6 - \frac{1}{63}(\frac{x}{L})^7 + \frac{1}{504}(\frac{x}{L})^8\right]_{x_1}^{x_2} \tag{2.41}$$

and $\Pi_1 = \frac{SL^3}{EI}$ is a dimensionless quantity which gives the ratio of surface stress S to the elastic bending force EI/L^3. In general, the natural frequency can be represented as [36]:

$$f = \frac{1}{2\pi}\sqrt{\frac{K + K_n}{m_{eq}}} \tag{2.42}$$

where K_n is a function of $\beta(x_1/L, x_2/L)$ and the dimensionless quantity Π_1. The surface sensitivity of this model can be given by [36]:

$$\alpha = \lim_{\Delta s \to 0} \frac{1}{f}\frac{\Delta f}{\Delta s} = \frac{1}{f}\frac{df}{ds} \tag{2.43}$$

which is similar to the expression of mass sensitivity, and can be further expressed as [36]:

$$\alpha = \frac{1}{16(\Pi_1 + \frac{1}{8}S)} \tag{2.44}$$

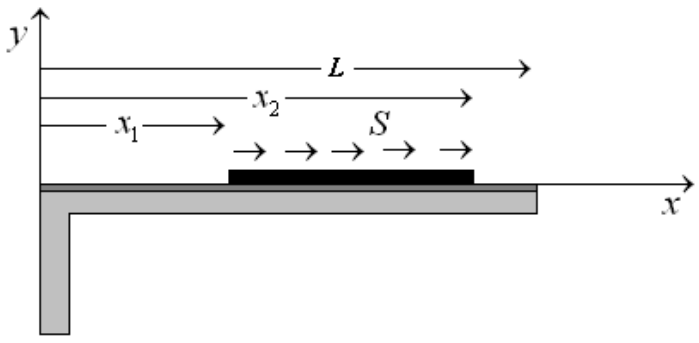

Figure 2.8. Microcantilever modeled as a beam with non-uniform stresses.

Finally, Mcfarland *et al.* [40] have developed a general model for entirely coated microcantilever with a layer of molecules. In their model, the change in the i^{th} frequency of microcantilever is expressed as a function of adsorbed mass, increased stiffness due to the change in the thickness and surface stress as follow:

$$f_i = \frac{\left(\lambda_i \Delta S\right)^2}{2\pi\sqrt{3}} \sqrt{\frac{k}{m_{beam} + \delta m} + \frac{3E_{ads} I_{ads}}{L^3 (m_{beam} + \delta m)}} \tag{2.45}$$

where E_{ads} and I_{ads} are the stiffness and moment of inertia of adsorbed layer, respectively, λ_i are roots of characteristic equation expressed in Eq. (2.36), and $k = \frac{3EI}{L^3}$. Moreover, the effect of damping due to viscous environment on the frequency is given by [40]:

$$\frac{f_i^D}{f_i^v} = \left(1 + \frac{\pi \rho_D b}{4 \rho h}\right)^{-1/2} \tag{2.46}$$

where f_i^D and f_i^v are the i^{th} resonant frequency of the microcantilever in the viscous and vacuum environment, respectively, and ρ_D and ρ are the density of environment and beam, respectively.

2.4. Microcantilever Based Integrated Systems Principle of Operation

Use of microcantilever beams as a platform for new sensing technology emerged from the research of sensing probes in Scanning Force microscopy (SFM) [41, 42] and in particular Atomic Force microscopy (AFM), [43]. SFM encompasses a family of

techniques that provide measurement of surface topography and surface properties at the atomic scale. The SFM principle has widespread applicability, typically in new probe-based techniques (e.g., piezoresponse force microscopy), force measurements (e.g., atomic force microscopy) and imaging applications (e.g., scanning tunneling microscopy). Due to important contribution of this area, this section is aimed at providing an overview of principle of operation and recent developments in SFM techniques.

2.4.1. Atomic Force Microscopy (AFM)

AFM is one of the most power tools for determining the topography of a surface at subnanometer resolution. It enables for direct measurement of specific interaction between two kinds of molecules which can be employed in biology, biomaterial, polymer, electronics and many other applications. A typical AFM consist of an integrated microcantilever-tip assembly interacting with the sample surface, a piezoelectric (PZT) actuator, a displacement detector and a feedback electronic. As the microcantilever scans the sample, the interatomic attractive and repulsive forces between sample and tip leads to the deflection of microcantilever. This deflection can be measured by optical detection technique which detects any nanoscale motion of microcantilever. Utilizing a feedback mechanism based on the output signals of transducer, the tip and sample are maintained in the constant separation distance by moving the PZT scanner in the vertical (Z) direction. With an instrumental sensitivity on the order of 0.1 A°, the topography of the surface and intermolecular force between tip and sample can be detected [44]. The schematic of basic AFM are depicted in Figure 2.9.

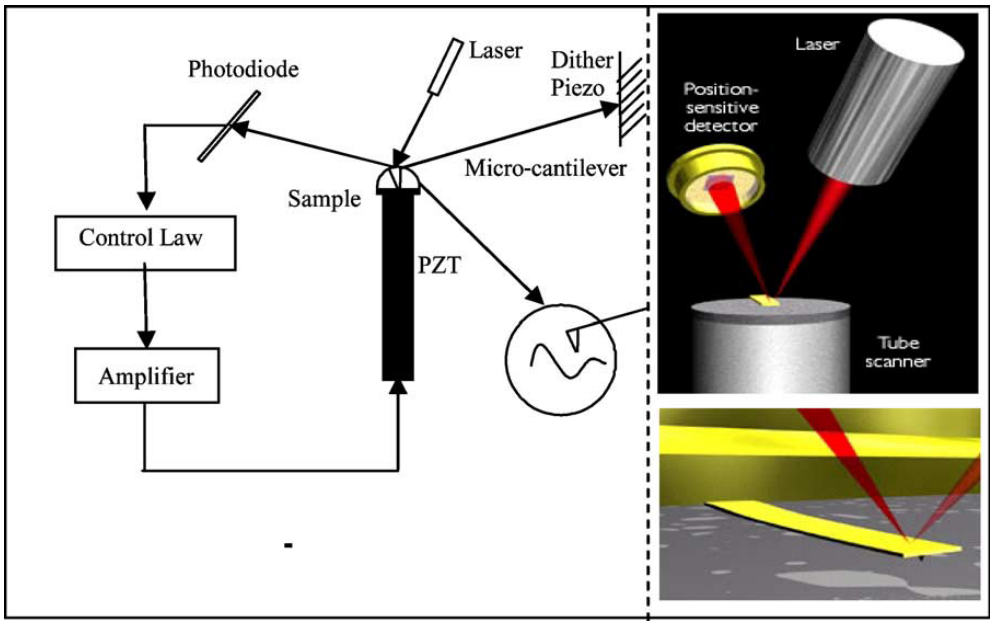

Figure 2.9. Schematic of basic AFM operation (left), real micro-cantilever and components (right) [44].

Typically, AFM system is operated in three open-loop modes: (i) non-contact mode, (ii) contact mode, and (iii) tapping mode. In the non-contact mode, the separation distance between tip and sample is defined in the attractive region in the Lennard-Jones potential curve (see Figure 2.10) and the frequency of oscillating microcantilever due to attractive van der Waals forces acting between tip and sample is detected [45]. In the contact mode, the tip is moving at closer distance to the sample, and the change in the frequency of cantilever due to the repulsive force between tip and sample is measured (see Figure 2.10) [46]. And in tapping mode, the microcantilever is vibrated at or near its resonance frequency through applying a base motion by PZT actuator. The amplitude of vibration is maintained in a constant level and the change in the oscillating amplitude as a result of change in the topography of the surface through a feedback mechanism is used

to measure the interatomic force or topography of the scanned surface [47]. The schematic of operation modes in all three modes are shown in Figure 2.11.

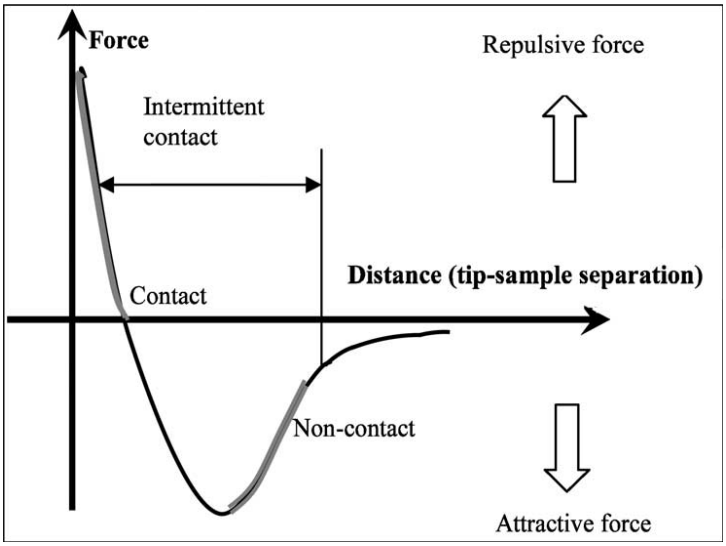

Figure 2.10. Interatomic force variation versus distance between AFM tip and sample [44].

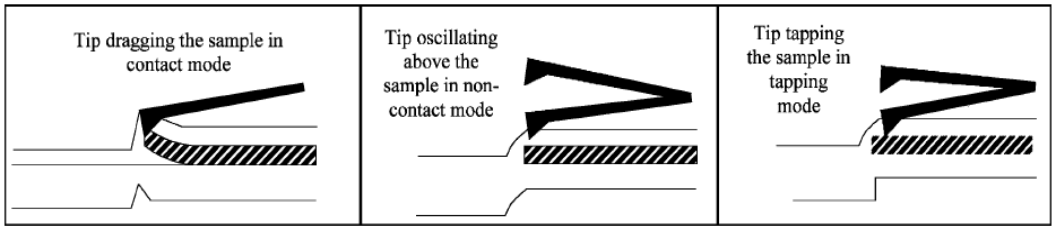

Figure 2.11. Contact mode (left), non-contact mode (middle) and tapping mode (right) [44].

In order to utilize AFM for imaging with chemical sensitivity and measure the interactions between functional groups, the tip and sample must be modified with well-defined molecular monolayers. Through varying the head group of monolayers, it is possible to study different types of interactions between two kinds of molecules. Numbers of studies have been reported the successful methods for covalently modifying

the Au coated Si_3O_4 tips with functionalized organic molecules, and measured adhesive forces between modified tip and samples [48]. Figure 2.12 illustrates the scheme for selectively chemical interaction of tip and sample substrate.

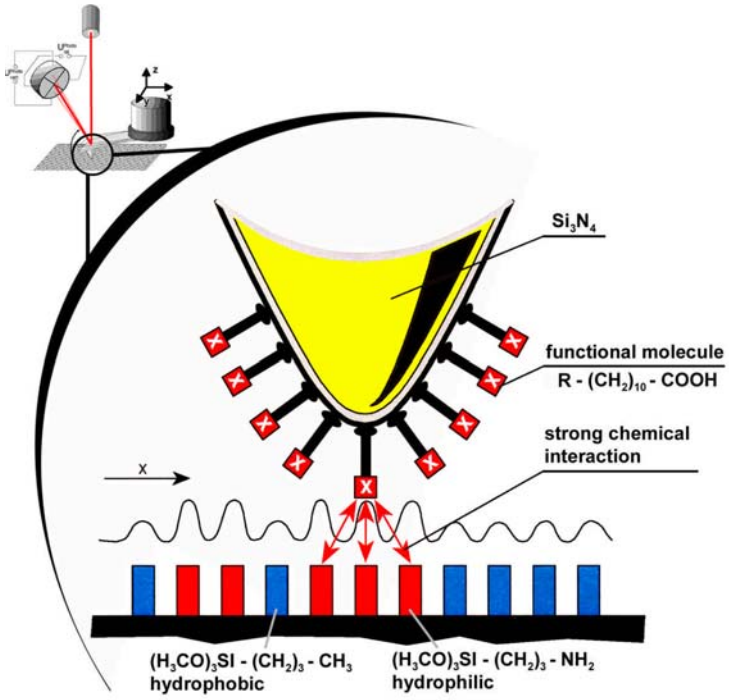

Figure 2.12. Scheme for chemical modification of tip and sample [www.nanocraft.de].

2.4.2. Friction Force Microscopy

Typically, friction force microscopy (FFM) is a contact mode AFM which is used to measure both lateral (friction) force as well as vertical force. While in the AFM system microcantilever oscillates in the vertical direction, in FFM it may experience torsional vibration in addition to the vertical bending. The torsion of microcantilever originates from the friction force between tip and sample which applies a lateral force to the tip results in the lateral motion and rotation of the beam as shown in Figure 2.13. Employing

a quadrant photo detector (see Figure 2.14) to measure the tilt angle of microcantilever from its resting point with considering the rotational stiffness of cantilever, the friction force between tip and sample can be measured.

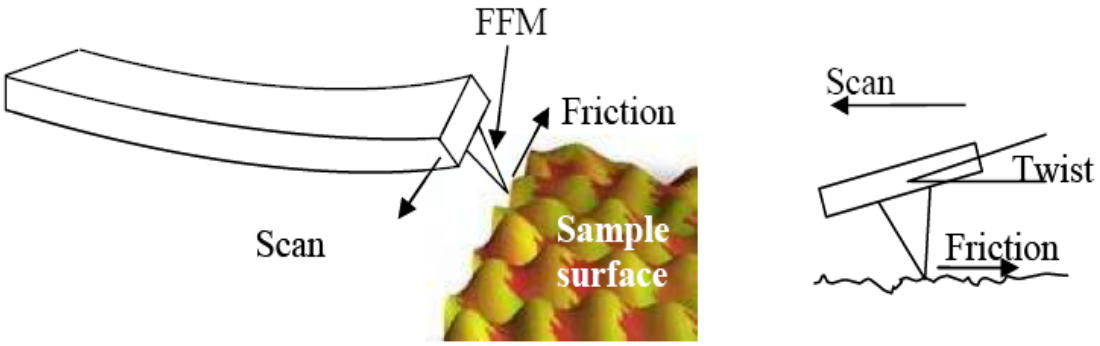

Figure 2.13. (a) Schematic operation of FFM, and (b) twist of the FFM tip, [49].

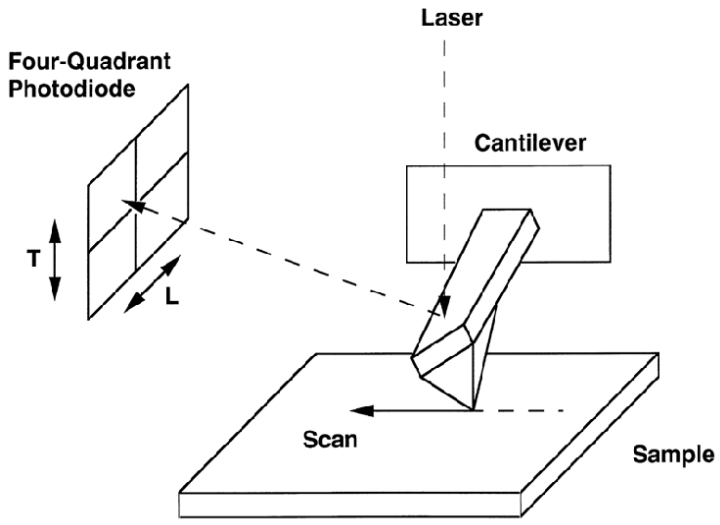

Figure 2.14. Schematic of a quadrant photo detector employed in the FFM.

Recently, an alternative approach has been introduced to measure friction force via FFM system [50]. It was shown that considering nonlinearity in the motion of FFM, the vertical vibration of cantilever is coupled to its torsional motion. As the lateral force applies to the microcantilever, due to coupling effect, the rotation of microcantilever can affect the vertical oscillation of cantilever. Therefore, the change in the rotation of cantilever and consequently the friction force can be indirectly measured from the change in the resonant frequency of vertical vibration of coupled motion. In this approach, the differences in the resonant frequency of vertical vibration in coupled motion and single vertical motion are related to the friction force between tip and sample.

2.4.3. Piezoresponse Force Microscopy

Piezoelectric materials are one of the most promising classes of materials which have attracted a lot of attention since their discovery in 1880-1881. Many works have been carried out in developing applications for piezoelectric materials with efforts devoted into the development of these materials for implementation in the microelectromechanical system (MEMS) [51-53]. In order to use piezoelectric materials in microstructure design, the investigation of size effect of these materials in low dimensional structures is a crucial factor. It was shown that at microscopic level, the materials cannot preserve their macroscopic properties and a significant deviation in the properties of materials can be observed when compared to bulk materials [54]. In this respect, characterization of material in these scales requires different technique than those utilized for bulk materials. Recently, rapid development in scanning probe microscopy (SPM)-based techniques and in particular piezoresponse force microscopy (PFM) has attracted widespread attention as

a primary technique for nondestructive characterization of piezoelectric materials in the scale of grain [55-58].

PFM functions based on application of a periodic bias external electrical field between a rear electrode on the sample and a conducting AFM tip. The periodic bias voltage is $V_{tip} = V_{dc} + V_{ac}Cos(wt)$ in which V_{dc} is DC component of the bias voltage used to measure the static deflection of the microcantilever and $V_{ac}Cos(wt)$ is a small AC voltage which is applied to the tip in order to induce local piezoelectric vibration. The piezoresponse of the surface can be detected as the first harmonic component of bias induced tip deflection $d = d_0 + ACos(wt + \varphi)$. The amplitude of vibration, A, provides information about the piezoelectric coefficients of surface, while the phase of electromechanical response of surface, φ, yields information about the polarization direction of surface [58 and 59]. Figure 2.15 depicts the schematic of surface displacement as a result of applied voltage and microcantilever motion with respect to the piezoelectric domain of sample.

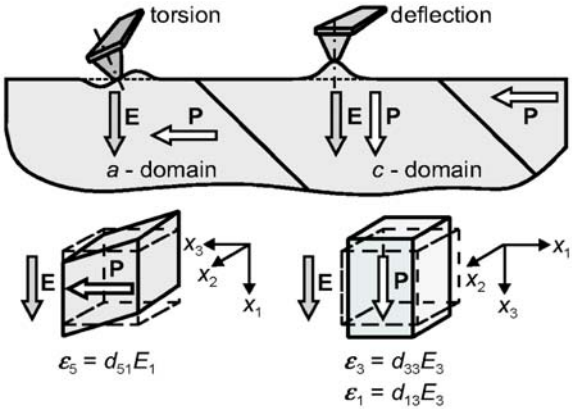

Figure 2.15. The electromechanical response of piezoelectric sample in lateral (left) and vertical (right) displacements [60].

2.5. Methods of Signal Transduction

For MCS which are operated in the static or dynamic modes, the following signal transduction methods have been used to measure the microcantilever frequencies of vibration or static deflections.

2.5.1 Optical Deflection Method

In order to measure the nanomechanical response of microcantilever, the optical laser readout system which provides sub-angstrom resolution is the most widespread method. This technique is based on the laser beam reflected off from the cantilever surface onto a position sensitive photo detector. In this way, any nanoscale motion of cantilever results in the deflection of reflected laser beam and accordingly displacement in the reflected spot on the surface of sensitive photo detector which is calculated using appropriate electronics. In order to detect the lateral and transversal deflection of microcantilever simultaneously, a simple combination of two orthogonal quadrant photo sensitive detectors can be used (Figure 2.16). The difference in light intensities between the upper and lower two quadrants enables to measure the vertical deflection of cantilever, while the difference in the signal intensities between right and left two quadrants gives the lateral deflection [61 and 62]. Other optical deflection methods such as dual fiber optic proximity sensor [63], laser Doppler vibrometry [64], and interferometry [65 and 66] have also been used for this purpose.

The advantage of optical readout technique is the precision of detection in sub-nanometer range. However, the accuracy of this technique due to thermal management issues in the liquid environment still is questionable [67]. Add to this, the conventional

optical techniques are bulky and are not portable, and in some cases the alignment of the system can raise the cost of this technique.

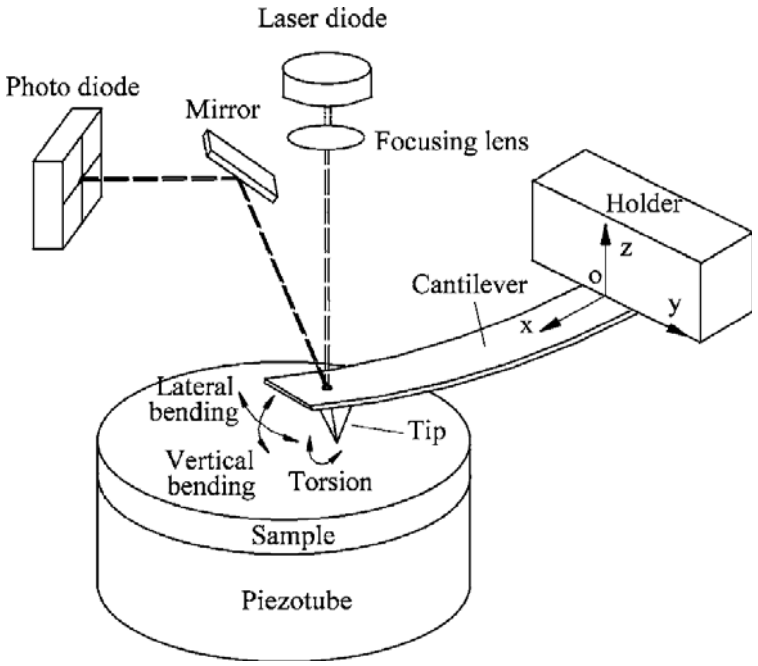

Figure 2.16. The schematic of laser read out technique for combined motion of microcantilever [66].

2.5.2. Piezoresistive-based Measurement

An alternative to the optical readout system is the piezoresistive-based transducer. Piezoresistive detection methods rely on the ability of piezoresistive materials such as doped silicon to change resistivity upon application of stress. The change in the resistivity of piezoresistor can be easily converted into the measurable electrical signals through interface circuits such as Wheatstone bridge circuit [68]. Figure 2.17 depicts the schematic of a two-dimensional piezoresistive cantilever force sensor structure. The four piezoresistors are arranged on the surface of structures such that a pair of them is stress sensing transistors and is located on the surface of cantilever, while another pair is

positioned on the outside of cantilever and is used for compensation in the Wheatstone bridge [69]. The schematic of lateral and vertical circuit of piezeoresitive cantilever sensor are shown in Figure 2.18. The change between these two circuits can be performed through using an appropriate electronic switch [69].

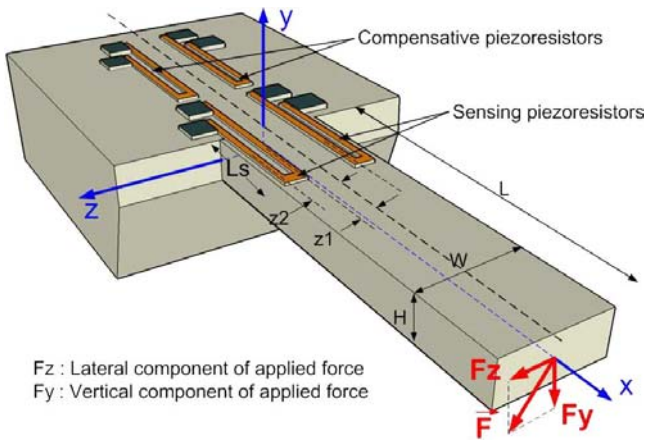

Figure 2.17. Schematic drawing of the two-dimensional piezoresistive force-sensing cantilever [69].

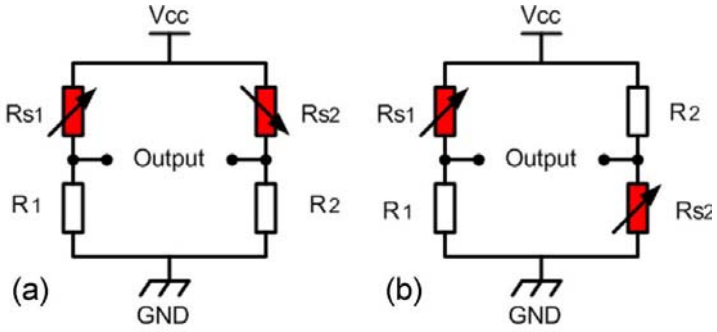

Figure 2.18. Schematic configuration. (a) Lateral force sensing mode. (b) Vertical force sensing mode [69].

When lateral and/or vertical forces are applied to the tip of microcantilever, the resistance change for the piezoresistors in lateral and vertical directions can be respectively expressed as [69]:

$$\frac{\Delta R_l}{R_0} = \frac{1}{L_s}\int_0^{L_s} \frac{-\pi_l F_z (z_1 + z_2)}{2I_y}(L - x)dx = \frac{-\pi_l F_z (z_1 + z_2)}{2I_y}(L - \frac{L_s}{2}) \tag{2.47}$$

$$\frac{\Delta R_v}{R_0} = \frac{1}{L_s}\int_0^{L_s} \frac{-\pi_l H F_y}{2I_z}(L - x)dx = \frac{-\pi_l H F_z}{2I_z}(L - \frac{L_s}{2}) \tag{2.48}$$

where ΔR, R_0, π_l, L_s, L, F_z, F_y, H, z_1, z_2, I_y, I_z denote the resistance change of the piezoresistor, resistance of the zero-stressed piezoresistor, longitudinal piezoresitor coefficient, distance from fixed end of cantilever to the tip of piezoresistor, length of cantilever, lateral applied force, vertical applied force, thickness of cantilever, distance from the lateral neutral plane to the inner half (see Figure 2.19), distance from the lateral neutral plane to the outer half, lateral momentum of inertia, vertical momentum of inertia, respectively.

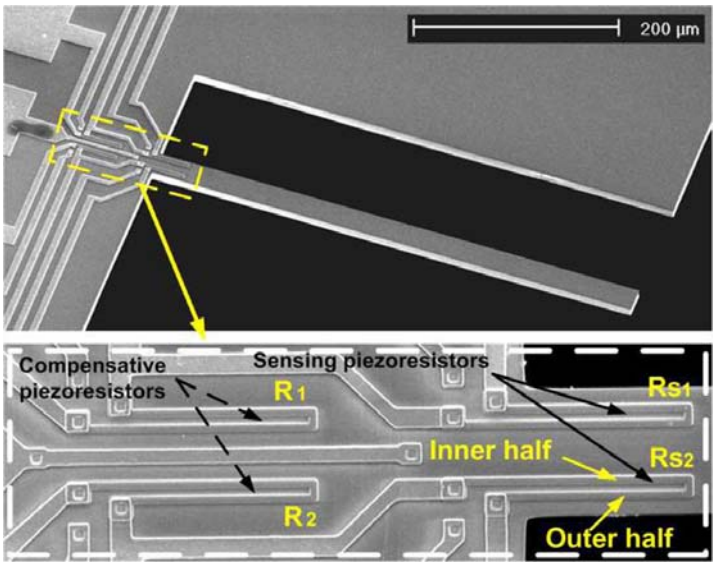

Figure 2.19. SEM image of the two dimensional piezoresistive cantilever sensor [69].

Assuming the resistance value of piezoresistors in Figure 2.19 as

$$R_{S1} = R_0 + \Delta R_l \quad \text{and} \quad R_{S2} = R_0 - \Delta R_l \,, \tag{2.49}$$

then the output voltage in the lateral and vertical directions can be respectively given by [69]

$$V_{out}^{l} = V_{cc} \frac{2\dfrac{\Delta R_l}{R_0}}{4 - \left(\dfrac{\Delta R_l}{R_0}\right)^2} \cong \frac{1}{2}\frac{\Delta R_l}{R_0} V_{cc} \tag{2.50}$$

$$V_{out}^{v} = V_{cc} \frac{1}{\left(\dfrac{2R_0}{\Delta R_v}\right)^2 - 1} \cong \frac{1}{4}\left(\frac{\Delta R_l}{R_0}\right)^2 V_{cc} \tag{2.51}$$

where V_{cc} is the bias voltage.

The above equations indicate that if the magnitude of input bias and output voltages from Wheatstone bridge circuit along with geometry and coefficients of piezoresistors and cantilever are known, the magnitude of applied stress or strain and therefore the deflection of microcantilever can be directly obtained.

2.5.3. Piezoelectric Film Attachment

Piezoelectric detection techniques rely on the ability of piezoelectric materials to induce electric charge when set into vibration. One such method consists of depositing thin film of piezoelectric material such as ZnO on the microcantilever surface [70] (see Figure 2.20). The generated voltage can then be utilized to detect the vertical deflection of microcantilever. In this case, the magnitude of output voltage is proportional to the slope difference of the deflection at two ends of the attached piezoelectric layer [71]:

$$V_S(t) \equiv \frac{E_p h_p d_{31} b}{C_f}\left[\frac{\partial w(x_2,t)}{\partial x} - \frac{\partial w(x_1,t)}{\partial x}\right] \tag{2.52}$$

where V_S, E_p, h_p, d_{31}, b, C_f are the output voltage, Young's modulus, thickness, piezoelectric coefficient, width and capacitive coefficient of piezoelectric sensor attached to the surface of microcantilever. The last term in the right hand side of Eq. (2.52) represents the slope change at both ends of piezoelectric patch layer.

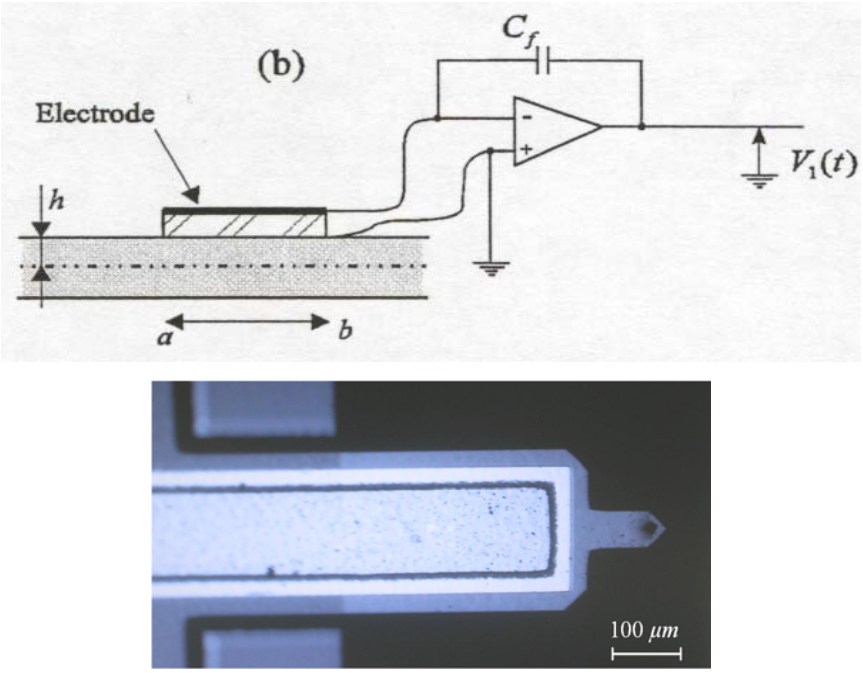

Figure 2.20. The configuration for the piezoelectric cantilever sensor (top), and the piezoelectric cantilever Active Probe (bottom).

Typically, piezoelectric microcantilever can be used as an actuator, sensor and actuator-sensor mode, simultaneously. When they are used as an actuator, they offer an actuation bandwidth of 10 times larger than that of conventional piezotubes [72]. This

advantage of piezoelectric microcantilever actuator over commonly used bulky piezotube actuator makes it a promising candidate to be utilized in next-generation of high speed imaging AFM. On the other hand, when piezoelectric microcantilever is used as a sensor, they offer the sensitivity as much magnitude as of optical sensing techniques [73]. This way, they can be used as an alternative sensor for the bulky laser in AFM system which show some disadvantages in terms of laser alignment in the liquid environment, laser expense and space required for the laser operation. Additionally, it is possible to operate a piezoelectric microcantilever in sensing-actuating mode, simultaneously, by an appropriate electrical circuit which is impossible by other methods. In this line, recently Gurjar and Jalili [74] have used a self sensing strategy to detect ultra small tip mass. A piezoelectric patch layer deposited on the surface of microcantilever was used as a source of actuation, and the same piezoelectric layer was utilized to detect the change in the resonant frequency of the beam as a result of adding mass. They showed that according to this technique, the shift in the resonant frequency due to 10-15g added mass is detectable.

CHAPTER THREE

A GENERAL FRAMEWORK FOR MODAL ANALYSIS AND FORCED VIBRATIONS OF FLEXIBLE EULER BERNOULLI BEAM WITH MUTIPLE CROSS-SECTIONAL DISCONTINIUTIES

3.1. Introduction

Modal analysis and vibration characterization of beam-like structures are of a great importance with widespread applications to structures such as aircraft wings, spacecraft antennas, helicopter blades, robot arms and many other systems. In this respect, numerous studies can be found in literature on the transverse vibration analysis of uniform beams under different boundary conditions. However, in many real applications, the investigation of beams with non-uniform cross-section may provide a realistic distribution of mass and stiffness desired for accurate structural analysis. Particularly, for structures with abrupt changes in cross section, the added mass, stiffness and geometrical discontinuities affect the modal behavior of structure which cannot be neglected.

The work presented here originates from the need for accurate vibration analysis of flexible beams with locally attached piezoelectric layers for precision sensing and control purposes [75]. Figure 3.1(a) depicts a typical flexible uniform beam with an attached piezoelectric layer for actuation and sensing the vibrations. As seen, the attached layer creates jumped non-uniformities in the cross-section which may significantly alter the configuration of beam mode shapes. Since sensor output for transversal motion of beam is proportional to the slope difference of mode shapes at two ends of attachment [75],

applying a uniform beam model may drastically degrade the precision of estimation and consequently vibration control strategies. Figure 3.1(b) depicts a typical configuration of a piezoelectrically-driven microcantilever probe widely utilized in mass sensing and AFM [76]. Due to the presence of piezoelectric actuator/sensor layer, the body of the cantilever is made wider, while in order to increase the sensitivity of tip deflection the cantilever the ending part is made narrower. Therefore, the cantilever has two steps in the cross-section: one small step where the piezoelectric layer ends; and one large step where the cantilever cross-sectional area drops suddenly. Dynamic modeling and vibration analysis of beams with jumps in their cross-section becomes a crucial issue in sensing and imaging enhancement of microcantilever active probes. Moreover, this may be beneficial to many other applications, including analysis of machining processes [77], and design of road and railway bridges [78].

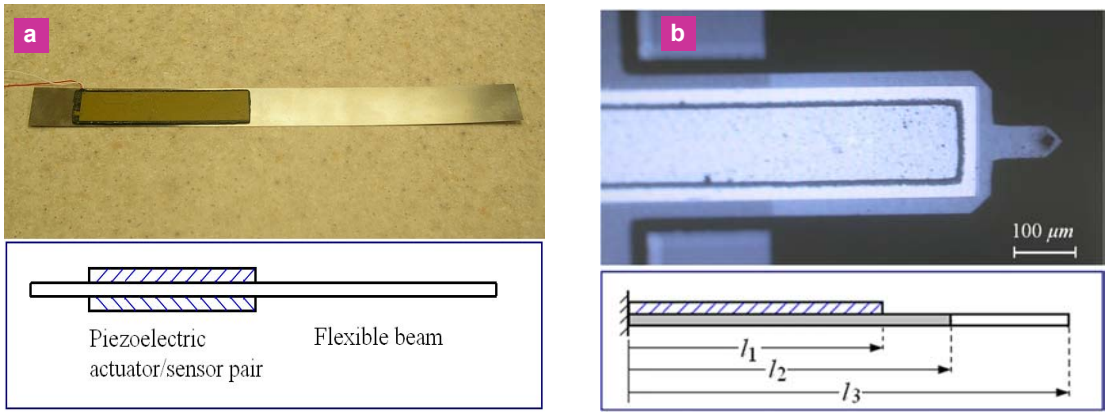

Figure 3.1. Beam configurations with cross-sectional discontinuities: (a) Flexible beam with locally attached piezoelectric actuator/sensor, and (b) piezoelectrically-driven microcantilever beam with cross-sectional discontinuity.

In the last decades, many studies have been reported on the transverse vibration of continuous Euler-Bernoulli beams [79, 80]. However, methods applied for continuous beams cannot be directly used for beams with sudden changes in the cross-section. Partitioning method [76], finite difference approach [81], shear deformation theory [82], and transfer matrices approach [83] have been used to study free vibration of such structures. While bibliography on the free vibration of beams with one step change in the cross-section is extensive [84-89], few studies have been focused on the analysis of beams with multiple jumps [90, 91]. Nevertheless, there is a lack of a straightforward framework for the forced vibration analysis of beam with any arbitrary number of step jumps in the cross section, and under general distributed dynamic loading. Additionally, graphical comparison of beam mode shapes with and without geometrical discontinuities has not been well presented in the literature. Such a demonstration can provide a valuable insight to realize how the dynamic response of beam in the spatial domain varies with respect to the variation of the added mass and stiffness.

The present work is aimed at the forced vibration formulation and analysis of Euler-Bernoulli beams with an arbitrary number of step changes in their cross-section and properties. To obtain beam mode shapes, the entire length of beam is partitioned into the segments between any two successive discontinuity points. As a result, the governing equation of motion is divided into a set of partial differential equations (PDEs) with constant parameters and a set of continuity conditions at stepped points. A general formulation is then derived for the characteristics matrix of beam using boundary and continuity conditions. The natural frequencies of the beam and the parameters of the

modes shapes can be obtained by imposing the non-trivial solution condition on the derived characteristics equation. Finally, using the method of assumed modes, the governing ordinary differential equations (ODEs) of beam and their state-space representation are derived under distributed vertical loading condition.

The rest of this chapter is organized as follows: Sections 3.2 presents the modal analysis and forced vibration formulation of EB beam with multiple cross-sectional discontinuities; Sections 3.3 includes the case study of a beam with two step discontinuities in the cross-section, to numerically and graphically demonstrate the effects of discontinuities; and finally, Section 3.4 presents the concluding remarks.

3.2. Euler-Bernoulli (EB) Beam with Multiple Stepped Discontinuities

Consider an initially straight non-uniform EB beam of length L, with variable cross section $A = A(x)$, variable stiffness $E = E(x)$, and variable moment of inertia $I = I(x)$. Let $x \in [0, L]$ and $t \in [0, \infty)$ be the spatial and time variables, respectively. The governing equation for transverse vibration of beam with variable mass per unit length $m(x)$ and damping coefficient of $c(x)$ subjected to a vertical time varying distributed load $P(x,t)$ is a fourth-order PDE expressed as:

$$\frac{\partial^2}{\partial x^2}\left(E(x)I(x)\frac{\partial^2 w(x,t)}{\partial x^2} \right) + c(x)\frac{\partial w(x,t)}{\partial t} + m(x)\frac{\partial^2 w(x,t)}{\partial t^2} = P(x,t) \tag{3.1}$$

with $w(x,t)$ being the transversal displacement function. In order to obtain natural frequencies and eigenfunctions (mode shapes) of system, the eigenvalue problem

associated with the transversal vibration of beam is obtained by applying free and un-damped conditions to Eq. (3.1) as follows:

$$\frac{\partial^2}{\partial x^2}\left(E(x)I(x)\frac{\partial^2 w(x,t)}{\partial x^2} \right) = -m(x)\frac{\partial^2 w(x,t)}{\partial t^2} \tag{3.2}$$

Let's assume that the solution of Eq. (3.2) is separable in time and space domains,

$$w(x,t) = \phi(x)q(t) \tag{3.3}$$

where $\phi(x)$ denotes the spatial mode shape function and $q(t)$ represents the generalized time-dependent coordinate. Substituting Eq. (3.3) into Eq. (3.2), the eigenvalue equation can be written in the following form of separated time and space equations:

$$\frac{d^2}{dx^2}\left(E(x)I(x)\frac{d^2\phi(x)}{dx^2} \right) / \left(m(x)\phi(x) \right) = -\ddot{q}(t)/q(t) = \omega^2 \tag{3.4}$$

where ω is a constant parameter. The mode shapes are obtained by solving the spatial part of Eq. (3.4) written as:

$$\frac{d^2}{dx^2}\left(E(x)I(x)\frac{d^2\phi(x)}{dx^2} \right) = \omega^2 m(x)\phi(x) \tag{3.5}$$

For a beam with parametric discontinuities (e.g., jump in the moment of inertia or mass distribution) Eq. (3.5) cannot be solved using conventional approaches. An alternative method is to partition the beam into uniform segments between any two successive stepped points and apply the continuity conditions at these points. Therefore, the non-uniform beam is converted to a set of uniform segments constrained through the continuity conditions. The next section discusses this technique in detail and proposes a

framework for dynamic analysis of flexible beams with jumped cross-sectional configuration.

3.2.1. Modal Analysis of Stepped EB Beam

Figure 3.2 illustrates a straight EB beam with arbitrary boundary conditions and N jumped discontinuities in its spatial span. The beam considered in this study has a uniform cross-section at each segment. Hence, Eq. (3.5) can be divided into n uniform equations expressed as:

$$(EI)_n \frac{d^4\phi_n(x)}{dx^4} = \omega^2 m_n \phi_n(x)\ , \quad l_{n\text{-}1} < x < l_n ; \quad n = 1,2,3,...,N;\ l_0 = 0 \tag{3.6}$$

where $\phi_n(x)$, $(EI)_n$, and m_n are mode shapes, flexural stiffness, and mass per unit length of beam at the n^{th} segment, respectively*. Let,

$$\beta_n^4 = \omega^2 \frac{m_n}{(EI)_n} \tag{3.7}$$

Eq. (3.6) can be rewritten in a more recognizable form

$$\frac{d^4\phi_n(x)}{dx^4} - \beta_n^4 \phi_n(x) = 0 \tag{3.8}$$

with the following general solution

$$\phi_n(x) = A_n \sin\beta_n x + B_n \cos\beta_n x + C_n \sinh\beta_n x + D_n \cosh\beta_n x \tag{3.9}$$

* $(\cdot)_n$ denotes the mode shape or parameter value for the n^{th} cross-section, while $(\cdot)^{(r)}$, which will be used later in the dissertation, denotes the mode shape or parameter value of the r^{th} mode; though, ω_r which represents the r^{th} natural frequency is an exception.

where A_n, B_n, C_n and D_n are the constants of integration determined by suitable boundary and continuity conditions. It is to be noted that any conventional boundary conditions can be applied to the beam; however, without the loss of generality, the clamped-free conditions are chosen here for the boundaries. Applying the clamped condition at $x = 0$ requires:

$$\phi_1(0) = \frac{d\phi_1(0)}{dx} = 0^{\dagger} \tag{3.10}$$

Substituting Eq. (3.10) into Eq. (3.9) yields:

$$B_1+D_1=0 \text{ and } A_1+C_1=0 \tag{3.11}$$

On the other hand, the continuity conditions for displacement, slope, bending moment, and shear force of beam at discontinuity locations are given by:

$$\phi_n(l_n) = \phi_{n+1}(l_n) \tag{3.12}$$

$$\frac{d\phi_n(l_n)}{dx} = \frac{d\phi_{n+1}(l_n)}{dx} \tag{3.13}$$

$$(EI)_n \frac{d^2\phi_n(l_n)}{dx^2} = (EI)_{n+1} \frac{d^2\phi_{n+1}(l_n)}{dx^2} \tag{3.14}$$

$$(EI)_n \frac{d^3\phi_n(l_n)}{dx^3} = (EI)_{n+1} \frac{d^3\phi_{n+1}(l_n)}{dx^3} \tag{3.15}$$

† $\frac{d^q\phi(l_n)}{dx^q} \equiv \frac{d^q\phi(x)}{dx^q}\Big|_{x=l_n}$.

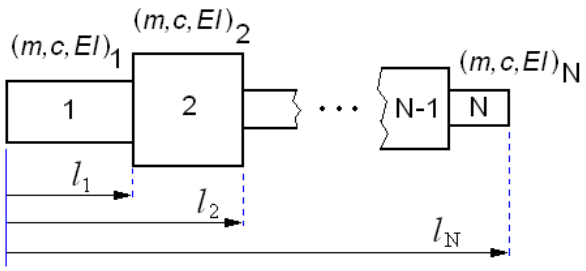

Figure 3.2. EB beam configuration with *N* jumped discontinuities.

Indeed, these conditions are applied at the boundaries of adjacent segments to satisfy the continuity and equilibrium conditions immediately before and after stepped points. Applying conditions (3.12)-(3.15) to Eq. (3.9) results in:

$$\begin{aligned} &A_n \sin\beta_n l_n + B_n \cos\beta_n l_n + C_n \sinh\beta_n l_n + D_n \cosh\beta_n l_n = \\ &A_{n+1} \sin\beta_{n+1} l_n + B_{n+1} \cos\beta_{n+1} l_n + C_{n+1} \sinh\beta_{n+1} l_n + D_{n+1} \cosh\beta_{n+1} l_n \end{aligned} \tag{3.16}$$

$$\begin{aligned} &\beta_n (A_n \cos\beta_n l_n - B_n \sin\beta_n l_n + C_n \cosh\beta_n l_n + D_n \sinh\beta_n l_n) = \\ &\beta_{n+1} (A_{n+1} \cos\beta_{n+1} l_n - B_{n+1} \sin\beta_{n+1} l_n + C_{n+1} \cosh\beta_{n+1} l_n + D_{n+1} \sinh\beta_{n+1} l_n) \end{aligned} \tag{3.17}$$

$$\begin{aligned} &\gamma_n \beta_n^2 (-A_n \sin\beta_n l_n - B_n \cos\beta_n l_n + C_n \sinh\beta_n l_n + D_n \cosh\beta_n l_n) = \\ &\beta_{n+1}^2 (-A_{n+1} \sin\beta_{n+1} l_n - B_{n+1} \cos\beta_{n+1} l_n + C_{n+1} \sinh\beta_{n+1} l_n + D_{n+1} \cosh\beta_{n+1} l_n) \end{aligned} \tag{3.18}$$

$$\begin{aligned} &\gamma_n \beta_n^3 (-A_n \cos\beta_n l_n + B_n \sin\beta_n l_n + C_n \cosh\beta_n l_n + D_n \sinh\beta_n l_n) = \\ &\beta_{n+1}^2 (-A_{n+1} \cos\beta_{n+1} l_n + B_{n+1} \sin\beta_{n+1} l_n + C_{n+1} \cosh\beta_{n+1} l_n + D_{n+1} \sinh\beta_{n+1} l_n) \end{aligned} \tag{3.19}$$

where $\gamma_n = \dfrac{(EI)_n}{(EI)_{n+1}}$.

Finally, the free boundary condition at $x = L = l_N$ requires:

$$\frac{d^2\phi_N(l_N)}{dx^2} = \frac{d^3\phi_N(l_N)}{dx^3} = 0 \tag{3.20}$$

Substituting Eq. (3.20) into Eq. (3.9) yields:

$$\beta_N^2(-A_N \sin\beta_N l_N - B_N \cos\beta_N l_N + C_N \sinh\beta_N l_N + D_N \cosh\beta_N l_N) = 0 \tag{3.21}$$

$$\beta_N^3(-A_N \cos\beta_N l_N + B_N \sin\beta_N l_N + C_N \cosh\beta_N l_N + D_N \sinh\beta_N l_N) = 0 \tag{3.22}$$

Note that β_n's are functions of beam natural frequency with an explicit expression given in Eq. (3.7). Since the natural frequency is independent of segments indices and is considered for the entire length of beam, β_ns of different segments can be interrelated in terms of a single parameter β using Eq. (3.7):

$$\beta_n = \beta\alpha_n \tag{3.23}$$

where

$$\alpha_n = \left(\frac{m_n(EI)_1}{m_1(EI)_n}\right)^{1/4} \tag{3.24}$$

Note that $\alpha_1 = 1$ and thus, $\beta = \beta_1$.

Eqs. (3.11), (3.21) and (3.22) derived from boundary conditions while Eqs. (3.16)-(3.19) are obtained from the continuity conditions form the characteristics matrix equation as:

$$\mathbf{J}_{4N\times 4N}\mathbf{P}_{4N\times 1} = \mathbf{0} \tag{3.25}$$

where **J** is the characteristics matrix and **P** is the vector of mode shape coefficients

$$\mathbf{P} = [A_1\ B_1\ C_1\ D_1\ A_2\ B_2\ C_2\ D_2\ \cdots\ A_N\ B_N\ C_N\ D_N]^{\mathrm{T}}_{1\times 4\mathrm{N}} \tag{3.26}$$

Matrix **J** is constructed based on three sets of equations. The first two rows and last two rows represent the boundary conditions at $x = 0$ and $x = L$, respectively, and the middle part of matrix demonstrates the continuity conditions at the singularity points. Matrix **J** can be divided into three parts as:

$$\mathbf{J} = \begin{bmatrix} [\mathbf{J_1}]_{2\times 4N} \\ [\mathbf{J_2}]_{4(N-1)\times 4N} \\ [\mathbf{J_3}]_{2\times 4N} \end{bmatrix}_{4N\times 4N} \tag{3.27}$$

where

$$\mathbf{J}_1 = \begin{bmatrix} 0 & 1 & 0 & 1 & 0 & \cdots & 0 \\ 1 & 0 & 1 & 0 & 0 & \cdots & 0 \end{bmatrix}_{2\times 4N} \tag{3.28}$$

represents the clamed boundary condition at $x = 0$ given by Eq. (3.11),

$$\mathbf{J_2} = \begin{bmatrix} \overset{1}{[} & J_2^{(1)} & \overset{8}{]}_{4\times 8} & & & \\ & \overset{5}{[} & J_2^{(2)} & \overset{12}{]}_{4\times 8} & \mathbf{0} & \\ & & & \ddots & & \\ & \mathbf{0} & & & \overset{4(N-2)}{[} \; J_2^{(N-1)} \; \overset{4N}{]}_{4\times 8} & \end{bmatrix}_{4(N-1)\times 4N} \tag{3.29}$$

includes the continuity conditions given by Eqs. (3.16)-(3.19) at (N-1) points of discontinuity with

$$J_2^{(n)} = \begin{bmatrix} \sin\alpha_n\beta l_n & \cos\alpha_n\beta l_n & \sinh\alpha_n\beta l_n & \cosh\alpha_n\beta l_n \\ \alpha_n\beta\cos\alpha_n\beta l_n & -\alpha_n\beta\sin\alpha_n\beta l_n & \alpha_n\beta\cosh\alpha_n\beta l_n & \alpha_n\beta\sinh\alpha_n\beta l_n \\ -\gamma_n\alpha_n^2\beta^2\sin\alpha_n\beta l_n & -\gamma_n\alpha_n^2\beta^2\cos\alpha_n\beta l_n & \gamma_n\alpha_n^2\beta^2\sinh\alpha_n\beta l_n & \gamma_n\alpha_n^2\beta^2\cosh\alpha_n\beta l_n \\ -\gamma_n\alpha_n^3\beta^3\cos\alpha_n\beta l_n & \gamma_n\alpha_n^3\beta^3\sin\alpha_n\beta l_n & \gamma_n\alpha_n^3\beta^3\cosh\alpha_n\beta l_n & \gamma_n\alpha_n^3\beta^3\sinh\alpha_n\beta l_n \end{bmatrix}$$

$$\begin{bmatrix} -\sin\alpha_{n+1}\beta l_n & -\cos\alpha_{n+1}\beta l_n & -\sinh\alpha_{n+1}\beta l_n & -\cosh\alpha_{n+1}\beta l_n \\ -\alpha_{n+1}\beta\ \cos\alpha_{n+1}\beta l_n & \alpha_{n+1}\beta\ \sin\alpha_{n+1}\beta l_n & -\alpha_{n+1}\beta\ \cosh\alpha_{n+1}\beta l_n & -\alpha_{n+1}\beta\ \sinh\alpha_{n+1}\beta l_n \\ \alpha_{n+1}^2\beta^2 \sin\alpha_{n+1}\beta l_n & \alpha_{n+1}^2\beta^2 \cos\alpha_{n+1}\beta l_n & -\alpha_{n+1}^2\beta^2 \sinh\alpha_{n+1}\beta l_n & -\alpha_{n+1}^2\beta^2 \cosh\alpha_{n+1}\beta l_n \\ \alpha_{n+1}^3\beta^3 \cos\alpha_{n+1}\beta l_n & -\alpha_{n+1}^3\beta^3 \sin\alpha_{n+1}\beta l_n & -\alpha_{n+1}^3\beta^3 \cosh\alpha_{n+1}\beta l_n & -\alpha_{n+1}^3\beta^3 \sinh\alpha_{n+1}\beta l_n \end{bmatrix}_{4\times 8}$$

(3.30)

and

$$\mathbf{J}_3 = \begin{bmatrix} 0 & \cdots & 0 & -\alpha_N^2\beta^2 \sin\alpha_N\beta l_N & -\alpha_N^2\beta^2 \cos\alpha_N\beta l_N & \alpha_N^2\beta^2 \sinh\alpha_N\beta l_N & \alpha_N^2\beta^2 \cosh\alpha_N\beta l_N \\ 0 & \cdots & 0 & -\alpha_N^3\beta^3 \cos\alpha_N\beta l_N & \alpha_N^3\beta^3 \sin\alpha_N\beta l_N & \alpha_N^3\beta^3 \cosh\alpha_N\beta l_N & \alpha_N^3\beta^3 \sinh\alpha_N\beta l_N \end{bmatrix}_{2\times 4N}$$

(3.31)

represents the free boundary condition at $x = L$ given by Eqs. (3.21) and (3.22).

In order to obtain a non-trivial solution for Eq. (3.25) and find the natural frequencies and mode shapes, the determinant of matrix **J** must be set to zero

$$\det\left[\mathbf{J}(\beta)\right] = 0 \tag{3.32}$$

Since this matrix is a function of only parameter $\beta \in (0, \infty)$, its determinant can be numerically evaluated for its zero values by continuously varying parameter β with a reasonably small step size within a range of interest starting from, but excluding zero. The values of β which satisfy Eq. (3.32) lead to calculation of natural frequencies using a modified version of Eq. (3.7) as follows:

$$\omega_r^2 = \left(\beta^{(r)}\right)^4 \frac{(EI)_1}{m_1} = \left(\beta_n^{(r)}\right)^4 \frac{(EI)_n}{m_n} \tag{3.33}$$

where $\beta^{(r)}$s are solutions for Eq. (3.32) and ω_r is the corresponding r^{th} natural frequency. Since the determinant of matrix **J** has been set to zero for the selected values of β, the mode shape coefficients A_1 to D_N are linearly dependent. In order to obtain unique solution for these coefficients, orthonormality between mode shapes can be utilized. For the conventional boundary conditions considered here, this condition is stated as:

$$\int_{l_0}^{l_N} m(x)\phi^{(r)}(x)\phi^{(s)}(x)dx = \delta_{rs} \text{ or } \int_{l_0}^{l_N} m(x)\left(\phi^{(r)}(x)\right)^2 dx = 1 \tag{3.34}$$

where δ_{rs} is the Kronecker delta function, and $\phi^{(r)}(x)$ is the r^{th} mode shape of beam expressed as:

$$\phi^{(r)}(x) = \begin{cases} \phi_1^{(r)}(x) = A_1^{(r)} \sin\beta_1^{(r)}x + B_1^{(r)} \cos\beta_1^{(r)}x + C_1^{(r)} \sinh\beta_1^{(r)}x + D_1^{(r)} \cosh\beta_1^{(r)}, & l_0 \le x \le l_1 \\ \phi_2^{(r)}(x) = A_2^{(r)} \sin\beta_2^{(r)}x + B_2^{(r)} \cos\beta_2^{(r)}x + C_2^{(r)} \sinh\beta_2^{(r)}x + D_2^{(r)} \cosh\beta_2^{(r)}x, & l_1 < x \le l_2 \\ \vdots & \\ \phi_N^{(r)}(x) = A_N^{(r)} \sin\beta_N^{(r)}x + B_N^{(r)} \cos\beta_N^{(r)}x + C_N^{(r)} \sinh\beta_N^{(r)}x + D_N^{(r)} \cosh\beta_N^{(r)}x, & l_{N-1} < x \le l_N \end{cases} \tag{3.35}$$

The obtained mode shapes and natural frequencies are used to derive the ODE of motion for a beam under distributed dynamic excitation as will be discussed next.

3.2.2. Forced Motion Analysis of Stepped EB Beam

Using expansion theorem for the beam vibration analysis, the expression for the transverse displacement becomes:

$$w(x,t) = \sum_{r=1}^{\infty} \phi^{(r)}(x)q^{(r)}(t) \tag{3.36}$$

where $q^{(r)}(t)$ is the generalized time-dependent coordinate for the r^{th} mode. Substituting Eq. (3.36) into PDE of motion Eq. (3.1) yields:

$$\sum_{r=1}^{\infty}\left\{\frac{d^2}{dx^2}\left[E(x)I(x)\frac{d^2\phi^{(r)}(x)}{dx^2}\right]q^{(r)}(t)+c(x)\phi^{(r)}(x)\dot{q}^{(r)}(t)+m(x)\phi^{(r)}(x)\ddot{q}^{(r)}(t)\right\}=P(x,t) \tag{3.37}$$

To safely take the term $E(x)I(x)$ out of the bracket for the beam with multiple discontinuities, Eq. (3.37) is multiplied by s^{th} mode shape, $\phi^{(s)}(x)$, and is integrated over the beam length:

$$\int_{l_0}^{l_N}\left\{\sum_{r=1}^{\infty}\left(\frac{d^2}{dx^2}\left[E(x)I(x)\frac{d^2\phi^{(r)}(x)}{dx^2}\right]\phi^{(s)}(x)q^{(r)}(t)+c(x)\phi^{(r)}(x)\phi^{(s)}(x)\dot{q}^{(r)}(t)\right.\right.$$
$$\left.\left.+m(x)\phi^{(r)}(x)\phi^{(s)}(x)\ddot{q}^{(r)}(t)\right)\right\}dx=\int_{l_0}^{l_N}P(x,t)\phi^{(s)}(x)dx=0 \tag{3.38}$$

Recall Eq. (3.6) which can be modified to

$$(EI)_n\frac{d^4\phi_n^{(r)}(x)}{dx^4}=\omega_r^2 m_n\phi_n^{(r)}(x) \tag{3.39}$$

Using Eq. (3.39) and dividing the spatial integral into N uniform segments, one can write:

$$\int_{l_0}^{l_N}\left(\frac{d^2}{dx^2}\left[E(x)I(x)\frac{d^2\phi^{(r)}(x)}{dx^2}\right]\phi^{(s)}(x)q^{(r)}(t)\right)dx=\sum_{n=1}^{N}\left[\int_{l_{n-1}}^{l_n}(EI)_n\frac{d^4\phi_n^{(r)}(x)}{dx^4}\phi_n^{(s)}(x)q^{(r)}(t)dx\right]=$$
$$\sum_{n=1}^{N}\left[\int_{l_{n-1}}^{l_n}\omega_r^2 m_n\phi_n^{(r)}(x)\phi_n^{(s)}(x)q^{(r)}(t)dx\right]=\omega_r^2 q^{(r)}(t)\int_{l_0}^{l_N}m(x)\phi^{(r)}(x)\phi^{(s)}(x)dx \tag{3.40}$$

Applying beam orthogonality conditions given by:

$$\int_{l_0}^{l_N} m(x)\phi^{(r)}(x)\phi^{(s)}(x)dx = \int_{l_0}^{l_N} E(x)I(x)\phi^{(r)}(x)\phi^{(s)}(x)dx = \delta_{rs} \tag{3.41}$$

and using Eq. (3.40), Eq. (3.38) can be recast as:

$$\ddot{q}^{(r)}(t) + \sum_{s=1}^{\infty}\left\{\dot{q}^{(s)}(t)\int_{l_0}^{l_N} c(x)\phi^{(r)}(x)\phi^{(s)}(x)dx\right\} + \omega_r^2 q^{(r)}(t) = \int_{l_0}^{l_N} P(x,t)\phi^{(r)}(x)dx \ , \ r = 1,2,...,\infty \tag{3.42}$$

which can be simplified to

$$\ddot{q}^{(r)}(t) + \sum_{s=1}^{\infty}\left\{c_{rs}\dot{q}^{(s)}(t)\right\} + \omega_r^2 q^{(r)}(t) = f^{(r)}(t) \tag{3.43}$$

where

$$c_{rs} = \int_{l_0}^{l_N} c(x)\phi^{(r)}(x)\phi^{(s)}(x)dx, \quad f^{(r)}(t) = \int_{l_0}^{l_N} P(x,t)\phi^{(r)}(x)dx \tag{3.44}$$

The truncated *k*-mode description of the beam Eq. (3.43) can now be presented in the following matrix form:

$$\mathbf{M}\ddot{\mathbf{q}} + \mathbf{C}\dot{\mathbf{q}} + \mathbf{K}\mathbf{q} = \mathbf{F} \tag{3.45}$$

where

$$\begin{aligned}&\mathbf{M} = I_{k\times k}, \mathbf{C} = [c_{rs}]_{k\times k}, \mathbf{K} = [\omega_r^2\delta_{rs}]_{k\times k}, \mathbf{q} = [q^{(1)}(t), q^{(2)}(t), \ldots, q^{(k)}(t)]_{k\times 1}^T, \\ &\mathbf{F} = [f^{(1)}(t), f^{(2)}(t), \ldots, f^{(k)}(t)]_{k\times 1}^T\end{aligned} \tag{3.46}$$

The state-space representation of Eq. (3.45) is given by:

$$\dot{\mathbf{X}} = \mathbf{AX} + \mathbf{Bu} \tag{3.47}$$

where

$$\mathbf{A} = \begin{bmatrix} \mathbf{0} & \mathbf{I} \\ -\mathbf{M}^{-1}\mathbf{K} & -\mathbf{M}^{-1}\mathbf{C} \end{bmatrix}_{2k\times 2k},\ \mathbf{B} = \begin{bmatrix} \mathbf{0} \\ \mathbf{M}^{-1} \end{bmatrix}_{2k\times k},\ \mathbf{X} = \begin{Bmatrix} \mathbf{q} \\ \dot{\mathbf{q}} \end{Bmatrix}_{2k\times 1},\ \mathbf{u} = \mathbf{F}_{k\times 1} \tag{3.48}$$

The implementation of the proposed framework will be studied in the next section for a particular case of interest, where the EB beam has two stepped points in cross section and is subjected to a distributed dynamic excitation.

3.3. An Example Case Study: EB beam with two jumped discontinuity in cross-section

An example case of study is considered in this section to demonstrate the implementation of the proposed method for forced vibration analysis of a flexible beam with jump discontinuities. Figure 3.3 depicts a cantilever beam with two jump discontinuities in the cross-section subjected to a vertical load uniformly applied at the middle section. This may resemble a cantilever beam with an actuator/sensor pair attached to its middle part. The objective is to derive the equations of motion and depict the mode shapes and frequency response of the beam for a finite number of modes.

To observe the effects of the jump on the beam's mode shapes and system's frequency response, several length and thickness values are considered for the middle cross section as listed in Tables 3.1 and 3.2. It is assumed that Sections 1 and 3 have the same dimensions and properties, and only the thickness of the beam jumps in Section 2.

We first formulate the problem based on the proposed approach detailed in the preceding section.

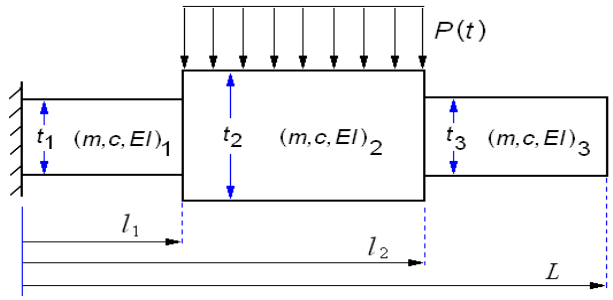

Figure 3.3. EB beam with two stepped discontinuities in cross section under distributed dynamic load.

Matrix **J** for the depicted beam configuration can be formed using Eqs. (3.27)-(3.31) as follows:

$$\mathbf{J}_{12\times12}=\begin{bmatrix}
0 & 1 & 0 & 1 & 0 & 0\\
1 & 0 & 1 & 0 & 0 & 0\\
\sin\beta l_1 & \cos\beta l_1 & \sinh\beta l_1 & \cosh\beta l_1 & -\sin\alpha_2\beta l_1 & -\cos\alpha_2\beta l_1\\
\beta\cos\beta l_1 & -\beta\sin\beta l_1 & \beta\cosh\beta l_1 & \beta\sinh\beta l_1 & -\alpha_2\beta\cos\alpha_2\beta l_1 & \alpha_2\beta\sin\alpha_2\beta l_1\\
-\gamma_1\beta^2\sin\beta l_1 & -\gamma_1\beta^2\cos\beta l_1 & \gamma_1\beta^2\sinh\beta l_1 & \gamma_1\beta^2\cosh\beta l_1 & \alpha_2^2\beta^2\sin\alpha_2\beta l_1 & \alpha_2^2\beta^2\cos\alpha_2\beta l_1\\
-\gamma_1\beta^3\cos\beta l_1 & \gamma_1\beta^3\sin\beta l_1 & \gamma_1\beta^3\cosh\beta l_1 & \gamma_1\beta^3\sinh\beta l_1 & \alpha_2^3\beta^3\cos\alpha_2\beta l_1 & -\alpha_2^3\beta^3\sin\alpha_2\beta l_1\\
0 & 0 & 0 & 0 & \sin\alpha_2\beta l_2 & \cos\alpha_2\beta l_2\\
0 & 0 & 0 & 0 & \alpha_2\beta\cos\alpha_2\beta l_2 & -\alpha_2\beta\sin\alpha_2\beta l_2\\
0 & 0 & 0 & 0 & -\gamma_2\alpha_2^2\beta^2\sin\alpha_2\beta l_2 & -\gamma_2\alpha_2^2\beta^2\cos\alpha_2\beta l_2\\
0 & 0 & 0 & 0 & -\gamma_2\alpha_2^3\beta^3\cos\alpha_2\beta l_2 & \gamma_2\alpha_2^3\beta^3\sin\alpha_2\beta l_2\\
0 & 0 & 0 & 0 & 0 & 0\\
0 & 0 & 0 & 0 & 0 & 0
\end{bmatrix}$$

$$
\begin{bmatrix}
0 & 0 & 0 & 0 & 0 & 0 \\
0 & 0 & 0 & 0 & 0 & 0 \\
-\sinh\alpha_2\beta l_1 & -\cosh\alpha_2\beta l_1 & 0 & 0 & 0 & 0 \\
-\alpha_2\beta\cosh\alpha_2\beta l_1 & -\alpha_2\beta\sinh\alpha_2\beta l_1 & 0 & 0 & 0 & 0 \\
-\alpha_2^2\beta^2\sinh\alpha_2\beta l_1 & -\alpha_2^2\beta^2\cosh\alpha_2\beta l_1 & 0 & 0 & 0 & 0 \\
-\alpha_2^3\beta^3\cosh\alpha_2\beta l_1 & -\alpha_2^3\beta^3\sinh\alpha_2\beta l_1 & 0 & 0 & 0 & 0 \\
\sinh\alpha_2\beta l_2 & \cosh\alpha_2\beta l_2 & -\sin\alpha_3\beta l_2 & -\cos\alpha_3\beta l_2 & -\sinh\alpha_3\beta l_2 & -\cosh\alpha_3\beta l_2 \\
\alpha_2\beta\cosh\alpha_2\beta l_2 & \alpha_2\beta\sinh\alpha_2\beta l_2 & -\alpha_3\beta\cos\alpha_3\beta l_2 & \alpha_3\beta\sin\alpha_3\beta l_2 & -\alpha_3\beta\cosh\alpha_3\beta l_2 & -\alpha_3\beta\sinh\alpha_3\beta l_2 \\
\gamma_2\alpha_2^2\beta^2\sinh\alpha_2\beta l_2 & \gamma_2\alpha_2^2\beta^2\cosh\alpha_2\beta l_2 & \alpha_3^2\beta^2\sin\alpha_3\beta l_2 & \alpha_3^2\beta^2\cos\alpha_3\beta l_2 & -\alpha_3^2\beta^2\sinh\alpha_2\beta l_2 & -\alpha_3^2\beta^2\cosh\alpha_3\beta l_2 \\
\gamma_2\alpha_2^3\beta^3\cosh\alpha_2\beta l_2 & \gamma_2\alpha_2^3\beta^3\sinh\alpha_2\beta l_2 & \alpha_3^3\beta^3\cos\alpha_3\beta l_2 & -\alpha_3^3\beta^3\sin\alpha_3\beta l_2 & -\alpha_3^3\beta^3\cosh\alpha_3\beta l_2 & -\alpha_3^3\beta^3\sinh\alpha_3\beta l_2 \\
0 & 0 & -\alpha_3^2\beta^2\sin\alpha_3\beta L & -\alpha_3^2\beta^2\cos\alpha_3\beta L & \alpha_3^2\beta^2\sinh\alpha_3\beta L & \alpha_3^2\beta^2\cosh\alpha_3\beta L \\
0 & 0 & -\alpha_3^3\beta^3\cos\alpha_3\beta L & \alpha_3^3\beta^3\sin\alpha_3\beta L & \alpha_3^3\beta^3\cosh\alpha_3\beta L & \alpha_3^3\beta^3\sinh\alpha_3\beta L
\end{bmatrix}
\tag{2.49}
$$

Varying parameter β with small steps over a desired range, and finding for the zeros of determinant of **J**, leads to determination of the natural frequencies of the beam using Eq. (3.33). The coefficients of the mode shapes can be obtained through Eqs. (3.32) and (3.34). The $(r)^{\text{th}}$ mode shape of the beam can be written as:

$$
\phi^{(r)}(x) = \begin{cases}
\phi_1^{(r)}(x) = A_1^{(r)}\sin\beta_1^{(r)}x + B_1^{(r)}\cos\beta_1^{(r)}x + C_1^{(r)}\sinh\beta_1^{(r)}x + D_1^{(r)}\cosh\beta_1^{(r)}x, & 0 \le x \le l_1 \\
\phi_2^{(r)}(x) = A_2^{(r)}\sin\beta_2^{(r)}x + B_2^{(r)}\cos\beta_2^{(r)}x + C_2^{(r)}\sinh\beta_2^{(r)}x + D_2^{(r)}\cosh\beta_2^{(r)}x, & l_1 \le x \le l_2 \\
\phi_3^{(r)}(x) = A_3^{(r)}\sin\beta_3^{(r)}x + B_3^{(r)}\cos\beta_3^{(r)}x + C_3^{(r)}\sinh\beta_3^{(r)}x + D_3^{(r)}\cosh\beta_3^{(r)}x, & l_2 \le x \le L
\end{cases}
\tag{3.50}
$$

To derive the equations of motion, the elements of Eq. (3.46) must be calculated first. Let's assume that the damping coefficient of the beam remains constant for the entire length of beam (i.e. $c(x) = c$), and the time-varying vertical load is uniformly distributed in the middle segment ($P(x, t) = P(t)$ for $l_1 < x < l_2$, and $P(x, t) = 0$ for $x < l_1$ or $x > l_2$). Consequently, this yields:

$$c_{rs} = \int_{l_0}^{l_N} c(x)\phi^{(r)}(x)\phi^{(s)}(x)dx = c\left\{\int_{0}^{l_1} \phi_1^{(r)}(x)\phi_1^{(s)}(x)dx + \int_{l_1}^{l_2} \phi_2^{(r)}(x)\phi_2^{(s)}(x)dx + \int_{l_2}^{L} \phi_3^{(r)}(x)\phi_3^{(s)}(x)dx\right\}$$

$$f^{(r)}(t) = \int_{l_0}^{l_N} P(x,t)\phi^{(r)}(x)dx = P(t)\int_{l_1}^{l_2} \phi_2^{(r)}(x)dx \tag{3.51}$$

Thus, the equation of motion and its state-space representation can be formed based on Eqs. (3.43)-(3.48).

Once the system is derived in state-space, frequency response of system can be plotted to demonstrate the behavior of system within a desired frequency range. Without loss of generality, the displacement of an arbitrary point ($x = L_0$) is taken as the system output:

$$\mathbf{Y}(t) = \omega(L_0,t) = \sum_{r=1}^{k} \phi^{(r)}(L_0)q^{(r)}(t) = [\phi^{(1)}(L_0), \phi^{(2)}(L_0), ..., \phi^{(k)}(L_0), 0, ..., 0]_{1\times 2k}\,\mathbf{X}(t) \tag{3.52}$$

The standard form of state-space representation of the system can then be written as:

$$\begin{aligned} \dot{\mathbf{X}} &= \mathbf{AX} + \mathbf{Bu} \\ \mathbf{Y} &= \mathbf{CX} \end{aligned} \tag{3.53}$$

where

$$\mathbf{C} = [\phi^{(1)}(L_0), \phi^{(2)}(L_0), ..., \phi^{(k)}(L_0), 0, ..., 0]_{1\times 2k} \tag{3.54}$$

The frequency response of the system can now be plotted using beam's transfer function obtained through the Laplace transformation of its state-space model as follows:

$$G(s) = \frac{Y(s)}{U(s)} = \mathbf{C}(sI - \mathbf{A})^{-1}\mathbf{B} \tag{3.55}$$

Numerical simulations have been performed in the next subsection to demonstrate the mode shapes and frequency response plot of beam configuration discussed in this section.

3.3.1. Numerical Simulations and Discussions

Two sets of numerical simulations are presented in this section; the first case is designated to study the effects of thickness variation of beam's middle cross section, while in the second case, the effects of length variation of the beam's middle cross section is investigated. The objective of the simulations is to demonstrate how different jump configurations may affect the beam's mode shapes and natural frequencies.

Table 3.1 indicates the parameter values used for the simulation of the first scenario, where beam's thickness in the middle section varies. Beam's equation of motion has been truncated into only four modes, and five different thickness values have been considered for the middle section, one of which being a uniform beam without any jump in cross-section. Figure 3.4 depicts the mode shapes of beam for different configurations. As seen from the results, mode shapes of the beam significantly change as the thickness of the jump increases. Particularly, it is observed that such a change has more effect on even modes (2 and 4) compared to odd modes (1 and 3). This reason perhaps is due to the fact that the middle section resists against bending in modes 2 and 4, while it is located on a fairly straight curvature in modes 1 and 3. This not only affects beam's modes shapes, but also its natural frequencies; the frequency response plot given in Figure 3.5 depicts that the first and third natural frequencies of beam for different jump configurations are localized, in contrast to the frequencies of second and fourth modes, where the frequency

peaks are more scattered. The continuity of the mode shapes at jump points can be clearly seen from the figures, as expected from the analysis.

The parameter values used for the simulation of second scenario, where the effect of length variation is considered, are given in Table 3.1. This table also includes first four natural frequencies. The obtained modes shapes of beam's tip displacement and the frequency response plots are depicted in Figures 3.6 and 3.7, respectively. Similar to the first scenario, the length variation of the middle section significantly affects the mode shapes; particularly, second and fourth modes demonstrate larger changes in their shapes and natural frequencies compared to first and third modes, due to their larger curvature within the location of middle section.

Table 3.1. Beam parameters for numerical simulation of different *thickness* values in the middle section.

Config.	l_1(m)	l_2(m)	L(m)	t_1(m)	t_2(m)	t_3(m)	ω_1(rad/sec)	ω_2(rad/sec)	ω_3(rad/sec)	ω_4(rad/sec)
T1	0.1	0.2	0.3	0.001	0.001	0.001	57.1	357.9	1002.1	1963.7
T2	0.1	0.2	0.3	0.001	0.0015	0.001	58.1	431.9	1059.2	2293.9
T3	0.1	0.2	0.3	0.001	0.002	0.001	56.4	459.5	1052.1	2642.6
T4	0.1	0.2	0.3	0.001	0.0025	0.001	54.4	463.8	1030.3	2906.1
T5	0.1	0.2	0.3	0.001	0.003	0.001	52.5	459.3	1005.5	3070.2

Beam's other parameters:
Density: ρ = 7800(kg/m^3), Width: b = 0.01(m), Damping coefficient: c = 0.001(N.sec/m), Young's modulus of elasticity: E = 200(Gpa)

Table 3.2. Beam parameters for numerical simulation of different *length* values in the middle section.

Config.	l_1(m)	l_2(m)	L(m)	t_1(m)	t_2(m)	t_3(m)	ω_1(rad/sec)	ω_2(rad/sec)	ω_3(rad/sec)	ω_4(rad/sec)
L1	0.15	0.15	0.3	0.001	0.003	0.001	57.1	357.9	1002.1	1963.7
L2	0.125	0.175	0.3	0.001	0.003	0.001	54.7	365.5	988.5	2253.8
L3	0.1	0.2	0.3	0.001	0.003	0.001	52.5	459.3	1005.5	3070.2
L4	0.075	2.25	0.3	0.001	0.003	0.001	51.5	627.4	1232.2	3403.0

Other beam parameters are the same as those specified in Table 1.

Table 3.3. Normalized slope difference of the mode shapes between the starting and the ending step points.

	Config. T1	Config. T2	Config. T3	Config. T4	Config. T5
Mode 1	1	0.30	0.12	0.06	0.03
Mode 2	1	0.55	0.29	0.16	0.10
Mode 3	1	0.75	0.46	0.29	0.18
Mode 4	1	0.87	0.66	0.46	0.31

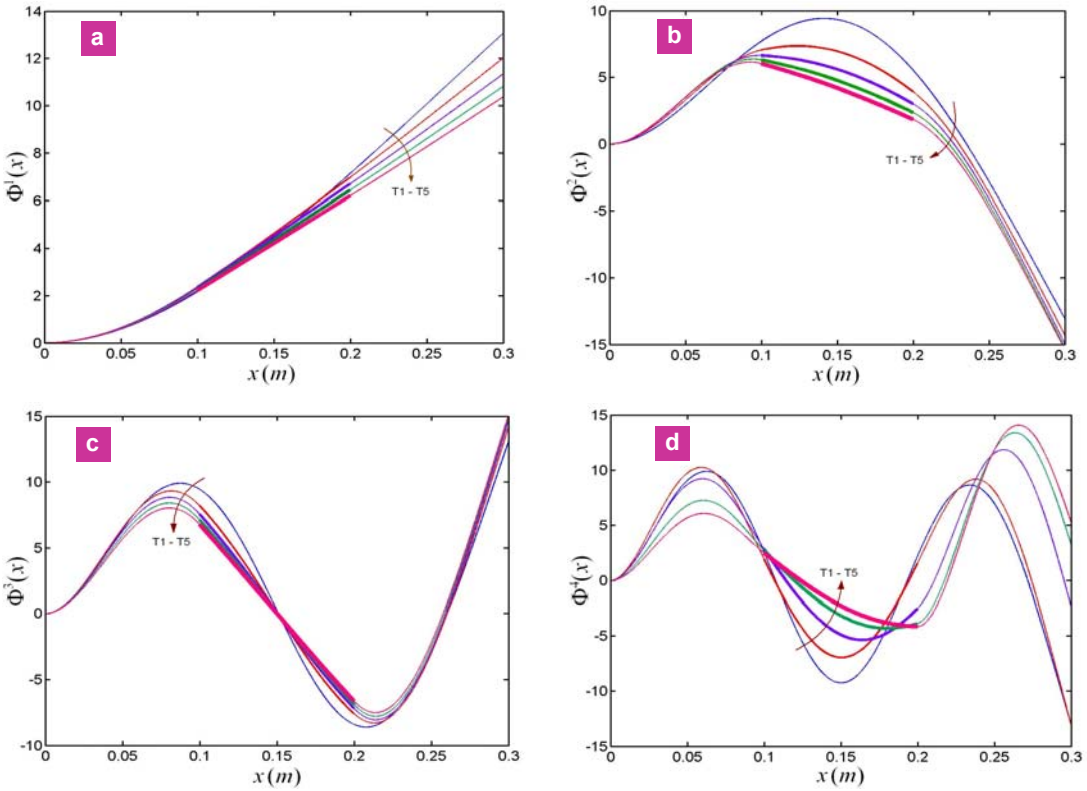

Figure 3.4. (a) First, (b) second, (c) third, and (d) fourth mode shapes of beams with five different middle section *thicknesses*.

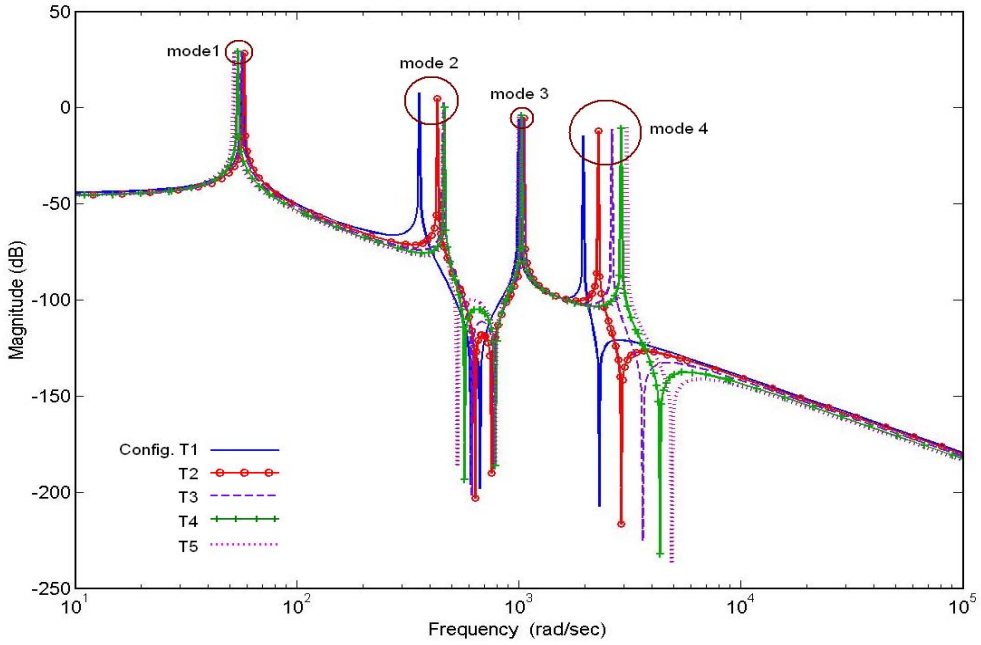

Figure 3.5. Modal frequency response plot of beams tip displacements for five different middle section *thicknesses*.

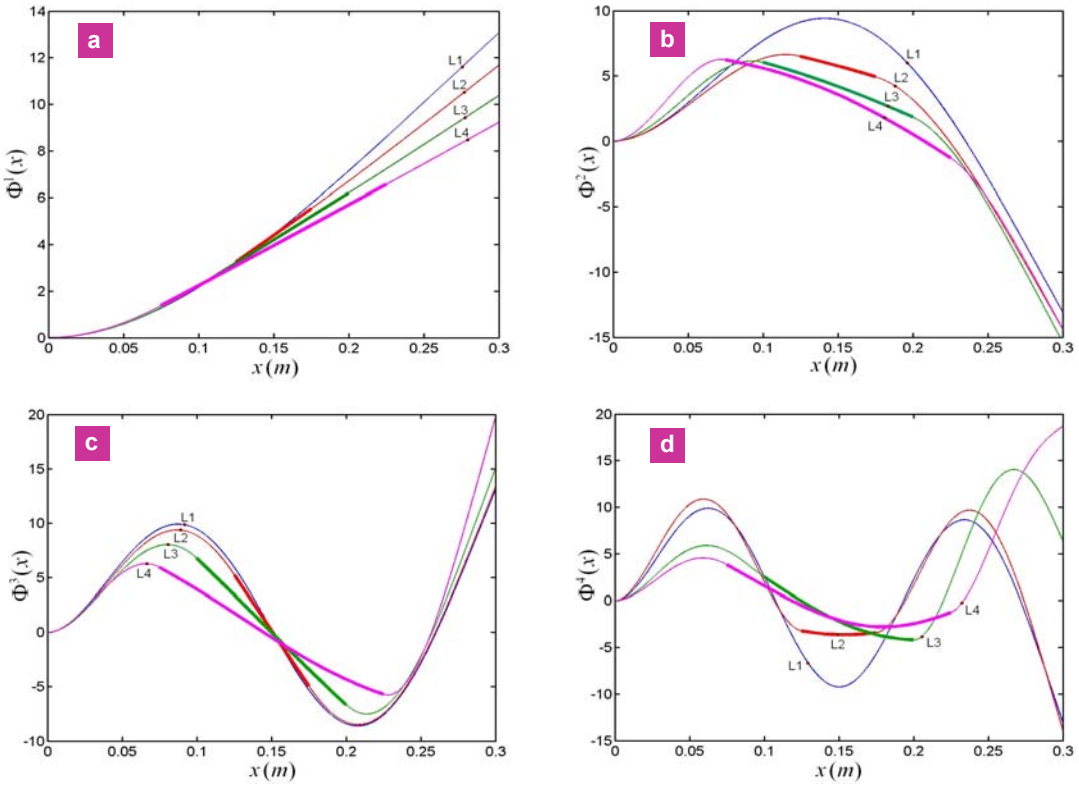

Figure 3.6. (a) First, (b) second, (c) third, and (d) fourth mode shapes of beams with four different middle section *lengths*.

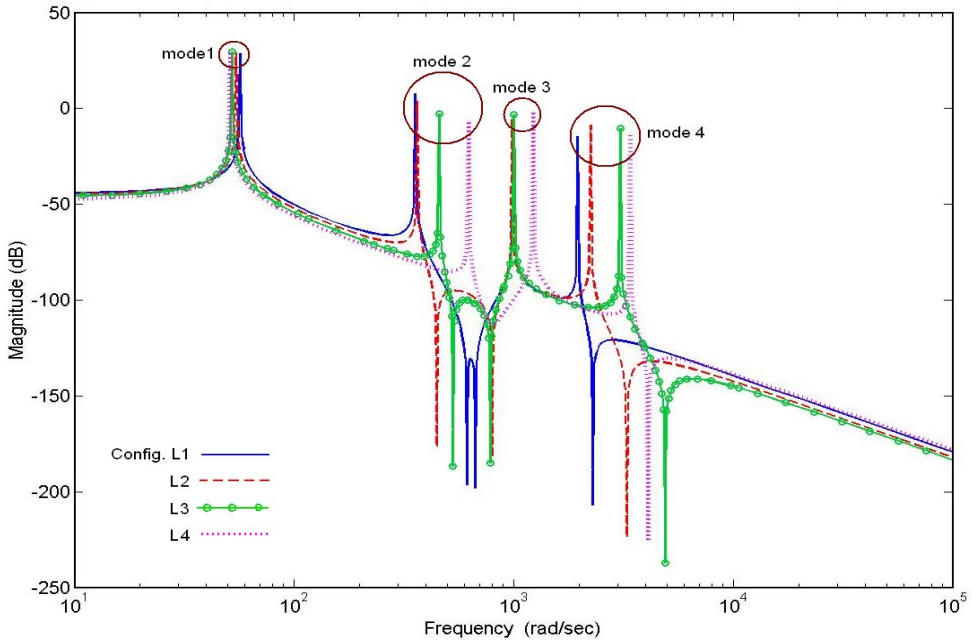

Figure 3.7. Modal frequency response plot of beams tip displacements for four different middle section *lengths*.

If the presence of the added mass in the middle section is due to the attachment of patch sensors (e.g. piezoelectric or piezoresistive sensors), the slope difference of the mode shapes between the starting and ending points of attachment is proportional to the sensor output voltage [75]:

$$v_{sens}^{(r)}(t) = \frac{E_p h_p d_{31} b}{C_f}\left[\frac{d\phi^{(r)}(l_2)}{dx} - \frac{d\phi^{(r)}(l_1)}{dx}\right]\cdot q^{(r)}(t) \tag{3.56}$$

where $v_{sens}^{(r)}$ is the output voltage of the sensor associated with the r^{th} mode. It would be interesting to observe how the presence of sensor and its added mass and stiffness would affect the output voltage estimation (the expression inside bracket in Eq. (3.56)). For this, the slope difference of the beam with different thickness values of the middle section (beam specified in Table 3.1) at the points of discontinuities are calculated and

normalized to the beam with the uniform cross-section (configuration T1). The reason for this normalization is to compare the stepped beams with the uniform beam to determine the percentage of error induced by the assumption of uniform cross-section for beams with patch sensors in different thicknesses.

Table 3.3 reveals the normalized slope difference of the mode shapes between the starting and the ending step points. It is seen from the table that as the thickness of the cross-section increases, the slope difference drastically drops. According to the table, if the real configuration of a beam/sensor pair corresponds to the thinnest jump, that is, Configuration T2, the assumption of a uniform beam (Configuration T1) for the system leads to 230% estimation error for mode 1, 80% for mode 2, 30% for mode 3, and 15% for mode 4. As the thickness of the jump increases, the error percentages further increase. The results shall prove the high degree of need to the modeling of cross-sectional discontinuities in flexible beams, and may indicate the impact of the proposed framework to the area of vibrations and vibration control systems.

3.4. Conclusions

This section presented a comperhensive framework for derivation of mode shapes and state-space representation of motion of flexible EB beams with multiple jump discontinuities in their cross section. To solve the governing equations of motion, the beam was divided into uniform segments of constant parameters, and the continuity conditions were applied at the partitioned points. The characteristics matrix was then formulated using the beam boundary and continuity conditions. Natural frequencies of beam were obtained by setting the determinant of characteristics matrix to zero. The

governing equations were discretized and its state-space representation was then derived for the beam under a distributed dynamic loading condition. To demonstrate the proposed method, the formulations and numerical simulations have been presented for a beam with two stepped discontinuities in the cross-section. Results indicate that the effects of added mass and stiffness at the middle section on the beam mode shapes and natural frequencies are significant. Hence, exact solutions are required for practical implementation of such discontinuous structures.

CHAPTER FOUR

MODELING AND EXPERIMENTAL VIBRATION ANALYSIS OF MICROCANTILEVER ACTIVE PROBES®

4.1. Introduction

Microcantilever beams with their structural flexibility, sensitivity to atomic and molecular forces, and ultra-fast responsiveness have recently attracted widespread attention in variety of applications including atomic force and friction microscopy [92-95], biomass sensing [96-101], thermal scanning microscopy [102-107], and MEMS switches [108-109]. In all above applications, the shift in the natural frequency of microcantilever in sensing condition away from that of original microcantilever is used as a sensing element [110-114].

In recent years, a new generation of piezoelectric microcantilever beams so-called "Active Probes®" has been introduced and received great attention due to its unique configuration (see Figure 4.1). The probe is covered by a piezoelectric layer on the top surface. This layer is utilized as a potential source of actuation, or as an alternative transduction for the laser interferometer in the next-generation laserless AFMs. In typical configuration of Active Probe®, body of the microcantilever is designed wider due to the presence of piezoelectric layer, while the tip zone is made narrower in order to improve tip deflection measurement. Hence, the Active Probes® has two steps in the cross-section:

one small step where the piezoelectric layer ends and one larger step where the microcantilever cross-sectional area decreases suddenly.

These discontinuities can significantly affect the modal characteristics of the system, and consequently the level of measurement precision in different scenarios. For example, when piezoelectric layer is used as a sensor, the generated voltage can be utilized to detect the vertical deflection of Active Probes®. In this case, the magnitude of output voltage is proportional to the slope difference of the deflection at two ends of the attached piezoelectric layer as explained in the pervious chapter [115]. Along this line of reasoning, developing an accurate dynamic model for microcantilever with jump discontinuities in cross-section is important and can have significant impact on sensing and imaging enhancement of Active Probes®.

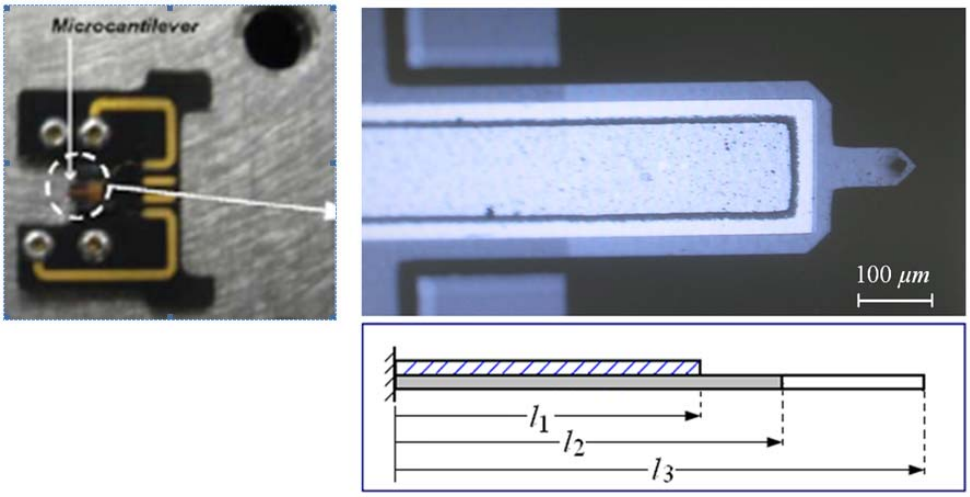

Figure 4.1. piezoelectrically-driven microcantilever beam with cross-sectional discontinuity.

As reported here, a general and practical framework was developed in preceding chapter for flexible beams with multiple jumped discontinuities in the cross-section

[116]. It was shown that the effects of added mass and stiffness on the beam mode shapes and natural frequencies are significant. Also, results from forced vibration analysis indicate that the system frequency response is affected by geometrical discontinuities of the structure. In this regard, this chapter is aimed at acquiring a precise model for modal characterization and dynamic analysis of the aforementioned Active Probes® with geometrical discontinuities. To this end, the entire length of Active Probes® is divided into three uniform segments consisting of a composite beam with the piezoelectric layer and two segments of simple beams with different cross-sectional areas.

The governing equation of motion is consequently divided into three partial differential equations with two sets of continuity conditions applied to the points of discontinuity. The eigenvalue problem associated with the cantilever configuration is then solved to obtain microcantilever mode shapes and natural frequencies. Using the well-known pin-force model, the induced electromechanical stress in the piezoelectric layer is replaced with a pair of concentrated moments at both ends of attachment. Moreover, applying the method of assumed modes, the governing equations reduce to ordinary differential equations to arrive at the state-space representation of the system. Results from the proposed model are compared with those obtained from experiment and commonly used theory for the uniform beams. It is clearly demonstrated that the proposed model provides good agreement with the experimental results. Furthermore, it is shown that assuming uniform geometry and configuration for the dynamic analysis of the current Active Probe is not a valid strategy and creates significant error in measurements.

4.2. Experimental Setup and Procedure

In this section, an Active Probe®, the DMASP manufactured by Veeco Instruments Inc. [www.veeco.com], is used to study the dynamic response of the probe. For this purpose, an experimental set-up is built using a state-of-the-art microsystem analyzer, the MSA-400 manufactured by Polytec Inc. [www.polytec.com]. MSA-400 employs the laser Doppler vibrometry and stroboscopic video microscopy to measure the 3D dynamic response of MEMS and NEMS (see Figure 4.2). It features picometer displacement resolution for out-of-plane measurement, as well as measures frequencies as high as 20 MHz.

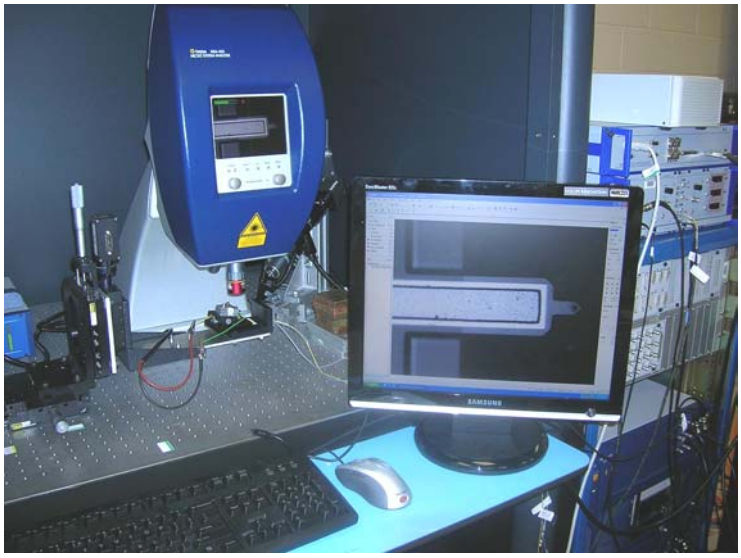

Figure 4.2. Experimental setup for microcantilever under Micro System Analyzer (MSA-400).

The Active Probes®, shown in Figure 4.3, is covered by a piezoelectric layer containing a stack of 0.25 μm Ti/Au, 3.5 μm ZnO, and 0.25 μm Ti/Au. The Ti/Au layers on the top and beneath ZnO layer act as electrodes which, along with the silicon

cantilever, construct a bimorph actuator. As the input voltage is applied to the pads at the fixed end of the beam, the expansion and contraction of the ZnO layer results in the transversal vibration of the Active Probes®.

The Active Probes® assembled on a chip is mounted on a *XYZ* stage to be adjusted within the laser light focus for measuring of beam motion (Figure 4.4). Using an optical microscope, the desired points on the surface of Active Probes® are precisely chosen to be scanned. When the electrical signals are applied to the system, the laser Doppler vibrometer measures the beam velocity at any given points through collecting and processing of backscattered laser light. In this study, a 10 Volt AC chirp signal with 500 kHz bandwidth is applied to the piezoelectric layer as the source of excitation.

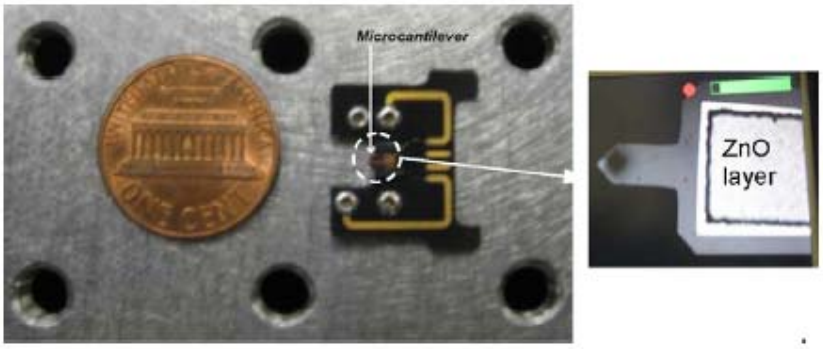

Figure 4.3. Comparison of the Veeco DMASP microcantilever beam size with a US penny.

Figure 4.5 demonstrates modal frequency response of the Active Probes®. As seen, the first three resonant frequencies of the probe are located within the applied frequency bandwidth with the values of 52.3, 203.0, and 382.5 kHz, respectively. Furthermore, the

corresponding mode shapes of Active Probes® are obtained by exciting the system in its resonant frequencies as depicted in Figure 4.6.

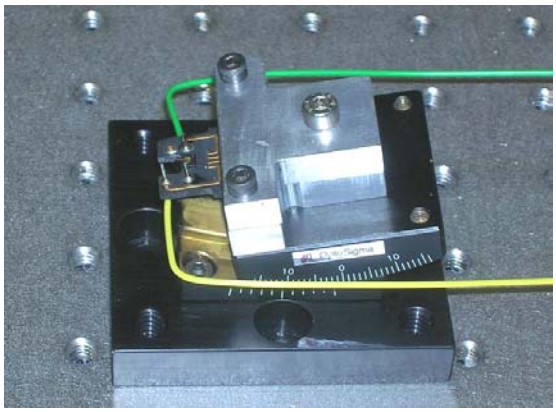

Figure 4.4. Experimental set-up for the measurement of the microcantilever tip.

In the following section, a modeling framework is proposed for the Active Probes® taking into account its discontinuities for precise modal characterization and frequency response analysis. To assess the effects of discontinuities on the frequency response and mode shapes of the system, results will be compared with those obtained from a uniform beam model.

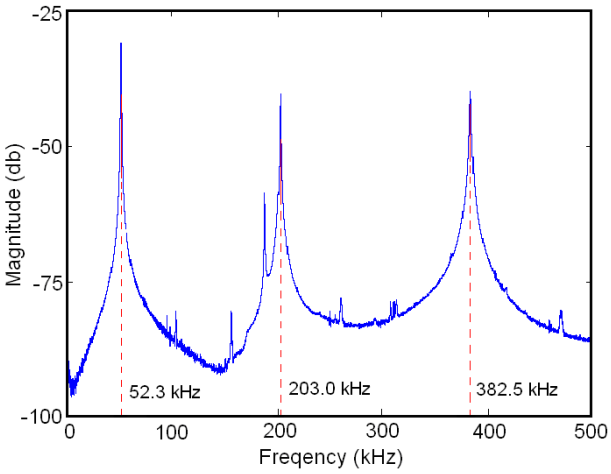

Figure 4.5. Modal frequency response of Active Probe tip transversal vibration.

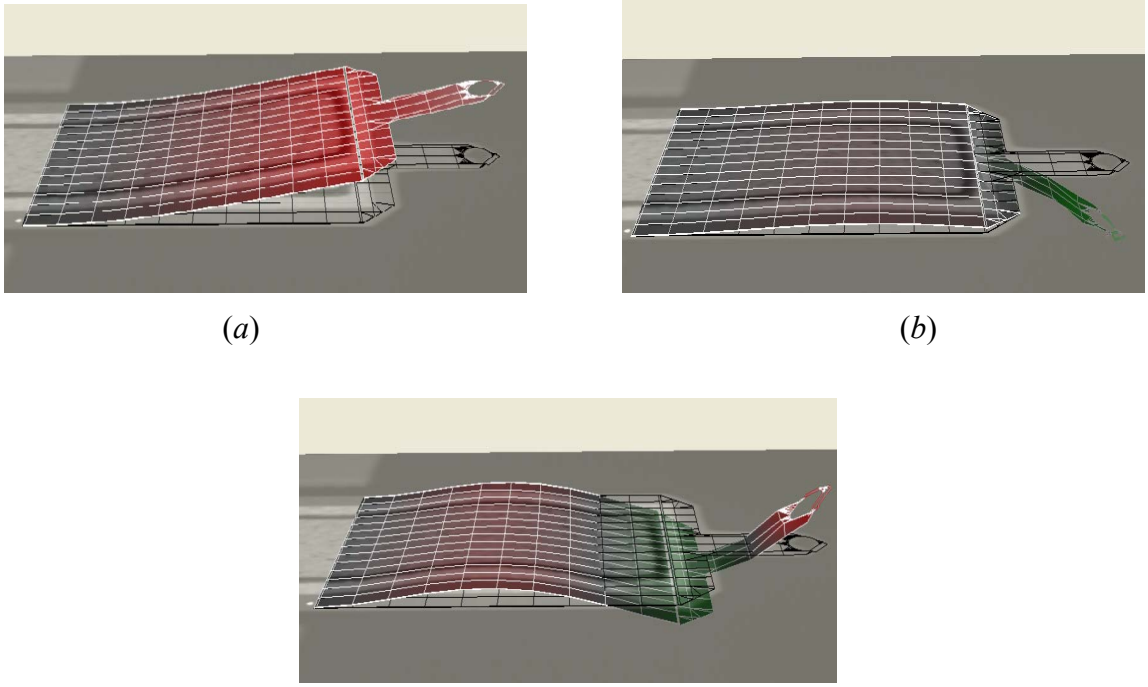

(*a*) (*b*)

(*c*)

Figure 4.6. 3D motion of Active Probes® at (*a*) first, (*b*) second, and (*c*) third resonant frequency.

4.3. Mathematical Modeling of Active Probes®

Consider a piezoelectrically-driven discontinuous microcantilever beam with its geometrical parameter depicted in Figure 4.7. Utilizing Euler-Bernoulli beam assumptions, the only non-zero component of strain can be expressed as [115]

$$\varepsilon_x = \begin{cases} -(y - y_n)\dfrac{\partial^2 w(x,t)}{\partial x^2} & \text{for } x \le l_1 \\ -y\dfrac{\partial^2 w(x,t)}{\partial x^2} & \text{for } x > l_1 \end{cases} \tag{4.1}$$

with $w(x,t)$ being the vertical component of displacement along y direction, and y_n being the neutral surface (measured along y-axis from y=0) in the composite (beam/piezoelectric layer) portion of the cantilever given by

$$y_n = \frac{1}{2}\frac{E^p t_p w_p (t_p + t_b)}{E^p t_p w_p + E^b t_b w_{b1}} \tag{4.2}$$

where E^b and E^p are the Young's modulus of the microcantilever and piezoelectric layer, respectively.

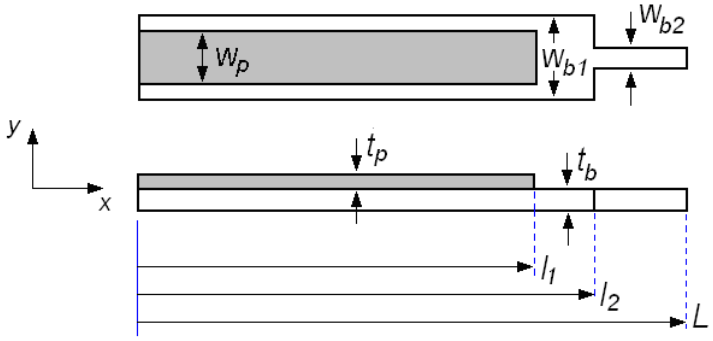

Figure 4.7. The schematic representation of microcantilever with an attached piezoelectric layer on its top surface.

Assuming one-dimensional deformation, the stress-strain relation for the beam can be written as

$$\sigma_x^b = E^b \varepsilon_x = -E^b y \frac{\partial^2 w(x,t)}{\partial x^2} \tag{4.3}$$

and for the piezoelectric portion can be expressed in the form of

$$\sigma_x^p = E^p (\varepsilon_x - d_{31}\frac{v(t)}{t_p}) = E^p \left(-(y - y_n)\frac{\partial^2 w(x,t)}{\partial x^2} - d_{31}\frac{v(t)}{t_p} \right) \tag{4.4}$$

where d_{31} is the coefficient of the converse piezoelectric effect, and $v(t)$ is the applied voltage to the piezoelectric layer. Inserting Eq. (4.1) into Eq. (4.4), the cross-sectional

bending moment acting at x distance from clamped end of the microcantilever cantilever can be expressed as

$$M(x,t) = -\int \sigma_x^p y dA = EI(x)\frac{\partial^2 w(x,t)}{\partial x^2} + \frac{1}{2} w_p E^p d_{31}(t_b + t_p) v(t) Q(x) \tag{4.5}$$

where

$$I(x) = I_p Q(x) + I_{b1} R(x) + I_{b2} S(x), \quad 0 \le x \le L$$

$$I_p = t_b y_n^2 w_{b1} - (t_p^2 + t_b t_p) y_n w_p + \frac{1}{3}(t_p^3 + \frac{3}{2} t_b t_p^2 + \frac{3}{4} t_b^2 t_p) w_p, \quad I_{b1} = \frac{w_{b1} t_b^3}{12}, \quad I_{b2} = \frac{w_{b2} t_b^3}{12}, \tag{4.6}$$

$$Q(x) = 1 - H(x - l_1), \quad R(x) = 1 - H(x - l_2), \text{ and } S(x) = H(x - l_2)$$

and $H(x)$ is the unit Heaviside function.

Eq. (4.5) demonstrates that the bending moment due to piezoelectric layer on the surface of the beam can be divided into a passive and active terms. The passive term (the first term in the right hand side of Eq. (4.5) is treated in the potential energy, while the active term (the second expression) is considered in the virtual work. In this regard and based on the pin-force model, the stress in the piezoelectric layer can be replaced by a concentrated bending moment acting at the end of the piezoelectric layer (as shown in Figure 4.8) which results in a uniform distribution of internal moment at composite portion of microcantilever as follows:

$$M_p(x,t) = -\frac{1}{2} w_p E^p d_{31}(t_b + t_p) v(t) Q(x) \tag{4.7}$$

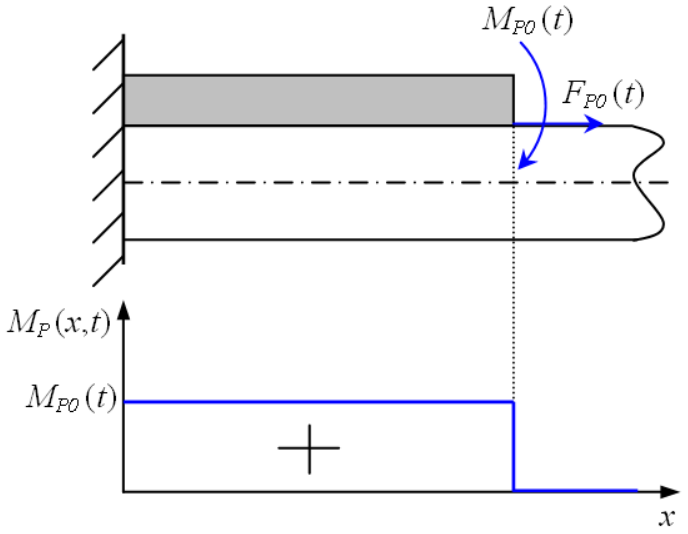

Figure 4.8. (top) Pin-force model for the composite portion of microcantilever, and (bottom) uniform distribution of internal moment along the microcantilever length.

Now, for the current configuration of Active Probe®, the governing partial differential equation (PDE) for the transverse vibration can be expressed as

$$\frac{\partial^2}{\partial x^2}(E(x)I(x)\frac{\partial^2 w}{\partial x^2}) + c(x)\frac{\partial w}{\partial t} + m(x)\frac{\partial^2 w}{\partial t^2} = \frac{\partial^2 M_p(x,t)}{\partial x^2} \tag{4.8}$$

where $c(x)$, $m(x)$, $E(x)$, and $I(x)$ are variable damping coefficient, mass per unit length, stiffness and moment of inertia, respectively.

For the reader's convenience, we briefly revisit the derivation of natural frequencies and mode shapes given in section 3.2.1. For the purpose of obtaining natural frequencies and mode shapes of the microcantilever, the free and un-damped conditions associated with the transverse vibration of the beam are given by

$$\frac{\partial^2}{\partial x^2}(E(x)I(x)\frac{\partial^2 w}{\partial x^2}) = -m(x)\frac{\partial^2 w}{\partial t^2} \tag{4.9}$$

Assuming that the solution of Eq. (4.9) is separable in time and space domains,

$$w(x,t) = \Phi(x)Q(t) \tag{4.10}$$

it can be rewritten in the form of

$$\frac{d^2}{dx^2}(E(x)I(x)\frac{d^2\Phi(x)}{dx^2}) = \omega^2 m(x)\Phi(x) \tag{4.11}$$

where ω is the natural frequency of the microcantilever.

In order to obtain an analytical solution for Eq. (4.11), the entire length of beam is divided into three uniform segments (see Figure 4.7) with two sets of continuity conditions at stepped points given by

$$(EI)_n \frac{d^4\phi_n(x)}{dx^4} = \omega^2 m_n \phi_n(x)\ , \quad l_{n\text{-}1} < x < l_n;\ \ n = 1,2,3;\ \ l_0 = 0 \text{ and } l_3 = L \tag{4.12}$$

The general solution for the above equation can be written as

$$\phi_n(x) = A_n \sin\beta_n x + B_n \cos\beta_n x + C_n \sinh\beta_n x + D_n \cosh\beta_n x \tag{4.13}$$

where $\beta_n^4 = \omega^2 \frac{m_n}{(EI)_n}$, and A_n, B_n, C_n, and D_n are the constants of integration determined by following boundary and continuity conditions:

$$\phi_1(0) = \frac{d\phi_1(0)}{dx} = 0 \tag{4.14}$$

$$\phi_n(l_n) = \phi_{n+1}(l_n) \tag{4.15}$$

$$\frac{d\phi_n(l_n)}{dx} = \frac{d\phi_{n+1}(l_n)}{dx} \tag{4.16}$$

$$(EI)_n \frac{d^2\phi_n(l_n)}{dx^2} = (EI)_{n+1} \frac{d^2\phi_{n+1}(l_n)}{dx^2} \tag{4.17}$$

$$(EI)_n \frac{d^3\phi_n(l_n)}{dx^3} = (EI)_{n+1} \frac{d^3\phi_{n+1}(l_n)}{dx^3} \tag{4.18}$$

$$\frac{d^2\varphi_3(L)}{dx^2} = \frac{d^3\varphi_3(L)}{dx^3} = 0 \tag{4.19}$$

Applying Eqs. (4.14-4.19) into Eq. (4.13), the characteristics matrix equation of system can be formed which is utilized to calculate system natural frequencies and mode shape coefficients by solving the corresponding eigenvalue problem [116]. Accordingly, the $(r)^{th}$ mode shape of the beam can be obtained as:

$$\phi^{(r)}(x) = \begin{cases} \phi_1^{(r)}(x) = A_1^{(r)} \sin\beta_1^{(r)}x + B_1^{(r)} \cos\beta_1^{(r)}x + C_1^{(r)} \sinh\beta_1^{(r)}x + D_1^{(r)} \cosh\beta_1^{(r)}x, & 0 \le x \le l_1 \\ \phi_2^{(r)}(x) = A_2^{(r)} \sin\beta_2^{(r)}x + B_2^{(r)} \cos\beta_2^{(r)}x + C_2^{(r)} \sinh\beta_2^{(r)}x + D_2^{(r)} \cosh\beta_2^{(r)}x, & l_1 \le x \le l_2 \\ \phi_3^{(r)}(x) = A_3^{(r)} \sin\beta_3^{(r)}x + B_3^{(r)} \cos\beta_3^{(r)}x + C_3^{(r)} \sinh\beta_3^{(r)}x + D_3^{(r)} \cosh\beta_3^{(r)}x, & l_2 \le x \le L \end{cases} \tag{4.20}$$

On the other hand, the equation of motion for the system can be expressed as [116]

$$\ddot{q}^{(r)}(t) + \sum_{s=1}^{\infty} \left\{ c_{rs} \dot{q}^{(s)}(t) \right\} + \omega_r^2 q^{(r)}(t) = f^{(r)}(t) \tag{4.21}$$

where

$$c_{rs} = \int_0^L c(x)\phi^{(r)}(x)\phi^{(s)}(x)dx = c\left\{ \int_0^{l_1} \phi_1^{(r)}(x)\phi_1^{(s)}(x)dx + \int_{l_1}^{l_2} \phi_2^{(r)}(x)\phi_2^{(s)}(x)dx + \int_{l_2}^{L} \phi_3^{(r)}(x)\phi_3^{(s)}(x)dx \right\}$$

$$f^{(r)}(t) = \int_0^L \frac{\partial^2 M_p(x,t)}{\partial x^2} \phi^{(r)}(x)dx \tag{4.22}$$

where $\phi^{(r)}(x)$ and $\phi^{(s)}(x)$ are r^{th} and s^{th} mode shapes of the microcantilever. Substituting Eq. (4.7) into Eq. (4.22) yields

$$
\begin{aligned}
f^{(r)}(t) &= -\frac{1}{2} w_p E^p d_{31} (t_b + t_p) v(t) \int_0^L Q''(x) \phi^{(r)}(x) dx \\
&= \frac{1}{2} w_p E^p d_{31} (t_b + t_p) v(t) \int_0^L H''(x - l_1) \phi^{(r)}(x) dx
\end{aligned}
\tag{4.23}
$$

For the second distributional derivative of the Heaviside function we have

$$
\int_0^L H''(x - l_1) \phi^{(r)}(x) dx = \int_0^L \delta'(x - l_1) \phi^{(r)}(x) dx = -\frac{d}{dx} \left(\phi^{(r)}(l_1) \right) \tag{4.24}
$$

where $\delta(\cdot)$ represents the Dirac delta function. Substituting Eq. (4.24) into Eq. (4.23) yields

$$
f^{(r)}(t) = U^{(r)} v(t) \quad \text{where} \quad U^{(r)} = -\frac{1}{2} \frac{d}{dx} \left(\phi^{(r)}(l_1) \right) w_p E^p d_{31} (t_b + t_p) \tag{4.25}
$$

The truncated *k*-mode description of the microcantilever Eq. (4.21) can now be presented in the following matrix form:

$$
\mathbf{M}\ddot{\mathbf{q}} + \mathbf{C}\dot{\mathbf{q}} + \mathbf{K}\mathbf{q} = \mathbf{F}\mathbf{u} \tag{4.26}
$$

where

$$
\begin{gathered}
\mathbf{M} = I_{k \times k}, \mathbf{C} = [c_{rs}]_{k \times k}, \mathbf{K} = [\omega_r^2 \delta_{rs}]_{k \times k}, \mathbf{q} = [q^{(1)}(t), q^{(2)}(t), \ldots, q^{(k)}(t)]_{k \times 1}^T, \\
\mathbf{F} = [U^{(1)}, U^{(2)}, \ldots, U^{(k)}]_{k \times 1}^T, \mathbf{u} = v(t)
\end{gathered}
\tag{4.27}
$$

The state-space representation of Eq. (4.24) is given by:

$$
\dot{\mathbf{X}} = \mathbf{A}\mathbf{X} + \mathbf{B}\mathbf{u} \tag{4.28}
$$

where

$$
\mathbf{A} = \begin{bmatrix} \mathbf{0} & \mathbf{I} \\ -\mathbf{M}^{-1}\mathbf{K} & -\mathbf{M}^{-1}\mathbf{C} \end{bmatrix}_{2k \times 2k}, \mathbf{B} = \begin{bmatrix} \mathbf{0} \\ \mathbf{M}^{-1}\mathbf{F} \end{bmatrix}_{2k \times 1}, \mathbf{X} = \begin{Bmatrix} \mathbf{q} \\ \dot{\mathbf{q}} \end{Bmatrix}_{2k \times 1} \tag{4.29}
$$

4.4. Theoretical and Experimental Vibration Analysis Comparisons

To compare the experimental mode shapes and natural frequencies with those obtained from the proposed model, exact values of system parameters are required. Although some of the parameters are given in the product catalogue, and some others can be measured through precision measurement devices such as our MSA-400, the presence of uncertainties associated with the parameters may drastically degrade model accuracy. Therefore, a system identification procedure is carried out here to fine-tune the parameter values for precise comparison with the experimentally obtained data.

The objective of system identification here is to minimize a constructed error function between the model and the actual system mode shapes and natural frequencies, simultaneously. The optimization variables comprise of microcantilever parameters and a set of scaling factors. In this regard, a number of points are selected along the Active Probes® for comparison of the mode shapes. The error function utilized for the system identification calculates the percentage of the average weighted error between the measured and evaluated natural frequencies and mode shapes at each selected point for a finite number of modes as follows:

$$E = \frac{1}{K}\left\{ W \sum_{r=1}^{K} \left(\frac{1}{P} \sum_{j=1}^{P} \left| \frac{\alpha_r w_{\max}^{(r)E}(x_j) - \phi^{(r)T}(x_j)}{\alpha_r w_{\max}^{(r)E}(x_j)} \right| \right) + (1-W) \sum_{r=1}^{K} \left| \frac{\omega_r^E - \omega_r^T}{\omega_r^E} \right| \right\} \times 100 \qquad (4.30)$$

where K is the number of modes, P represents the number of selected points on the microcantilever length, $0 < W < 1$ is a the weighing factor space, $\phi^{(r)T}(x_j)$ stands for the r^{th} theoretical mode shape evaluated at point x_j, $w_{\max}^{(r)E}(x_j)$ indicates the experimental

amplitude of point x_j at r^{th} resonant frequency, and α_r is an scaling optimization variable used to match r^{th} experimental resonant amplitude with the corresponding theoretical mode shape. Other optimization variables including parameters associated with microcantilever property and geometry (as listed in Table 4.1) are constrained within a limited range around the approximate values. The upper and lower bounds for the variables are selected in accordance with best guesses on the maximum possible amount of uncertainties in the approximate values.

To demonstrate the expected improvements through the proposed modeling framework, both uniform and discontinuous beam models are considered for the system identification. Optimization is carried out by selecting the first three modes of the system ($K = 3$), choosing 16 points on the cantilever length ($P = 16$), and setting the weighing factor $W = 0.5$ to equate the importance between the mode shapes and the resonant frequencies. A random optimization algorithm is then implemented for the parameters estimation. Random optimization is a class of heuristic algorithms which usually converges to the global solution within the search domain [117]. It is expected that the optimization does not converge to a desirable tolerance for the uniform beam model due to large discontinuities of the actual system.Table 4.1 demonstrates the initial (approximate) values of optimization variables, their imposed upper and lower bounds, and optimal values for the uniform and discontinuous microcantilever models, respectively. Figures 4.9 and 4.10 depict the first three mode shapes of the actual microcantilever beam along with those of the theoretical models. As seen from Figure 4.10, the mode shapes of the proposed discontinuous model match with the experimental

data vary closely when compared to those of the uniform model. Furthermore, the modal frequency responses show more accurate estimation of the system natural frequencies using the discontinuous beam theory (see Figure 4.10). Since the uniform beam assumption fails to accurately model the actual response of the Active Probes® for a multiple-mode operation, the discontinuous beam assumptions must be taken into account for the sake of modeling precision.

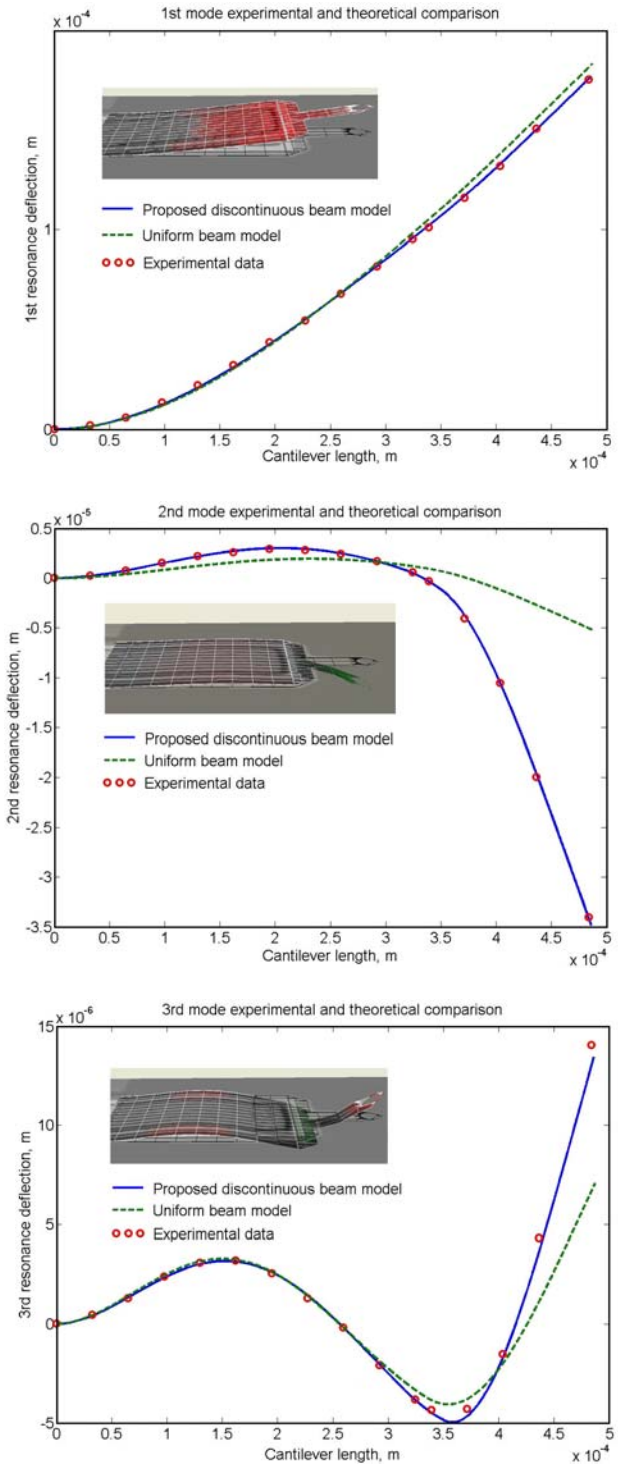

Figure 4.9. Active Probes® modal response experimental and theoretical comparisons for uniform and discontinuous beam models: (a) First mode shape, (b) second mode shape, and (c) third mode shape.

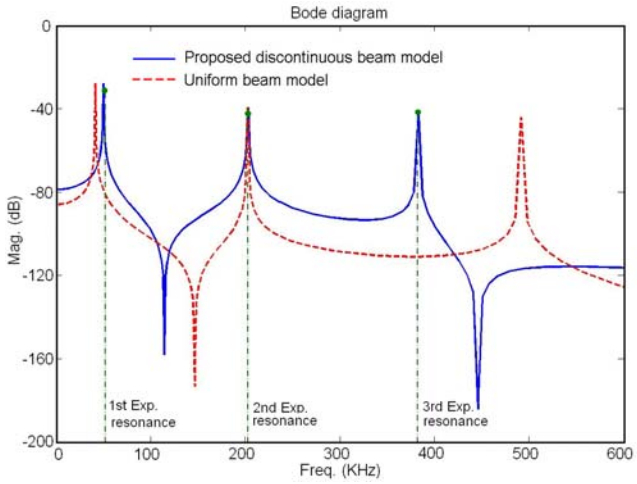

Figure 4.10. Active Probes®probe modal frequency response comparisons.

Table 4.1. Physical and numerical parameters used in system identification process: approximate parameter values, their upper and lower bounds, and the optimal solution for uniform and discontinuous beam model.

	Uniform beam model				Discontinuous beam model			
Parameters	Lower bound	Upper bound	Initial value	Optimal solution	Upper bound	Lower bound	Initial value	Optimal solution
$L(\mu m)$	485	487	486	486.7	485	487	486	485.9
$L_1(\mu m)$	-	-	-	-	315	330	325	315.0
$L_2(\mu m)$	-	-	-	-	350	370	360	350.0
$E_b(Gpa)$	50	200	105	154.1	50	200	105	140.2
$E_p(Gpa)$	50	200	104	75.1	50	200	104	102.2
$\rho_b(kg/m^3)$	2000	3500	2330	2528.9	2000	3500	2330	3177.0
$\rho_p(kg/m^3)$	5000	7000	6390	6974.1	5000	7000	6390	6782.9
$w_{b1}(\mu m)$	240	260	250	247.4	240	260	250	244.4
$w_{b2}(\mu m)$	-	-	-	-	50	60	55	54.3
$w_p(\mu m)$	120	150	130	135.2	120	150	130	140.8
$t_b(\mu m)$	2	5	4	4.3	2	5	4	3.4
$t_p(\mu m)$	2	5	4	2.9	2	5	4	2.1
α_1	200	800	500	278.9	200	800	500	454.9
α_2	5000	20000	10000	12967.0	5000	20000	10000	6595.1
α_3	5000	20000	10000	8536.4	5000	20000	10000	10028.9

4.5. Conclusions

Active Probes® are typically fabricated with intentional geometrical discontinuities due to the piezoelectric layer and sensing enhancement requirement. To remedy this complexity, a comperhensive framework was proposed for precise modeling, modal characterization and dynamic response analysis of Active Probes® with discontinuities in cross-section. This was achieved by considering Euler-Bernoulli beam assumptions and dividing the entire length of the Active Probes® into three uniform segments followed by applying appropriate continuity conditions. The electromechanical coupling of the piezoelectric layer was replaced with the equivalent force and moment using the well-established pin-force model. The governing equations of motion and their state-space representation were then formulated for dynamic response analysis. Results from experimental tests indicate significant enhancement on sensing accuracy using the proposed discontinuous beam model compared to a uniform model when a multiple-mode operation is desired.

CHAPTER FIVE

VIBRATION ANALYSIS OF VECTOR PIEZORESPONSE FORCE MICROSCOPY WITH COUPLED MOTIONS

5.1. Introduction

Progress in micro- and nanoscale electromechanical sensors and actuators has necessitated understanding of local piezoelectric properties at the scale of nanometer [118,119]. In this regard, rapid development in scanning probe microscopy (SPM)-based techniques made it possible to study these properties in the scale of grains, and produce controlled and localized modifications on the piezoelectric surface [120]. Among the SPM techniques, piezoresponse force microscopy (PFM) has evolved into a useful tool for this purpose due to ease of implementation, high resolution and its relatively insensitivity to topography [121-124].

PFM functions based on applying an external electrical field between a rear electrode on the piezoelectric sample and a conducting AFM tip. In the static mode, application of uniform electric field results in elongation or contraction of sample depending on the polar direction and applied field. From induced strain through electric field, the piezoelectric coefficient of sample can be determined. However, the domain imaging based on the detection of static deformation is difficult. The reason is that the separation of static piezoresponse deflection and deflection signal due to surface roughness is not an easy task [125]. To improve the sensitivity of the static mode, a dynamic piezoresponse image method based on the voltage modulation approach has been introduced [126-128].

In this method, a periodic bias external electrical field is applied to a rear electrode on the sample and a conducting AFM tip. The periodic bias voltage induces local piezoelectric vibration which can be detected by AFM tip. These vibrations depend on the orientation of polarization vector, and arise due to converse piezoelectric effect [129]. The phase of electromechanical response of surface provides information about the direction of polarization of surface, while the amplitude of vibration yields to information about the piezoelectric coefficients [130,131].

In general case, when a bias voltage is applied to a sample with arbitrary crystallographic orientation, the response of the piezoelectric material results in both in-plane and normal components of displacement [132]. Hence, the microcantilever can vibrate in all three directions which results in a coupled bending-longitudinal-torsional motion of microcantilever. The coupled motions in vector PFM occur due to: i) presence of friction force in the tip-sample junction and ii) geometrical coupling originated from the rotation of tip at the free end of microcantilever due to transversal/lateral bending of microcantilever.

Because of practical importance of coupled motions, many studies have been reported on the effect of coupling terms on the natural frequencies, mode shapes and response of the beam [133-137]. Neglecting the effect of wraping, Dokumaci [138] obtained the coupled natural frequencies of the cantilever beam which is then extended for the wrapping problem by Bishop *et al* [139]. A dynamic stiffness matrix analysis approach was then introduced by Banerjee *et al* [140] to determine the natural frequencies and mode shapes of the coupled Euler-Bernoulli beam. The coupled vibrations of beams

including warping, shear deformation and rotary inertia effects were studied by Bercin and Tanaka [141]. The coupled free and forced vibrations of a beam with tip and in span attachments were investigated by Gokdag and Kopmaz [142]. And recently, Mahmoodi and Jalili has investigated the nonlinear vertical-torsion coupled vibration of microcantilever sensors [50]. The results obtained from these studies have addressed the presence of bending, longitudinal or torsional mode natural frequency in the vibration spectra of the other modes.

Motivated by these considerations, the objective of this study is to acquire a comprehensive model for dynamic behavior of vector PFM system under applied combined electrical and mechanical loadings. For this purpose, PFM is considered as a suspended microcantilever beam with a tip mass in contact with a piezoelectric material. Furthermore, the material properties are expressed in two forms; Kelvin-Voigt model for viscoelstic representation of material and piezoelectric force acting on the tip as a result of response of material to applied electric field. Since the application of bias voltage to the tip results in the surface displacement in both normal and in-plane directions [143], the microcantilever is considered to vibrate in all three directions with coupled transversal/longitudinal and lateral/torsional motions.

In this model, the effect of friction between sample and tip is also taken into account. Through an energy method, it is seen that the PFM system can be governed by a set of partial differential equations (PDE) along with non-homogeneous and coupled boundary conditions. A general formulation is then derived for the mode shape and frequency response of the system. Finally, using the method of assumed modes, the governing

ordinary differential equations (ODEs) of the system and its state-space representation are derived under applied external voltage. Results demonstrate that mode shape, natural frequency and time response of microcantilever are heavily dependent upon the coupling terms arising from viscoelastic and piezoelectric properties of samples. It is shown that different materials show various constraints at the end of microcantilever. Materials with higher stiffness can convert clamped-free condition of microcantilever to clamped-hinged condition. Moreover, it is shown that the coupled damping terms of material in the tip-sample junction significantly affects the time response of the system.

5.2. PFM Operational Modes and Function

PFM functions based on application of a periodic bias external electrical field between a rear electrode on the sample and a conducting AFM tip (Figure 5.1). The periodic bias voltage is $V_{tip} = V_{dc} + V_{ac}Cos(wt)$ in which V_{dc} is the DC component of the bias voltage used to measure the static deflection of the microcantilever. $V_{ac}Cos(wt)$ is a small AC voltage which is applied to the tip in order to induce local piezoelectric vibration. The piezoresponse of the surface can be detected as the first harmonic component of bias induced tip deflection $d = d_0 + ACos(wt + \varphi)$. The amplitude of vibration, A, provides information about the piezoelectric coefficients of surface, while the phase of electromechanical response of surface, φ, yields information about the polarization direction of surface [124 and 130].

Utilizing Hertzian contact mechanics at the tip-surface junction, the relation between the indentation load P, indenter voltage V, and indentation depth h can be expressed as [143]

$$h = \frac{a^2}{R} + \frac{2\beta}{3\alpha}V \quad \text{and} \quad P = \alpha\frac{a^3}{R} - \beta a V \tag{5.1}$$

where α and β are elastic and piezoelectric properties of material, respectively, R is the tip radius and a is the contact radius. In this study, based on Eq. (5.1), the behavior of sample is divided into two parts; viscoelastic and piezoelectric. The viscoelastic response of material against indentation force is modeled as a spring and damper at all three directions, while the piezoresponse of sample is considered as a resistance force, F_{tip}, at the free end of cantilever.

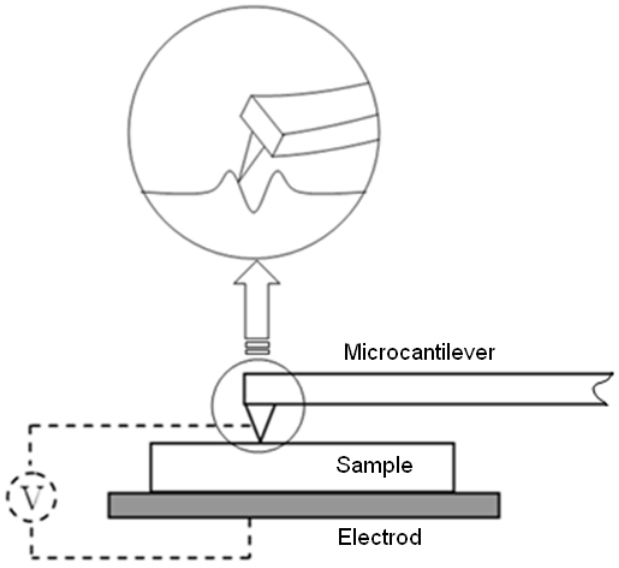

Figure 5.1. A schematic of tip-sample junction in the PFM system.

Figure 5.2 depicts the schematic of mechanical equivalent circuit of PFM. One end of the beam is clamped to the base position, while the tip is attached to the free end of the beam. The sample and tip are in the contact mode and any change in the topography of surface will affect the indentation depth of indenter. To avoid this, the boundary control input force, $f(t)$, is used at the base unit. In general case, when a bias is voltage applied to a sample with arbitrary crystallographic orientation, the response of the piezoelectric material results in both in-plane and normal components of displacement [132]. For this reason, the beam is considered to vibrate in all three directions. The free end of beam with the equivalent tip mass is connected to springs and dampers in the vertical, longitudinal and lateral directions which represent the viscoelastic resistance of material to tip movement. It is obvious that lateral and vertical components of viscoelastic response acting on the cantilever result in bending in these directions, while in the longitudinal direction the response of material is an axial force acting at the tip mass. Moreover, the piezoresponse of material are considered as F_{tip} in all three directions (i.e., $F_{tip\text{-}x}$, $F_{tip\text{-}y}$ and $F_{tip\text{-}z}$). In our proposed model, the height of the tip is also taken into account. As a result, piezoresponse of material acting at the end of tip causes an external moment and torsion in the longitudinal and lateral directions, respectively. Figure 5.3 depicts the longitudinal and lateral piezoelectric force acting at the tip of microcantilever. In this study, the effect of friction force present inthe tip and sample interface as well as in the longitudinal and lateral directions are considered as base excitations given by

$$u_{fric-x} = \Delta x = \frac{\mu_x F_{tip-z}}{k_x} \quad \text{and} \quad u_{fric-y} = \Delta y = \frac{\mu_y F_{tip-z}}{k_y} \quad k_x = k_y \neq 0 \tag{5.2}$$

where μ_x and μ_y are the coefficients of friction in x and y directions, respectively. This indicates that the friction force in the PFM is a function of applied voltage and time.

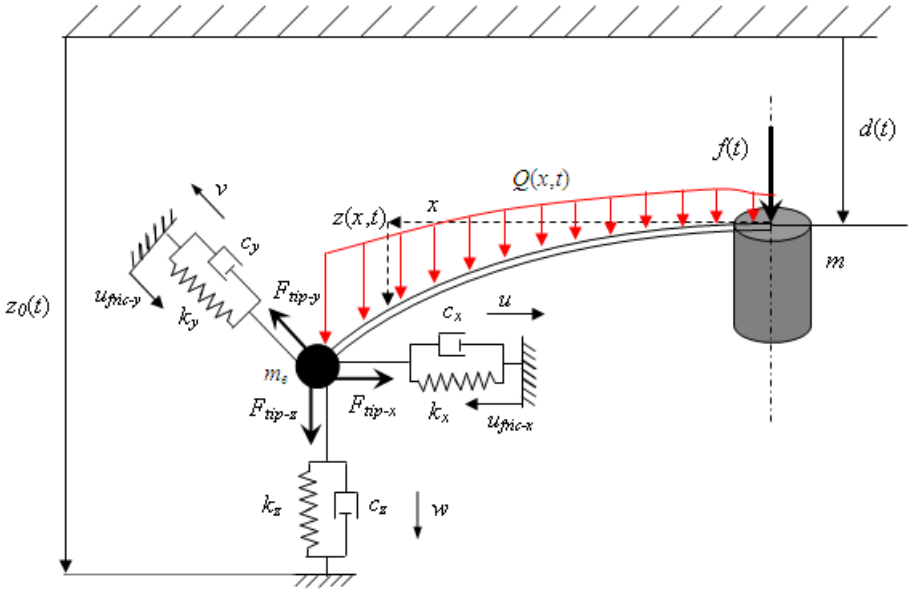

Figure 5.2. A proposed schematic representation of PFM systeme.

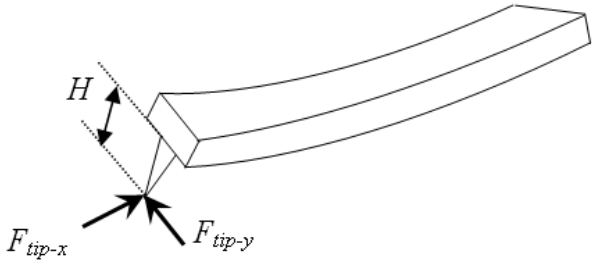

Figure 5.3. A schematic of microcantilever subjected to longitudinal and lateral piezoelectric forces.

5.3. Distributed-Parameters Modeling of PFM

In this section, a general distributed-parameters base modeling approach is utilized for the analysis of dynamic behavior of PFM. For this purpose, the Euler-Bernoulli model is used for microcantilever beam configuration as shown in Figure 5.2. One end of the beam is clamped to the base position assembly with the displacement of $d(t)$ and the total mass of m. The tip with the mass of m_e is attached to the free end of the beam. The microcantilever beam has rigidity EI, mass moment of inertia J, linear density ρ and the length L. The equivalent spring constants of sample are k_x , k_y and k_z , and damping coefficients are C_x , C_y and C_z in x, y, z directions, respectively. The friction coefficients between sample and tip are μ_x and μ_y for in-plane motions. In this work, the effect of viscous air damping and structural damping in the microcantilever beam are also taken into account.

The total kinetic energy of the system can now be expressed as

$$KE = \frac{1}{2}m(\dot{d}(t))^2 + \frac{1}{2}\int_0^L \rho\left[\left(\dot{d}(t) + \dot{w}_t(x,t)\right)^2 + v_t^2(x,t) + u_t^2(x,t)\right]dx + \frac{1}{2}m_e\left[\left(\dot{d}(t) + \dot{w}_t(L,t)\right)^2 + v_t^2(L,t) + u_t^2(L,t)\right] + \frac{1}{2}\int_0^L J\theta_t^2(x,t)dx \tag{5.3}$$

where subscripts $(\cdot)_t$ and $(\cdot)_x$ indicate partial derivatives with respect to the time variable t and position variable x, respectively. $w(x,t)$, $u(x,t)$ and $\mathrm{v}(x,t)$ are the vertical, longitudinal and lateral displacements of beam, respectively. $\theta(x,t)$ presents the torsion along x-axis due to applied voltage and friction. In the above equation, the first term is the kinetic energy of the base, the second and third terms are that of beam and tip,

respectively. The last term presents the kinetic energy due to torsion of beam along *x*-axis.

The total potential energy of the system can be written as

$$PE = \left\{ \frac{1}{2}\int_0^L EI_{yy} w_{xx}^2(x,t)dx + \frac{1}{2}\int_0^L EI_{zz} v_{xx}^2(x,t)dx \right\} + \frac{1}{2}\int_0^L EAu_x^2(x,t)dx + \frac{1}{2}\int_0^L C_T \theta_x^2(x,t)dx$$
$$+ \left\{ \frac{1}{2}k_x[(u(L,t) + u_{fric-x}) + w_x(L,t)H]^2 + \frac{1}{2}k_y[(v(L,t) + u_{fric-y}) - \theta H]^2 + \frac{1}{2}k_z w^2(L,t) \right\} \tag{5.4}$$

where H is the height of tip at the free part of beam, and C_T is the torsional stiffness of beam. The above equation indicates that potential energy consists of four parts: the potential energy of the beam due to bending in vertical and lateral direction (first term), the potential energy of the beam due to longitudinal movement (second term), torsion along *x*-axis (third term), and the elastic potential energy of sample in the longitudinal, lateral and vertical directions, respectively (last term). In addition to tip displacement at the free end of microcantilever, the elastic potential of sample in the longitudinal and lateral directions include base excitation terms due to presence of friction and geometrical coupling due to rotation of tip as a result of transversal and lateral bending. In the above equation, $w_x(L,t)H$ presents the geometrical coupling term between transversal and longitudinal direction and θH indicates coupling between lateral bending and torsional displacement. In this model, the friction effect is implemented as a base excitation in the

elastic potential energy of sample. The base displacement of sample is directly related to piezoelectric properties of material obtained in Eq. (5.2).

The boundary control input force $f(t)$ at the base unit, the piezoelectric force, capacitive forces between tip cantilever assembly and surface $Q(x,t)$, viscous air damping B, and structural damping C are all considered in the virtual work. For simplicity and without loss of generality, it is assumed that viscous air damping and structural damping coefficients in the transversal and lateral directions are similar. Moreover, the piezoelectric and damping forces acting at the tip-sample junction are considered as an equivalent impulse (Δ) forces acting at very small distance (ε) from end of microcantilever. This approach can ease the subsequent mathematical procedures used to homogenize the boundary conditions (BCs). More especially, utilizing this approach the damping terms in the BCs can be removed and transferred into the equations of motion. However, the conventional method is to consider damping terms in the BCs which make the nature of BCs time-dependent. In this case, the eigenvalues and subsequent mode shapes of the system become complex, which are more complicated to deal with compared to the former alternative proposed here. Moreover, the representation of the entire system in the state-space for a control purposes is more involved and not trivial.

Considering all these points, the virtual work of the system can be expressed as

$$
\begin{aligned}
\delta W^{nc} &= f(t)\delta d(t) + \int_0^L Q(x,t)\delta w(x,t)dx - \{B\int_0^L w_t(x,t)\delta w(x,t)dx + \\
&C\int_0^L w_{xt}(x,t)\delta w(x,t)dx + B\int_0^L v_t(x,t)\delta v(x,t)dx + C\int_0^L v_{xt}(x,t)\delta v(x,t)dx\} + \\
&\{\int_0^L \Delta(x-L+\varepsilon)F_{tip-z}(t)\delta w(x,t)dx + \int_0^L \Delta(x-L+\varepsilon)F_{tip-y}(t)\delta v(x,t)dx + \\
&\int_0^L \Delta(x-L+\varepsilon)F_{tip-x}(t)\delta u(x,t)dx\} + \{\int_0^L \Delta(x-L+\varepsilon)F_{tip-x}(t)H\delta w_x(x,t)dx + \\
&\int_0^L \Delta(x-L+\varepsilon)F_{tip-y}(t)H\delta\theta(x,t)dx\} - \{C_z\int_0^L \Delta(x-L+\varepsilon)w_t(L,t)\delta w(x,t))dx \\
&+C_x\int_0^L \Delta(x-L+\varepsilon)[u_t(L,t)+u_{t,fric-x}+w_{xt}(L,t)H]\delta u(x,t)dx \\
&+C_y\int_0^L \Delta(x-L+\varepsilon)[v_t(L,t)+u_{t,fric-y}-\theta_t(L,t)H]\delta v(x,t)dx\} \\
&-\{C_xH\int_0^L \Delta(x-L+\varepsilon)[u_t(L,t)+u_{t,fric-x}+w_{xt}(L,t)H]\delta w_x(x,t))dx \\
&+C_yH\int_0^L \Delta(x-L+\varepsilon)[v_t(L,t)+u_{t,fric-y}-\theta_t(L,t)H]\delta\theta(x,t))dx\}
\end{aligned}
\tag{5.5}
$$

whre $\delta(\cdot)$ denotes variation of arguments. The above equation expresses the virtual work of the system due to; boundary control input force (first term), capacitive forces between tip-cantilever assembly and surface (second term), microcantilever damping terms in transversal and lateral directions (third term), piezoelectric forces of sample in all three directions (fourth term), moment and torsion due to piezoelectric force in the longitudinal and lateral directions (fifth term), material damping forces (sixth term), and moment and torsion due to material damping terms in the longitudinal and lateral directions (last term).

The Hamilton's principle can be expressed as

$$\int_{t_1}^{t_2} \delta(KE - PE + W^{nc})dt = 0 \tag{5.6}$$

Substituting eqs. (5.3-5.5) into Eq. (5.6) yields the following PDEs for the motion of the PFM:

-for vertical vibration of microcantilever:

$$\begin{aligned}&\rho[\ddot{d}(t) + w_{tt}(x,t)] + EI_{yy}w_{xxxx}(x,t) + Bw_t(x,t) + Cw_{xt}(x,t) - \\ &C_x H\Delta_x(x-L+\varepsilon)[u_t(L,t) + w_{xt}(L,t)] + C_z\Delta(x-L+\varepsilon)w_t(L,t) = \\ &Q(x,t) - \Delta_x(x-L+\varepsilon)HF_{tip-x}(t) + C_x H\Delta_x(x-L+\varepsilon)u_{t,fric-x} + \Delta(x-L+\varepsilon)F_{tip-z}(t)\end{aligned} \tag{5.7}$$

-for base motion:

$$m\ddot{d}(t) + \int_0^L \rho[\ddot{d}(t) + w_{tt}(x,t)]dx + m_e[\ddot{d}(t) + w_{tt}(L,t)] = f(t) \tag{5.8}$$

-for lateral vibration of microcantilever:

$$\begin{aligned}&\rho v_{tt}(x,t) + EI_{zz}v_{xxxx}(x,t) + Bv_t(x,t) + Cv_{xt}(x,t) + \\ &C_y\Delta(x-L+\varepsilon)[v_t(L,t) - H\theta_t(L,t)] = \Delta(x-L+\varepsilon)F_{tip-y}(t) - C_y\Delta(x-L+\varepsilon)u_{t,fric-y}\end{aligned} \tag{5.9}$$

-for torsion of microcantilever:

$$\begin{aligned}&J\theta_{tt}(x,t) - C_T\theta_{xx}(x,t) + C_y H\Delta(x-L+\varepsilon)[v_t(L,t) - H\theta_t(L,t)] = \\ &\Delta(x-L+\varepsilon)HF_{tip-y}(t) - C_y H\Delta(x-L+\varepsilon)u_{t,fric-y}\end{aligned} \tag{5.10}$$

-for longitudinal vibration of microcantilever:

$$\begin{aligned}&\rho u_{tt}(x,t) - EAu_{xx}(x,t) + C_x\Delta(x-L+\varepsilon)[u_t(L,t) + Hw_{xt}(L,t)] = \\ &\Delta(x-L+\varepsilon)F_{tip-x}(t) - C_x\Delta(x-L+\varepsilon)u_{t,fric-x}\end{aligned} \tag{5.11}$$

with following boundary conditions (BCs)

$$m_e[\ddot{d}(t) + w_{tt}(L,t)] - EI_{yy} w_{xxx}(L,t) + k_z w(L,t) = 0 \tag{5.12}$$

$$m_e v_{tt}(L,t) - EI_{zz} v_{xxx}(L,t) + k_y (v(L,t) - \theta(L,t)H) = -k_y u_{fric-y} \tag{5.13}$$

$$m_e u_{tt}(L,t) + EAu_x(L,t) + k_x (u(L,t) + w_x(L,t)H) = -k_x u_{fric-x} \tag{5.14}$$

$$EI_{yy} w_{xx}(L,t) - k_x H(u(L,t) + w_x(L,t)H) = k_x H u_{fric-x} \tag{5.15}$$

$$C_T \theta_x(L,t) - k_y H(v(L,t) - H\theta(L,t)) = -k_y H u_{fric-y} \tag{5.16}$$

and

$$w(0,t) = w_x(0,t) = v_{xx}(L,t) = v(0,t) = v_x(0,t) = u(0,t) = \theta(0,t) = 0 \tag{5.17}$$

The above equations indicate that the transversal bending is coupled to longitudinal displacement and lateral bending is coupled to torsional motion of microcantilever through friction and piezoelectric forces acting at the end of beam (the terms in the right hand side of Eqs. (5.7-5.11)). Moreover, the BCs for those coupled motions are also coupled.

5.4. Assumed Mode Model Expansion

In order to numerically investigate the obtain equations of motion, we utilize assuming mode model (AMM) to discretize the original PDEs into the ordinary differential equations (ODEs). Since boundary conditions in Eqs. (5.13-5.16) are non-homogeneous, a new set of variables are defined in order to obtain homogenized boundary conditions. Then, assuming that variables are separable, a set of ordinary equations is obtained for different directions.

5.4.1. Coupled Transversal Bending-Longitudinal Displacement:

Equations (5.14 and 5.15) indicate that the transversal displacement of microcantilever is coupled to longitudinal motion through the BCs which are not homogeneous. To remedy this complexity, the BCs should be first homogenized. For this purpose, two new variables z and G are introduced with the following expressions.

$$w(x,t) = z(x,t) - u_{fric-x} F_1(x) \tag{5.18}$$

$$u(x,t) = G(x,t) - u_{fric-x} F_2(x) \tag{5.19}$$

where $F_i(x)$ (i=1,2) are geometrical functions. To determine these functions, Eqs. (5.18) and (5.19) are substituted into Eqs. (5.12, 5.14 and 5.15). Then, all BCs are forced to be homogenized simultaneously in the new coordinates. These result in the following conditions on geometrical functions F_1 and F_2 as

$$F_1(0) = F'_1(0) = F_1(L) = F_1'(L) = F_1'''(L) = 0 \quad \text{and} \quad F_1''(L) = -\frac{k_x H}{EI_{y-y}} \tag{5.20-a}$$

$$F_2(0) = F_2'(0) = F_2(L) = 0 \quad \text{and} \quad F_2'(L) = \frac{k_x}{EA} \tag{5.20-b}$$

These geometrical functions can now be obtained as

$$F_1(x) = \frac{k_x H}{EI_{y-y} L^3}\left(x^5 - \frac{7}{2} L x^4 + 4L^2 x^3 - \frac{3}{2} L^3 x^2 \right) \tag{5.21-a}$$

$$F_2(x) = \frac{k_x}{EAL}(x^2 - Lx) \tag{5.21-b}$$

Now, applying Eqs. (5.18) and (5.19) into the original equations of motion in the vertical and longitudinal directions (5.7, 5.8 and 5.11), the new PDEs can be written as

$$\rho[\ddot{d}(t)+z_{tt}(x,t)]+EI_{yy}z_{xxxx}(x,t)+Bz_t(x,t)+Cz_{xt}(x,t)- \\ C_xH\Delta_x(x-L+\varepsilon)[G_t(L,t)+z_{xt}(L,t)]+C_z\Delta(x-L+\varepsilon)z_t(L,t)=\Pi_1(x,t) \tag{5.22-a}$$

where

$$\Pi_1(x,t)=Q(x,t)-\Delta_x(x-L+\varepsilon)HF_{tip-x}(t)+C_xH\Delta_x(x-L+\varepsilon)u_{t,fric-x}+ \\ \Delta(x-L+\varepsilon)F_{tip-z}(t)+\rho u_{tt,fric-x}F_1(x)+EI_{yy}u_{fric-x}F_1''(x)+Bu_{t,fric-x}F_1(x)+ \\ Cu_{t,fric-x}F_1'(x)-C_xH\Delta_x(x-L+\varepsilon)u_{t,fric-x}[F_2(L)+F_1'(L)]+C_z\Delta(x-L+\varepsilon)u_{t,fric-x}F_1(L) \tag{5.22-b}$$

$$m\ddot{d}(t)+\int_0^L\rho[\ddot{d}(t)+z_{tt}(x,t)]dx+m_e[\ddot{d}(t)+z_{tt}(L,t)]=\Pi_2(x,t) \tag{5.23-a}$$

where

$$\Pi_2(x,t)=f(t)+\int_0^L\rho u_{tt,fric-x}F_1(x)dx+m_eu_{tt,fric-x}F_1(L) \tag{5.23-b}$$

$$\rho G_{tt}(x,t)-EAG_{xx}(x,t)+C_x\Delta(x-L+\varepsilon)[G_t(L,t)+Hz_{xt}(L,t)]=\Pi_3(x,t) \tag{5.24-a}$$

where

$$\Pi_3(x,t)=\Delta(x-L+\varepsilon)F_{tip-x}(t)-C_x\Delta(x-L+\varepsilon)u_{t,fric-x}+\rho u_{tt,fric-x}F_2(x)- \\ EAu_{fric-x}F_2''(x)+C_x\Delta(x-L+\varepsilon)u_{t,fric-x}[F_2(L)+HF_1'(L)] \tag{5.24-b}$$

with the following BCs:

$$m_e[\ddot{d}(t)+w_{tt}(L,t)]-EI_{yy}w_{xxx}(L,t)+k_zw(L,t)=0 \tag{5.25}$$

$$m_eu_{tt}(L,t)+EAu_x(L,t)+k_x(u(L,t)+w_x(L,t)H)=0 \tag{5.26}$$

$$EI_{yy}w_{xx}(L,t)-k_xH(u(L,t)+w_x(L,t)H)=0 \tag{5.27}$$

$$w(0,t)=w_x(0,t)=u(0,t)=0 \tag{5.28}$$

Now utilizing above equations, the natural frequencies and mode shapes of microcantilever for coupled motion can be obtained.

5.4.1.1. Frequency Equation, Orthogonality Conditions and Mode Shapes

In order to obtain the natural frequencies and modal shapes of the system, the eigenvalue problem associated with the transversal/longitudinal vibration of beam is obtained through applying free and undamped conditions in Eqs. (5.22-1) and (5.24-1), which results in

$$\rho z_{tt}(x,t) + EI_{yy} z_{xxxx}(x,t) = 0 \tag{5.29}$$

and

$$\rho G_{tt}(x,t) - EAG_{xx}(x,t) = 0 \tag{5.30}$$

The separation of variables can be assumed in the form of

$$z(x,t) = \Phi(x)e^{i\omega t} \quad \text{and} \quad G(x,t) = \Lambda(x)e^{i\omega t} \tag{5.31}$$

where $\Phi(x)$ and $\Lambda(x)$ are the modal shapes of the microcantilever beam with a tip mass and ω is the natural frequency of the system. Applying Eq. (5.31) into Eqs. (5.29) and (5.30) results in the following differential equations:

$$\Phi''''(x) - \lambda^4 \Phi(x) = 0 \tag{5.32}$$

$$\Lambda''(x) + \xi^2 \Lambda(x) = 0 \tag{5.33}$$

where

$$\lambda^4 = \frac{\rho\omega^2}{EI_{yy}} \quad \text{and} \quad \xi = \sqrt{I/A}\lambda^2 \tag{5.34}$$

The solutions for Eqs. (5.32 and 5.33) can be written, respectively, as

$$\Phi(x) = K_1[\sin(\lambda x) - \sinh(\lambda x)] + K_2[\cos(\lambda x) - \cosh(\lambda x)] \tag{5.35}$$

$$\Lambda(x) = K_3 \sin(\lambda^2 \sqrt{I/A})x \tag{5.36}$$

where K_1 , K_2 and K_3 are coefficients of mode shapes to be determined.

Inserting Eqs. (5.35) and (5.36) into BCs. (5.25-5.27), the results can be written in the matrix form as

$$\begin{bmatrix} A_{11} & A_{12} & A_{13} \\ A_{21} & A_{22} & A_{23} \\ A_{31} & A_{32} & A_{33} \end{bmatrix} \begin{bmatrix} K_1 \\ K_2 \\ K_3 \end{bmatrix} = 0 \tag{5.37}$$

where

$$A_{11} = -EI_{yy}\lambda^3 \Phi_1'''(L) - (m_e\omega^2 - k_z)\Phi_1(L)$$

$$A_{12} = -EI_{yy}\lambda^3 \Phi_2'''(L) - (m_e\omega^2 - k_z)\Phi_2(L)$$

$$A_{13} = 0$$

$$A_{21} = -\frac{EI_{yy}}{H}\lambda^2 \Phi_1''(L)$$

$$A_{22} = -\frac{EI_{yy}}{H}\lambda^2 \Phi_2''(L)$$

$$A_{23} = -m_e\omega^2 \sin \xi L + EA\xi \cos \xi L$$

$$A_{31} = \frac{EI_{yy}}{H}\lambda^2 \Phi_1''(L) + k_x H \lambda \Phi_1'(L)$$

$$A_{32} = \frac{EI_{yy}}{H}\lambda^2 \Phi_2''(L) + k_x H \lambda \Phi_2'(L)$$

$$A_{33} = k_x \sin \xi L$$

and

$$\Phi_1(L) = \Phi_2'''(L) = \sin \lambda L - \sinh \lambda L$$

$$\Phi_1'(L) = \Phi_2(L) = \cos \lambda L - \cosh \lambda L$$

$$\Phi_1''(L) = \Phi_2'(L) = -\sin \lambda L - \sinh \lambda L$$

$$\Phi_1'''(L) = \Phi_2''(L) = -\cos \lambda L - \cosh \lambda L$$

The frequency equation can now be obtained by equating the determinant of Eq. (5.37) to zero which yields:

$$\begin{aligned}
&-EI_{yy}\lambda^3\Phi_1'''(L)\{-\frac{EI_{yy}}{H}k_x\lambda^2\Phi_2''(L)\sin(\xi L)+m_e\omega^2\frac{EI_{yy}}{H}\lambda^2\sin(\xi L)\Phi_2''(L)+\\
&m_e\omega^2\lambda k_x H\sin(\xi L)\Phi_2'(L)-E^2\frac{AI_{yy}}{H}\xi\cos(\xi L)\lambda^2\Phi_2''(L)-EAk_xH\lambda\xi\cos(\xi L)\Phi_2'(L)\}+\\
&(m_e\omega^2-k_z)\{\frac{EI_{yy}}{H}\lambda^2\sin(\xi L)\Phi_2''(L)\Phi_1(L)(k_x-m_e\omega^2)-m_e\omega^2\lambda k_xH\sin(\xi L)\Phi_2'(L)\Phi_1(L)+\\
&E^2\frac{AI_{yy}}{H}\xi\cos(\xi L)\lambda^2\Phi_2''(L)\Phi_1(L)+EAk_xH\lambda\xi\cos(\xi L)\Phi_2'(L)\Phi_1(L)\}+\\
&EI_{yy}\lambda^3\Phi_2'''(L)\{-\frac{EI_{yy}}{H}\lambda^2\Phi_1''(L)k_x\sin(\xi L)+m_e\omega^2\frac{EI_{yy}}{H}\lambda^2\sin(\xi L)\Phi_1''(L)+\\
&m_e\omega^2\lambda k_xH\sin(\xi L)\Phi_1'(L)-E^2\frac{AI_{yy}}{H}\xi\cos(\xi L)\lambda^2\Phi_1''(L)-EAk_xH\lambda\xi\cos(\xi L)\Phi_1'(L)\}-\\
&(m_e\omega^2-k_z)\{\frac{EI_{yy}}{H}\lambda^2\sin(\xi L)\Phi_1''(L)\Phi_2(L)(k_x-m_e\omega^2)-m_e\omega^2\lambda k_xH\sin(\xi L)\Phi_1'(L)\Phi_2(L)+\\
&E^2\frac{AI_{yy}}{H}\xi\cos(\xi L)\lambda^2\Phi_1''(L)\Phi_2(L)+EAk_xH\lambda\xi\cos(\xi L)\Phi_1'(L)\Phi_2(L)\}=0
\end{aligned} \tag{5.38}$$

In order to determine the coefficients of mode shapes, K_1 and K_3 can be derived from Eq. (5.37) in terms of K_2 as

$$K_1 = -\frac{A_{12}}{A_{11}} K_2 \tag{5.39}$$

$$K_3 = \frac{1}{A_{23}} (A_{21} \frac{A_{12}}{A_{11}} - A_{22}) K_2 \tag{5.40}$$

To obtain unique solution for these coefficients, orthonormality between mode shapes can be utilized. For the boundary conditions considered here, this condition is stated as:

$$\int_0^L m(x)[\Phi_i(x)\Phi_j(x) + \Lambda_i(x)\Lambda_j(x)]dx + m_e\Phi_i(L)\Phi_j(L) + m_e\Lambda_i(L)\Lambda_j(L) = \delta_{ij} \tag{5.41}$$

where δ_{ij} is the Kronecker delta.

5.4.1.2. Forced Motion Analysis of Coupled Transversal/Longitudinal Motion

Using expansion theorem for the beam vibration analysis, the expressions for the transverse and longitudinal displacements become:

$$z(x,t) = \sum_{i=1}^{\infty} \Phi_i(x) q_i(t) \tag{5.42}$$

$$G(x,t) = \sum_{i=1}^{\infty} \Lambda_i(x) q_i(t) \tag{5.43}$$

where $q_i(t)$ are the generalized time-dependent coordinates. Now, inserting Eqs. (5.42) and (5.43) into Eqs. (5.22-5.24) and after some manipulations, the discretized model for

the transversal vibration and base motion of microcantilever can be written, respectively, as

$$\mathrm{A}_i\ddot{d}(t)+\sum_{j=1}^{\infty}B_{ij}\ddot{q}_j(t)+\sum_{j=1}^{\infty}C_{ij}\dot{q}_j(t)+\sum_{j=1}^{\infty}D_{ij}q_j(t)=f_i(t)\quad ,i=1,2,\ldots,\infty \tag{5.44}$$

where

$$A_i=\int_0^L\rho\Phi_i(x)dx \qquad B_{ij}=\int_0^L\rho\Phi_i(x)\Phi_j(x)dx$$

$$C_{ij}=\int_0^L\Phi_i(x)[B\Phi_j(x)+C\Phi'_j(x)]dx+C_xH\Phi'_i(L-\varepsilon)[\Phi'_j(L)+\Lambda_j(L)]+C_z\Phi_i(L-\varepsilon)\Phi_j(L)$$

$$D_{ij}=EI_{yy}\int_0^L\Phi_i(x)\Phi''''_j(x)dx$$

$$f_i(t)=\int_0^L\Phi_i(x)\Pi_1(x,t)dx$$

and base motion can be expressed as

$$\Psi\ddot{d}(t)+\sum_{i=1}^{\infty}L_i\ddot{q}_i(t)=\Pi_2(x,t) \tag{5.45}$$

where

$$\Psi=(m+m_e+\rho L) \qquad L_i=\int_0^L\rho\Phi_i(x)dx+m_e\Phi_i(L)$$

The truncated *n*-mode description for Eqs. (5.44) and (5.45) can now be presented in the following matrix form:

$$\mathbf{M}\ddot{\mathbf{q}}+\mathbf{C}\dot{\mathbf{q}}+\mathbf{K}\mathbf{q}=\mathbf{F}\mathbf{u} \tag{5.46}$$

where

$$\mathbf{M}=\begin{bmatrix} \Psi & L_1 & L_2 & \cdots & L_n \\ A_1 & B_{11} & B_{12} & \cdots & B_{1n} \\ A_2 & B_{21} & B_{22} & \cdots & B_{2n} \\ \vdots & \vdots & \vdots & \ddots & \vdots \\ A_n & B_{n1} & B_{n2} & \cdots & B_{nn} \end{bmatrix} \qquad \mathbf{C}=\begin{bmatrix} 0 & 0 & 0 & \cdots & 0 \\ 0 & C_{11} & C_{12} & \cdots & C_{1n} \\ 0 & C_{21} & C_{22} & \cdots & C_{2n} \\ \vdots & \vdots & \vdots & \ddots & \vdots \\ 0 & C_{n1} & C_{n2} & \cdots & C_{nn} \end{bmatrix}$$

$$\mathbf{K}=\begin{bmatrix} 0 & 0 & 0 & \cdots & 0 \\ 0 & D_{11} & D_{12} & \cdots & D_{1n} \\ 0 & D_{21} & D_{22} & \cdots & D_{2n} \\ \vdots & \vdots & \vdots & \ddots & \vdots \\ 0 & D_{n1} & D_{n2} & \cdots & D_{nn} \end{bmatrix} \qquad \mathbf{q}=\begin{Bmatrix} d(t) \\ q_1(t) \\ q_2(t) \\ \vdots \\ q_n(t) \end{Bmatrix}$$

$$\mathbf{F}=\begin{bmatrix} 1 & 0 & 0 & F_4 \\ 0 & F_{11} & F_{21} & F_{31} \\ 0 & F_{12} & F_{22} & F_{32} \\ \vdots & \vdots & \vdots & \vdots \\ 0 & F_{1n} & F_{2n} & F_{3n} \end{bmatrix} \qquad \mathbf{u}=\begin{Bmatrix} f(t) \\ V(t) \\ \dot{V}(t) \\ \ddot{V}(t) \end{Bmatrix}$$

where

$$F_4=\frac{\mu_x}{k_x}\beta a[\int_0^L \rho F_1(x)dx+m_e F_1(L)]$$

$$\overline{F}_{1i}=\beta a[\frac{\mu_x}{k_x}EI_{yy}\int_0^L \Phi_i(x)F_1''''(x)dx+H\Phi_i'(L-\varepsilon)+\Phi_i(L-\varepsilon)]$$

$$\overline{F}_{2i}=\beta a\frac{\mu_x}{k_x}[B\int_0^L \Phi_i(x)F_1(x)dx+C\int_0^L \Phi_i(x)F_1'(x)dx+$$
$$C_x H\Phi_i'(L-\varepsilon)(F_2(L)+F_1'(L)-1)+C_z\Phi_i(L-\varepsilon)F_1(L)]$$

$$\overline{F}_{3i}=\beta a\frac{\mu_x}{k_x}\int_0^L \rho\Phi_j(x)F_1(x)dx \qquad i=1,2,\ldots,\ \infty$$

The Eq. (5.46) can now be written in the form of state-space as

$$\dot{\mathbf{X}} = \Xi\mathbf{X} + \Gamma\mathbf{u} \tag{5.47}$$

where

$$\Xi = \begin{bmatrix} \mathbf{0} & \mathbf{I} \\ \mathbf{-M^{-1}K} & \mathbf{-M^{-1}C} \end{bmatrix}_{2(k+1)\times 2(k+1)}, \ \Gamma = \begin{bmatrix} \mathbf{0} \\ \mathbf{M^{-1}F} \end{bmatrix}_{2(k+1)\times 1}, \ \mathbf{C} = \begin{bmatrix} \mathbf{0} \\ \mathbf{M^{-1}} \end{bmatrix}_{2(k+1)\times 1} \text{ and } \quad \mathbf{X} = \begin{Bmatrix} \mathbf{q} \\ \dot{\mathbf{q}} \end{Bmatrix}_{2(k+1)\times 1}$$

The longitudinal vibrating of system can also be expressed as

$$\sum_{j=1}^{\infty} P_{ij}\ddot{q}_j(t) + \sum_{j=1}^{\infty} R_{ij}\dot{q}_j(t) + \sum_{j=1}^{\infty} U_{ij}q_j(t) = Y_i(t) \ \ , i = 1,2,\ldots, \infty \tag{5.48}$$

$$P_{ij} = \int_0^L \rho\Lambda_i(x)\Lambda_j(x)dx \qquad R_{ij} = C_x\Lambda_i(L-\varepsilon)[\Lambda_j(L) + H\Phi'_j(L)]$$

$$U_{ij} = -EA\int_0^L \Lambda_i(x)\Lambda''_j(x)dx \qquad Y_i(t) = \int_0^L \Lambda_i(x)\Pi_3(x,t)dx$$

and the truncated *n*-mode description for Eqs. (5.48) is as follow;

$$\mathbf{M_L}\ddot{\mathbf{q}}_\mathbf{L} + \mathbf{C_L}\dot{\mathbf{q}}_\mathbf{L} + \mathbf{K_L}\mathbf{q_L} = \mathbf{F_L}\mathbf{u_L} \tag{5.49}$$

where

$$\mathbf{M_L} = \begin{bmatrix} P_{11} & P_{12} & \cdots & P_{1n} \\ P_{21} & P_{22} & \cdots & P_{2n} \\ \vdots & \vdots & \ddots & \vdots \\ P_{n1} & P_{n2} & \cdots & P_{nn} \end{bmatrix} \qquad \mathbf{C_L} = \begin{bmatrix} R_{11} & R_{12} & \cdots & R_{1n} \\ R_{21} & R_{22} & \cdots & R_{2n} \\ \vdots & \vdots & \ddots & \vdots \\ R_{n1} & R_{n2} & \cdots & R_{nn} \end{bmatrix}$$

$$\mathbf{K_L} = \begin{bmatrix} U_{11} & U_{12} & \cdots & U_{1n} \\ U_{21} & U_{22} & \cdots & U_{2n} \\ \vdots & \vdots & \ddots & \vdots \\ U_{n1} & U_{n2} & \cdots & U_{nn} \end{bmatrix} \qquad \mathbf{q_L} = \begin{Bmatrix} q_1(t) \\ q_2(t) \\ \vdots \\ q_n(t) \end{Bmatrix}$$

$$\mathbf{F_L} = \begin{bmatrix} F_{L-11} & F_{L-21} & F_{L-31} \\ \vdots & \vdots & \vdots \\ F_{L-1n} & F_{L-2n} & F_{L-3n} \end{bmatrix} \qquad \mathbf{u_L} = \begin{Bmatrix} V(t) \\ \dot{V}(t) \\ \ddot{V}(t) \end{Bmatrix}$$

where

$$F_{L-1i} = \beta a[\Phi_i(L-\varepsilon) - \frac{\mu_x}{k_x} EA \int_0^L \Phi_i(x) F_2''(x) dx]$$

$$F_{L-2i} = \beta a \frac{\mu_x}{k_x} C_x \Phi_i(L-\varepsilon)[F_2(L) + HF_1'(L) - 1]$$

$$F_{L-3i} = \beta a \frac{\mu_x}{k_x} \int_0^L \rho \Phi_i(x) F_2(x) dx$$

Finally, the Eq. (5.46) can be written in the form of state-space as

$$\dot{\mathbf{X}}_\mathbf{L} = \Xi_\mathbf{L} \mathbf{X}_\mathbf{L} + \Gamma_\mathbf{L} \mathbf{u}_\mathbf{L} \tag{5.50}$$

where

$$\Xi_\mathbf{L} = \begin{bmatrix} \mathbf{0} & \mathbf{I} \\ \mathbf{-M_L^{-1}K_L} & \mathbf{-M_L^{-1}C_L} \end{bmatrix}_{2(k+1)\times 2(k+1)}, \ \Gamma_\mathbf{L} = \begin{bmatrix} \mathbf{0} \\ \mathbf{M_L^{-1}F_L} \end{bmatrix}_{2(k+1)\times 1}, \ \mathbf{C_L} = \begin{bmatrix} \mathbf{0} \\ \mathbf{M_L^{-1}} \end{bmatrix}_{2(k+1)\times 1} \text{ and}$$

$$\mathbf{X_L} = \begin{Bmatrix} \mathbf{q_L} \\ \dot{\mathbf{q}}_\mathbf{L} \end{Bmatrix}_{2(k+1)\times 1}$$

$$\Xi_L = \begin{bmatrix} 0 & I \\ -M_L^{-1}K_L & -M_L^{-1}C_L \end{bmatrix}, \quad \Gamma = \begin{Bmatrix} 0 \\ M_L^{-1}F_L \end{Bmatrix}, \quad C = \begin{Bmatrix} 0 \\ M_L^{-1} \end{Bmatrix}, \text{ and } \quad X_L = \begin{Bmatrix} q_L \\ \dot{q}_L \end{Bmatrix}$$

5.4.2. Coupled lateral bending-torsion displacement:

Similar to pervious problem, torsion and lateral bending vibrations are also coupled though friction and piezoelectric forces. The coupling terms appear in the right hand side of Eqs. (5.9) and (5.10) as well as coupled terms in the BCs (5.13) and (5.16). Comparing the eigenvalue problems for lateral bending/torsion and transversal bending/longitudinal motions (Eqs. (5.50-5.53)) reveals that the nature of equations for lateral and transversal bending and that of longitudinal and torsion are similar. The differences are related to constant coefficients of corresponding PDEs. Applying the similar procedure explained in the preceding section, the mode shapes, frequency equation, orthogonality condition and state-space representation for the coupled lateral bending/torsion motion can be also obtained. For the sake of briefness and undue complication, we do not provide the details here.

$$\rho v_{tt}(x,t) + EI_{z-z} v_{xxxx}(x,t) + Bv_t(x,t) + Cv_{xt}(x,t) = 0 \tag{5.50}$$

$$\rho[\ddot{d}(t) + w_{tt}(x,t)] + EI_{y-y} w_{xxxx}(x,t) - Q(x,t) + Bw_t(x,t) + Cw_{xt}(x,t) = 0 \tag{5.51}$$

$$J\theta_{tt}(x,t) - C_T \theta_{xx}(x,t) = 0 \tag{5.52}$$

$$\rho u_{tt}(x,t) - EAu_{xx}(x,t) = 0 \tag{5.53}$$

5.5. Numerical Results and Discussions

Based on the modeling procedure described above, a numerical simulation procedure is adopted to study the variation of natural frequency, mode shape and time response of system with respect to viscoelastic and piezoelectric properties of materials. Table 5.1 indicates the parameter values used for the simulations.

Table 5.1. Physical parameters of the system.

Properties	*Symbol*	*Value*	*Unit*
Beam length	L	460	μm
Beam thickness	t	2	μm
Beam width	b	50	μm
Beam density	ρ	2330	kg/m^3
Beam elastic modulus	E	120	GPa
Beam moment of inertia	I	3.33×10^{-23}	m^4
Tip height	h	20×10^{-6}	m
Tip mass	m_e	3×10^{-10}	kg
Base mass	m	0.001	kg
Beam viscous damping	B	1×10^{-8}	kg/ms
Beam structural damping	C	1×10^{-8}	kg/s
Contact radius	a	50×10^{-6}	m
Piezoelectric coefficient of material	β	40	N/mV

For the simulation purpose, the equation of motion has been truncated into only three modes. The eigenvalue problem associated with the transversal/longitudinal motion of beam is utilized to determine natural frequencies of microcantilever. Tables 5.2-5.4 list the natural frequency of the beam for; PFM system with only vertical spring (V-PFM), with only longitudinal spring (L-PFM), and with combined vertical/longitudinal springs (VL-PFM), respectively. Results indicate that in V-PFM, with the increase in sample spring constant, the natural frequency of microcantilever increases for all three mode shapes (see Table 5.2). Similar trend is seen for the natural frequency of L-PFM (see Table 5.3). Results demonstrate that the variation of natural frequency with respect to the stiffness of spring show more smooth trend in V-PFM compared to L-PFM. In L-PFM, the increase in the natural frequency is very small for the smaller spring constants; however, for the spring constant higher than 100 (N/m) the natural frequency for all three modes shows significant increase. At this range, L-PFM displays higher natural

frequency when compared to V-PFM. Table 4.4 lists the natural frequency of the microcantilever for VL-PFM.

Figure 5.4*a* depicts the first transversal mode shape of microcantilever in the V-PFM system for different equivalent sample spring constants. It is seen that the mode shape of microcantilever is heavily dependent upon the elastic properties of sample. Due to presence of tip mass, the mode shape shows concave curvature for k_z=0 at the end of beam. As the spring constant increases in the vertical direction, the radius of curvature decreases accordingly. This implies that higher spring constant makes more restriction at the end of microcantilever. Therefore, the clamped-free condition of the beam is converted into clamped-pinned condition for stiffer samples. Figure 5.4*b* presents the mode shape of microcantilever beam in VL-PFM system. The presence of longitudinal spring significantly affects the shape of curvature at the entire length of beam compared to V-PFM. It is seen that at higher spring constants, the amplitude of vibration decreases significantly.

Figures 5.4*c*-*d* depict the mode shape of microcantilever for second natural frequency in V-PFM and VL-PFM, respectively. Results demonstrate that the amplitude of mode shape at the end of microcantilever increases for the smaller values of spring constants. However, for higher spring constants, as expected, the amplitude of vibration decreases significantly. The reason is that as the constraint force is applied at the free end of the beam, the first extremum point of mode shapes moves left side with the increase in the spring constants. This results in the upward shift in the mode shapes of the beam with change in the slope of curvature at the end of microcantilever. As the spring force

increases, the slope decreases accordingly. Finally, at some points spring force can overcome this shift which leads to decrease in the amplitude of vibration. Similar trend can be observed for the third mode shape of microcantilever (see Figure 5.4e-f).

Figures 5.5*a-b* depict the first longitudinal mode shape of microcantilever for L-PFM and VL-PFM, respectively. Results indicate that at higher spring constants the effect of coupling could have a significant impact on the longitudinal mode shape of microcantilever. However, with the increase in the natural frequency of the system, the importance of coupling effect on the longitudinal vibration of microcantilever decreases accordingly (see Figure 5.5c-d for the mode shape of microcantilever at third natural frequency of system).

Figure 5.6a shows modal frequency response plot of microcanilever tip displacements at k_x=k_z= 10 (N/m) at four different damping ratios in the transversal direction where the damping term in the longitudinal direction is not taken into account. As expected, with the increase of damping coefficient, the amplitude of vibration decreases such that for $C_z = 5\times10^{-6}$ (N.S/m) the effect of third resonant frequency is vanished. Along this line, the effect of longitudinal damping term on the vibration of microcantilever is shown in Figure 5.6b. It is seen that the modal frequency of microcantilever in the presence of longitudinal damping term shows similar trend as observed in the previous case. More especially, Figure 5.6b demonstrates that at k_x=k_z= 10 (N/m), the resonance frequency of discrete system (tip-sample junction) reaches the second resonance frequency of the microcantilever. For this reason, the damping term does not influence the vibration amplitude at this frequency. Finally, Figure 5.7 illustrates the effect of longitudinal

damping term on the modal frequency of microcantilever at two different spring constants. The amplitude of vibration at k_x=k_z= 20 (N/m) decrease for all three resonance frequencies, however at k_x=k_z= 35 (N/m) the resonance frequency of sample reaches the third resonance frequency of microcantilever.

In summary, it is shown that in vector-PFM, the effect of coupling terms such as spring and damping terms significantly affect the natural frequencies and mode shapes of microcantilever. It is also observed that depending on the viscoelastic properties of sample; the resonance frequency of sample can reach one of resonance frequency of microcantilever. This results in un-damped vibrating condition in the corresponding frequency.

5.6. Conclusions

For materials with arbitrary crystallographic orientations, the vibration of microcantilever used in the PFM system may experience combined motions in the vertical-longitudinal or/and lateral-torsinal directions. In this study, a comprehensive dynamic model was proposed for a vector PFM with combined motions. It was shown that PFM system can be represented as a set of PDEs which can be transferred into ODE forms using assumed mode method. The PFM system was also written in the state-state representation form. It was shown that neglecting the coupling terms can affect the dynamic response of the system, significantly. Moreover, effects of spring constant and damping coefficient of material in the vibration of microcantilever were studied in more details. Results demonstrated that materials with different mechanical properties can induce different constraints at the free end of microcantilever, and materials with higher

stiffness can change the clamped-free condition of cantilever into clamped-pinned condition.

Table 5.2. Natural frequencies of microcantilever for V-PFM system.

	k_z=0	k_z=1	k_z=3	k_z=5	k_z=10	k_z=100	k_z=1000	k_z=2000
ω1(106)	0.0687	0.1838	0.2459	0.2665	0.2838	0.3001	0.3017	0.3018
ω2(106)	0.4310	0.4777	0.5720	0.6483	0.7887	0.9575	0.9763	0.9773
ω3(106)	1.2069	1.2227	1.2574	1.2951	1.3958	1.9425	2.0323	2.0368

Table 5.3. Natural frequencies of microcantilever for L-PFM system.

	k_x=0	k_x=1	k_x=3	k_x=5	k_x=10	k_x=100	k_x=1000	k_x=2000
ω1(106)	0.0687	0.0697	0.0714	0.0730	0.0765	0.5183	0.5790	0.5848
ω2(106)	0.4310	0.4329	0.4364	0.4399	0.4478	1.3150	1.4311	1.4446
ω3(106)	1.2069	1.2087	1.2122	1.2156	1.2238	2.4878	2.6629	2.6867

Table 5.4. Natural frequencies of microcantilever for VL-PFM system where $k=k_x=k_z$.

	k=0	k=1	k=3	k=5	k=10	k=100	k=1000	k=2000
ω1(106)	0.0687	0.1838	0.2466	0.2685	0.2898	0.3539	0.4200	0.4218
ω2(106)	0.4310	0.4791	0.5741	0.6497	0.7686	1.0107	1.1569	1.1791
ω3(106)	1.2069	1.2227	1.2574	1.2951	1.3958	1.9425	2.0323	2.0368

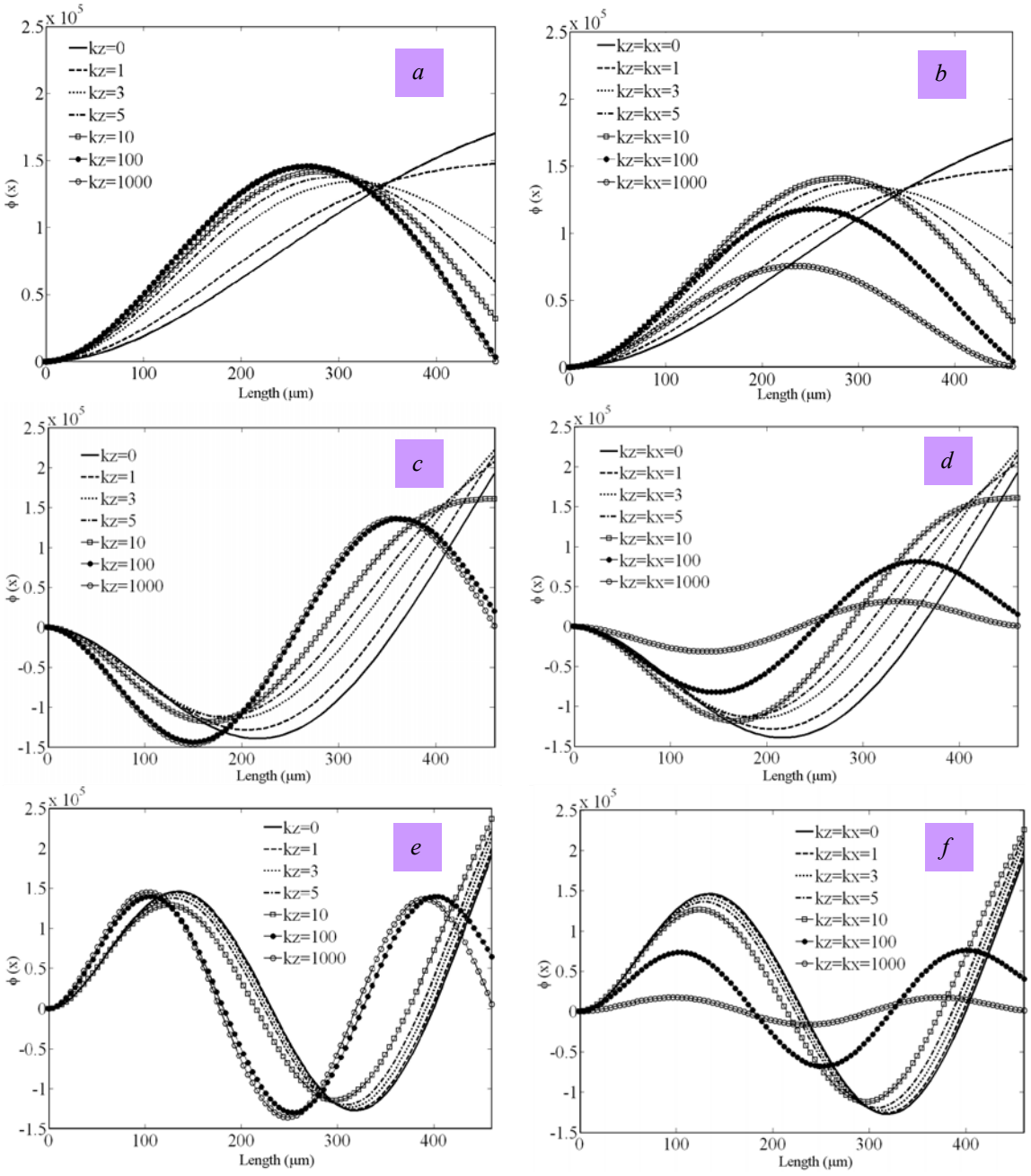

Figure 5.4. bending mode shapes of microcantilever for; (*a*) first mode of V-PFM, (*b*) first mode of VL-PFM, (*c*) second mode of V-PFM, (*d*) second mode of VL-PFM, (*e*) third mode of V-PFM, and (*f*) third mode of VL-PFM. The units of k_x and k_z are (N/m).

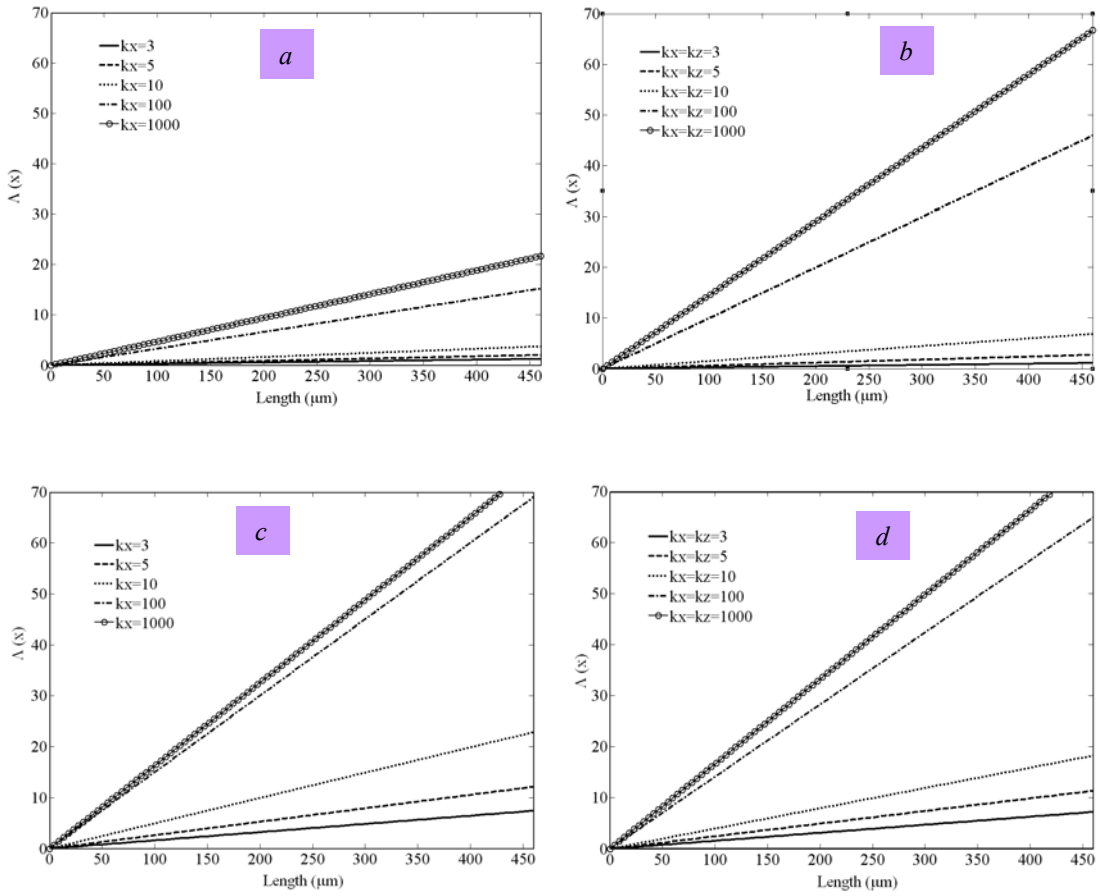

Figure 5.5. Longitudinal mode shapes of microcantilever for; (*a*) first mode of L-PFM, (*b*) first mode of VL-PFM, (*c*) third mode of L-PFM, and (*d*) third mode of VL-PFM. The units of k_x and k_z are (N/m).

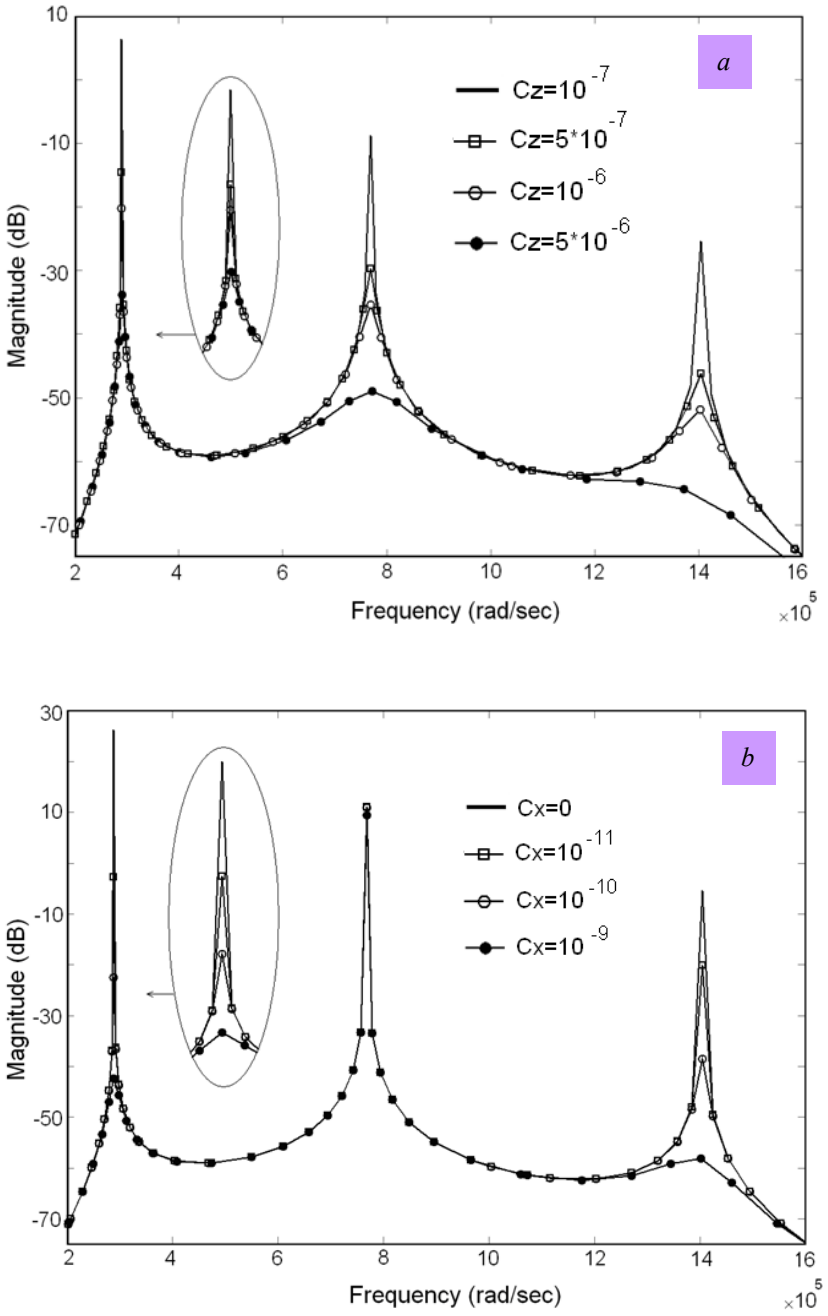

Figure 5.6. Modal frequency response plot of microcanilever tip displacements at $k_x = k_z = 10$ (N/m) and for four different damping ratios in, (*a*) transversal (without longitudinal term), and (*b*) longitudinal (without transversal term)directions. The units of damping coefficients are (N.S/m).

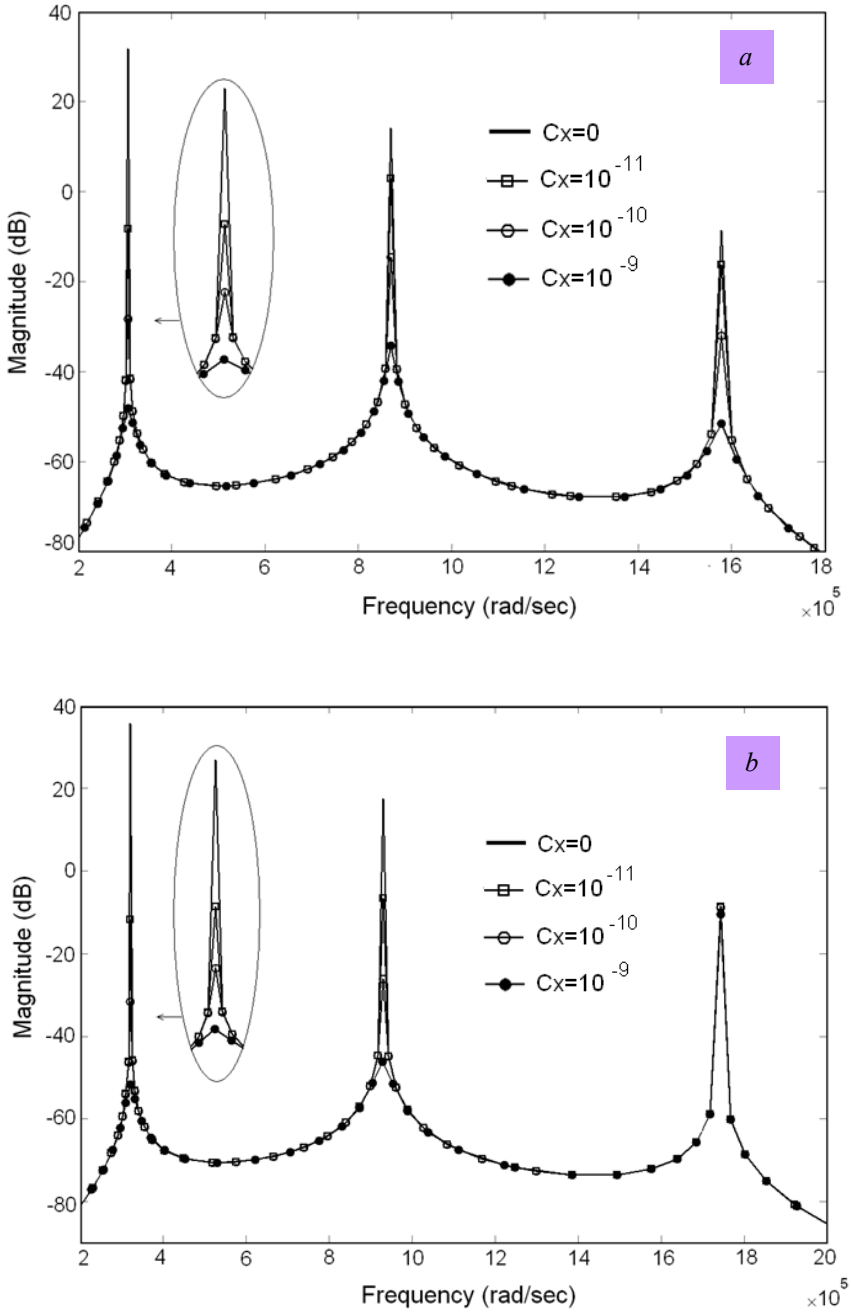

Figure 5.7. Modal frequency response plot of Microcanilever tip displacements for four damping ratios in longitudinal direction (without transversal term) and two spring constants, (*a*) k_x=k_z = 20, and (*b*) k_x=k_z=35. The units of damping coefficients are (N.S/m).

CHAPTER SIX

PIEZORESPONSE FORCE MICROSCOPY FOR LOW DIMENSIONAL MATERIAL CHARACTERIZATION; THEORY AND EXPERIMENT

6.1. Introduction

Piezoelectric materials are one of the most promising materials which have attracted a lot of attention since their discovery in 1880-1881. The applications of piezoelectric materials can be classified into four categories; generators, sensors, actuators, and transducers. The first commercial applications for piezoelectric materials as a sensor was introduced in World War I in the ultrasonic submarine structure [144]. Later, barium titanate oxide ($BaTiO_3$) ceramic was produced as a piezoelectric transducer material in the early 1950s [145]. In 1954, lead zirconate titanate ($PbZrTiO_3$–$PbTiO_3$) or PZT ceramics possessing excellent properties were developed as a promising candidate in all fields of piezoelectric applications [146]. Since, many works have been carried out in developing applications for PZT materials for implementation in microelectromechanical systems (MEMS) [51-53]. Such utilization results in high sensitivity and low electrical noise in sensing applications and high output force in the actuation of MEMS compared to other conventional designs.

Along this line and in order to implement piezoelectric materials in the nano- and microstructure design, the investigation of size effect of these materials in low dimensional structures is a crucial importance. It has been shown that as the dimension of piezoelectric materials are getting smaller, the materials cannot preserve their

macroscopic properties and a significant deviation in the material properties can be observed when compared to bulk materials [54]. In this respect, characterization of material in these scales requires different technique than those utilized for bulk materials.

Recently, rapid development in scanning probe microscopy (SPM)-based techniques and in particular piezoresponse force microscopy (PFM) has attracted widespread attention as a primary technique for nondestructive characterization of piezoelectric materials in the scale of grain [125-129]. The operational modes of PFM have been studied in the previous chapter and a comprehensive model for dynamic behavior of vector PFM system was introduced. In this chapter, we aim to introduce a practical procedure in order to simultaneously estimate the local viscoelastic and piezoelectric properties of materials. For this purpose, an energy based approach is used to derive the governing equations of motion for vertical PFM at a given point on the sample. A general formulation is obtained for the mode shape and frequency response of the system. Finally, using the method of assumed modes, the governing ordinary differential equations (ODEs) of the system and its state-space representation are derived under applied external voltage. For the proof of the concept, the results obtained from theory are used along with experimental data to identify the spring constant and piezoelectric coefficient of Periodically Poled Lithium Niobate (PPLN) material. In this regard, a parameter estimation technique based on minimizing the percentage of modeling error is utilized to obtain the optimal values of materials.

6.2. Distributed-Parameters Modeling of PFM

Based on the materials presented in the preceding chapter, a PFM system can be modeled as a microcantilever beam where one end of the beam is clamped to the base position assembly with the displacement of $d(t)$ and the total mass of m, and the free end of beam is attached to the tip mass of m_e (see Figure 6.1). As the external electric field is applied between the conducting tip and sample, the response of material can be divided into viscoelastic and piezoelectric parts. The viscoelstic part can be modeled based on Kelvin-Voigt model (parallel spring and damper), while the piezoresponse of material is considered as a force, F_{tip}, acting at the free end of microcantilever. Utilizing Hertzian contact mechanics at the tip-surface junction the indentation force can be expressed as [143]

$$P = \alpha \frac{a^3}{R} - \beta a V \tag{6.1}$$

where the first and second terms in the right hand side of Eq. (6.1) represent the elastic and piezoelectric components of applied force, respectively. In the above equation, α and β demonstrate the elastic and piezoelectric properties of material, respectively, R is the tip radius and a is the contact radius.

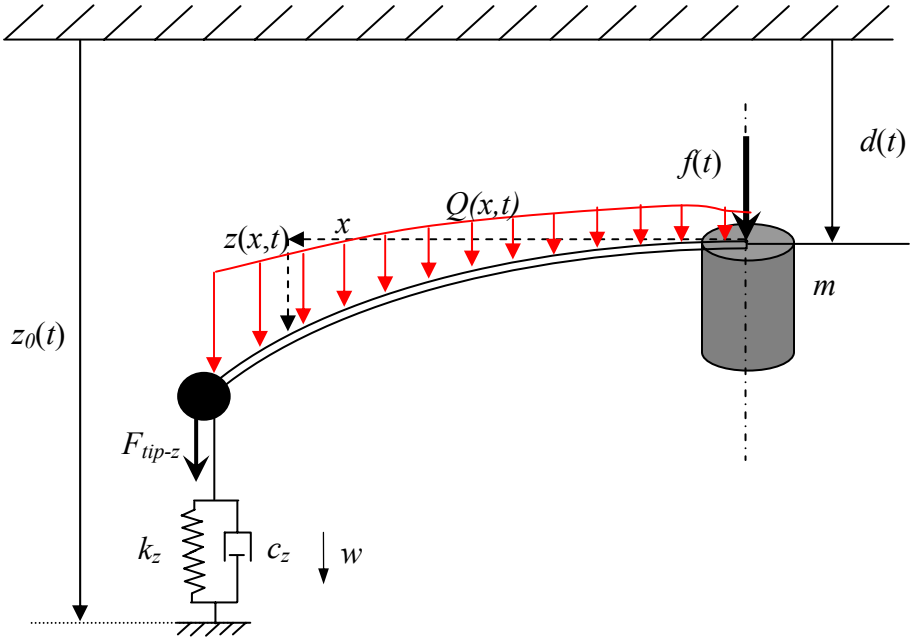

Figure 6.1. A schematic model of vertical PFM and sample.

Using the extended Hamilton's Principle and following the same procedure as outlined in preceding chapte, the partial differential equation (PDE) for the transversal vibration of microcantilever in the absence of base motion which is the case for a point scanning problem can be expressed as:

$$\rho w_{tt}(x,t) + EIw_{xxxx}(x,t) - Q(x,t) + Bw_t(x,t) + Cw_{xt}(x,t) = 0 \tag{6.2}$$

with following boundary conditions

$$m_e w_{tt}(L,t) - EIw_{xxx}(L,t) + k_z w(L,t) + C_z w_t(L,t) = F_{tip} \tag{6.3}$$

and

$$w(0,t) = w_x(0,t) = w_{xx}(L,t) = 0 \tag{6.4}$$

In the above equations, subscripts $(\cdot)_t$ and $(\cdot)_x$ indicate the partial derivatives with respect to the time variable t and position variable x, respectively. EI, ρ and L denote the

rigidity, linear density and length of microcantilever, respectively. $Q(x,t)$ is the capacitive forces between tip-cantilever assembly and surface, B is the viscous air damping, C is the structural damping term, k_z is the spring constant, and C_z is the damping coefficient of material.

6.3. Modal Analysis of System

In order to obtain natural frequencies and mode shapes of the system, the eigenvalue problem associated with the transversal vibration of microcantilever is obtained by applying free and un-damped conditions to Eq. (6.2) which results in

$$\rho w_{tt}(x,t) + EI_{yy} w_{xxxx}(x,t) = 0 \tag{6.5}$$

The solution to $w(x,t)$ can be assumed in the following separable form of

$$w(x,t) = \Phi(x) e^{i\omega t} \tag{6.6}$$

where $\Phi(x)$ is the mode shape of the microcantilever beam with a tip mass and ω is the natural frequency of the system. The solution for the mode shape of system can be expressed as

$$\Phi(x) = K_1[\sin(\lambda x) - \sinh(\lambda x)] + K_2[\cos(\lambda x) - \cosh(\lambda x)] \tag{6.7}$$

where K_1 and K_2 are coefficients of eigenfunctions. Inserting Eqs. (6.7) into free and un-damped condition in the BC. (6.3) results in following relationship:

$$\begin{bmatrix} A_{11} & A_{12} \\ A_{21} & A_{22} \end{bmatrix} \begin{bmatrix} K_1 \\ K_2 \end{bmatrix} = 0 \tag{6.8}$$

where

$$A_{11} = -EI_{yy}\lambda^3 \Phi_1'''(L) - (m_e\omega^2 - k_z)\Phi_1(L)$$
$$A_{12} = -EI_{yy}\lambda^3 \Phi_2'''(L) - (m_e\omega^2 - k_z)\Phi_2(L)$$
$$A_{21} = \lambda^2 \Phi_1''(L)$$
$$A_{22} = \lambda^2 \Phi_2''(L)$$

and

$$\Phi_1(L) = \Phi_2'''(L) = \sin\lambda L - \sinh\lambda L$$
$$\Phi_1'(L) = \Phi_2(L) = \cos\lambda L - \cosh\lambda L$$
$$\Phi_1''(L) = \Phi_2'(L) = -\sin\lambda L - \sinh\lambda L$$
$$\Phi_1'''(L) = \Phi_2''(L) = -\cos\lambda L - \cosh\lambda L$$

The frequency equation can now be obtained by equating the determinant of Eq. (6.8) to zero. In order to determine the unique solution for the coefficients of mode shapes, K_1 and K_2, orthogonality between mode shapes for the boundary conditions considered here can be expressed as:

$$\int_0^L \rho\Phi_i(x)\Phi_j(x)dx + m_e\Phi_i(L)\Phi_j(L) = \delta_{ij} \tag{6.9}$$

where δ_{ij} is the Kronecker delta. The obtained mode shapes are utilized in the forced vibration analysis of the system which is the focus of the study in the following section.

6.4. Forced Motion Analysis of Microcantilever

Using expansion theorem for the beam vibration analysis, the expression for the transverseal displacement can be written as:

$$w(x,t) = \sum_{i=1}^{\infty} \Phi_i(x)q_i(t) \tag{6.10}$$

where $\Phi_i(x)$ and $q_i(t)$ are the mode shapes and generalized time-dependent coordinates, respectively. Inserting Eq. (6.10) into Eq. (6.2), the PDE for the forced vibration of the microcantilever can be written as

$$\ddot{q}_i(t) + \sum_{j=1}^{\infty} C_{ij}\dot{q}_j(t) + \omega_i^2 q_i(t) = f_i V(t) \qquad i = 1, 2, \ldots, \infty \tag{6.11}$$

where

$$C_{ij} = \int_0^L \Phi_i(x)[B\Phi_i(x) + C\Phi'_j(x)]dx + C_z\Phi_i(L)\Phi_j(L)$$

and

$$f_i = \beta a \Phi_i(L)$$

In the derivation of Eq. (6.11), the following orthogonality conditions for the mode shapes were utilized

$$\int_0^L \rho\Phi_i(x)\Phi_j(x)dx + m_e\Phi_i(L)\Phi_j(L) = \delta_{ij} \tag{6.12-1}$$

$$\int_0^L EI\Phi_i''(x)\Phi_j''(x)dx + k_z\Phi_i(L)\Phi_j(L) = \omega_i^2\delta_{ij} \tag{6.12-2}$$

The truncated *n*-mode description of the beam Eq. (6.11) can now be presented in the following matrix form:

$$\mathbf{M}\ddot{\mathbf{q}} + \mathbf{C}\dot{\mathbf{q}} + \mathbf{K}\mathbf{q} = \mathbf{F}u \tag{6.13}$$

where

$$\mathbf{M} = I_{n\times n},\ \mathbf{C} = [c_{ij}]_{n\times n},\ \mathbf{K} = [\omega_i^2\delta_{ij}]_{n\times n},\ \mathbf{q} = [q^{(1)}(t), q^{(2)}(t), \ldots, q^{(n)}(t)]_{n\times 1}^T,$$

$$\mathbf{F} = [f^{(1)}, f^{(2)}, \ldots, f^{(n)}]_{n\times 1}^T,\ u = V(t)$$

The state-space representation of Eq. (6.13) is given by:

$$\dot{\mathbf{X}} = \mathbf{A}\mathbf{X} + \mathbf{B}u \tag{6.14}$$

where

$$\mathbf{A} = \begin{bmatrix} \mathbf{0} & \mathbf{I} \\ -\mathbf{M}^{-1}\mathbf{K} & -\mathbf{M}^{-1}\mathbf{C} \end{bmatrix}_{2n\times 2n}, \ \mathbf{B} = \begin{bmatrix} \mathbf{0} \\ \mathbf{M}^{-1}\mathbf{F} \end{bmatrix}_{2n\times 1}, \ \mathbf{X} = \begin{Bmatrix} \mathbf{q} \\ \dot{\mathbf{q}} \end{Bmatrix}_{2n\times 1} \tag{6.15}$$

6.5. Experimental Procedure and Setup

In this study, a commercial AFM (Asylum Research MFP-3D [www.asylumresearch.com], Figure 6.2) with an Au/Cr-coated SiN pyramidal tip on a triangular microcantilever (TR400PB, Olympus, length $L \approx 200$ μm, resonant frequency ~ 10 kHz, nominal spring constant k ~ 0.02 N m-1) were used for indentation of substrate. A more accurate spring constant 27.52 pN nm^{-1} was determined via a force-distance curve on the surface location where measurements were made. The force-distance curve were also resulted in determination of the deflection inverse optical lever sensitivity InvOLS = 63.47 nm V^{-1}, which allows for conversion of the deflection signal into displacement. Figure 6.3 demonstrates the geometry and 3D motion of the microcantilever at second, forth and sixth mode of vibration.

The sample was periodically poled lithium niobate (PPLN), made by Crystal Technologies, Inc. using the electric-field poling technique [147]. The 1 cm^2 PPLN chip (thickness ~ 1 mm) was mounted onto a 15 mm stainless steel specimen disc (Ted Pella) using a 9 mm, double-sided carbon conductive tab (PELCO Tabs, Ted Pella) (see Figure

6.4). The metal specimen disc had been attached to a standard glass microscope slide using a fast cure epoxy. The glass slide was held in place on the MFP-3D stage using magnets at each end of the slide. The PPLN was grounded to the MFP-3D stage via 30-gauge insulated wrapping wire (Radio Shack), which was attached to the top PPLN surface using PELCO conductive silver 187 (Ted Pella).

Figure 6.2. The Asylum Research MFP-3D.

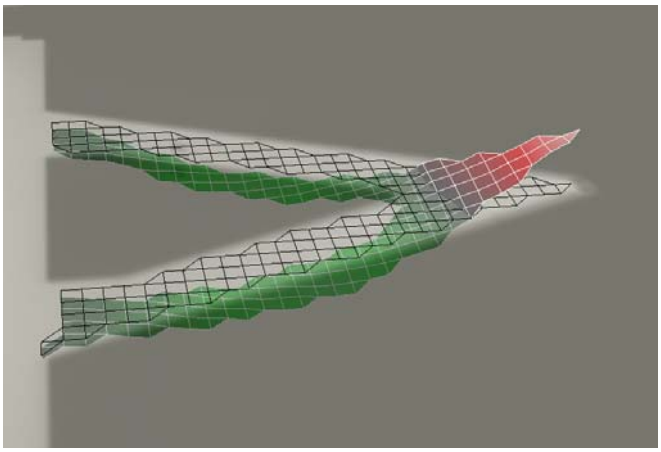

(a)

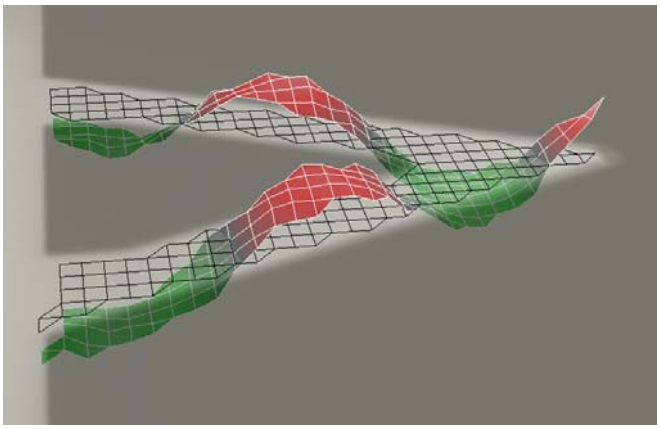

(b)

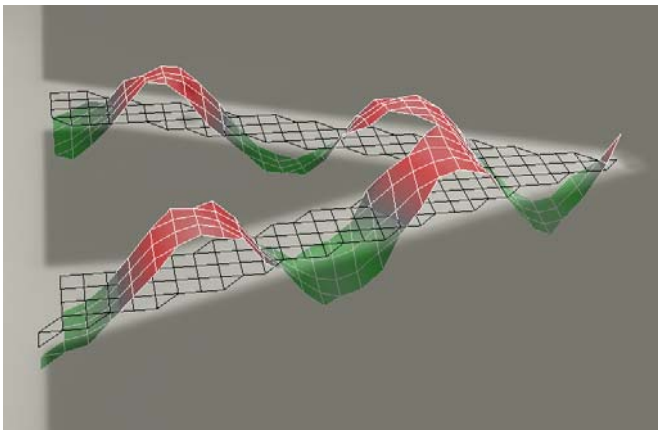

(c)

Figure 6.3. 3D motion of triangular microcantilever at (a) second mode, (b) forth mode, and (c) sixth mode.

Figure 6.5 depicts (a) the height, (b) PFM amplitude and (c) PFM phase images acquired simultaneously of PPLN. Some topographic cross-talk may be seen between the height and PFM amplitude images. This is caused by changes in the peak resonant frequencies as the features' properties change. The PFM phase image demonstrates c + (lighter) and c – (darker) poled domains. Moderate contributions from electrostatics are evidenced by the weak phase change between domains. The scan size is 40 μm x 40 μm, and the scan rate is 0.50 Hz. The images have been flattened on the first order. Z-scales are (a) 5.38 nm, (b) 318.89 pm, and (c) 109.52°. PFM images were obtained with 10 V applied to the tip at 1.209 MHz.

PFM imaging of a 40 μm x 40 μm area of the PPLN sample revealed a poling spacing of 15.8±0.2 μm (see phase image in Figure 6.6). The tip was positioned on a c – domain that was also at a spot with clean, flat topography using the force panel in contact mode (see Figure 6.5, marker #1). At this location, the force-distance curve was performed to determine the InvOLS and spring constant, and once contact was re-established with the Z-piezo approximately unstrained, surface contact tunes were made in piezo force mode. The frequency of the voltage applied to the tip was swept from 0 Hz to 1 MHz. Maintaining the same tip position, 10 ms step voltage with magnitude of 3 volt were applied to the PPLN while the deflection response over time was recorded.

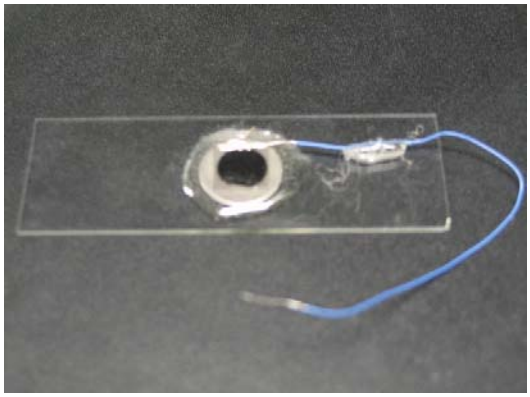

Figure 6.4. The PPLN chip on the MFP-3D stage.

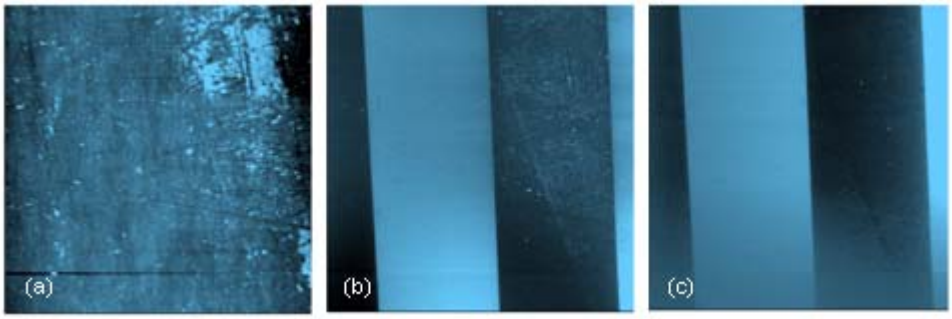

Figure 6.5. Height (a), PFM amplitude (b) and PFM phase (c) images of PPLN.

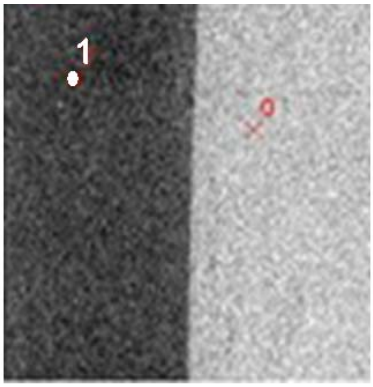

Figure 6.6. PFM phase image of PPLN showing the location of the tip at marker #1.

6.6. Material Characterization

In order to detect the properties of PPLN based on the results obtain from theory and experiment, a system identification procedure is required to characterize the whole system parameters. The similar procedure explained in Section 3.4 was carried out here for this purpose. To separate the vertical modes from other modes such as torsion, the random optimization algorithm is designated based on minimum modeling error for all possible combinations of resonant frequencies (see Figure 6.7). This algorithm has been applied for a series of optimization runs in order to arrive at a global extremum.

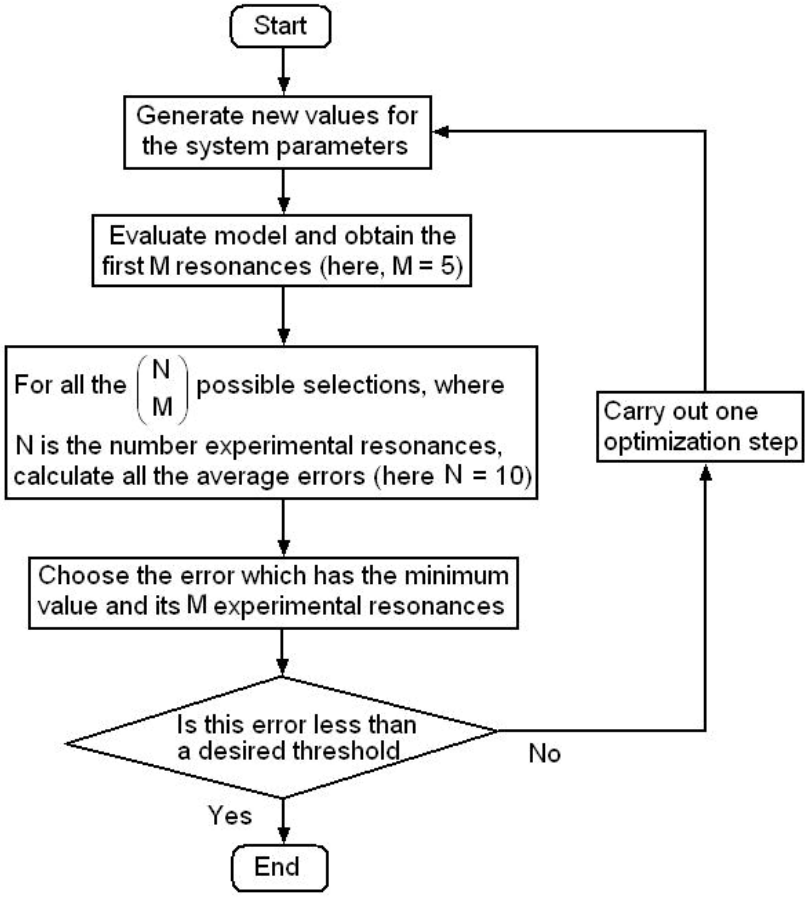

Figure 6.7. Optimization algorithm in order to separate bending modes from non-vertical modes.

Figure 6.8 depicts the first 7 actual resonant frequencies with first 5 vertical frequencies obtained from theoretical model. Based on the proposed algorithm, it is shown that two actual modes of the system do not match the vertical modes. Extensive numerical simulations have been performed which show the validity of this optimization process in eliminating these two modes. In this respect, the optimal values for the beam and spring constant have been obtained as listed in Table 6.1.

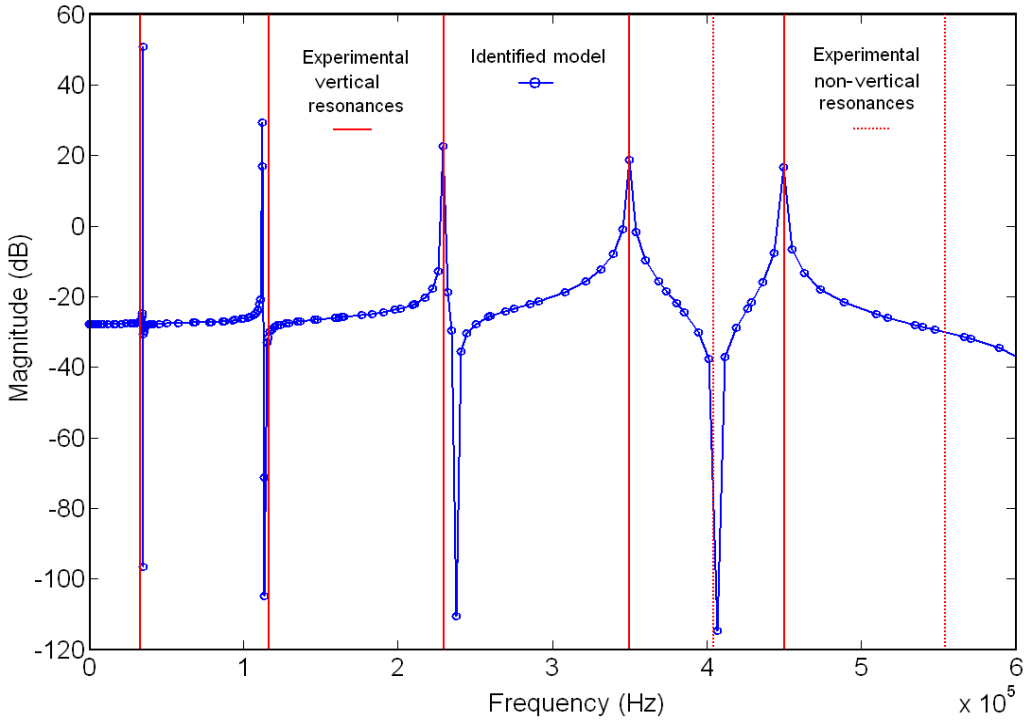

Figure 6.8. Comparison of actual and theoretical resonant frequencies for PPLN.

Table 6.1. Optimal physical parameters of the system.

Properties	*Symbol*	*Value*	*Unit*
Beam length	L	175	μm
Beam density	ρ	3900	kg/m^3
Beam rigidity	EI	5.8×10^{-14}	N/m^2
Tip mass	m_s	6.42×10^{-12}	kg
Spring constant	K_c	48.3	N/m

In order to obtain the piezoelectric coefficient of PPLN, a unit step input voltage with duration of 3 milliseconds was applied to the sample. The response of PPLN is demonstrated in Fig. 6.9. Since the equivalent spring constant in the tip-sample junction can be considered as a parallel combination of cantilever and material springs, the piezoelectric coefficient (β) for the applied piezoelectric force (βaV) at tip-sample junction can be expressed as:

$$\beta = (K_b + K_m)\frac{h}{aV}$$

where $K_b = 3EI/L^3$, K_m is the local spring constant of material obtained from frequency response, h is the steady state response of material to input voltage, a is the contact radius, and V is applied input voltage. Using the optimal parameters of beam and local spring constant of PPLN from Table 6.1, and assuming the contact radius of tip and sample equal with 50 nm, the piezoelectric coefficient of the PPLN can be obtained as $\beta = 55$ (N/m.V). The results obtained for piezoelectric coefficient and piezoelectric response of PPLN based on the proposed framework are comparable with those obtained for $BaTio_3$, PZT4 and PZT5a reported in reference [143].

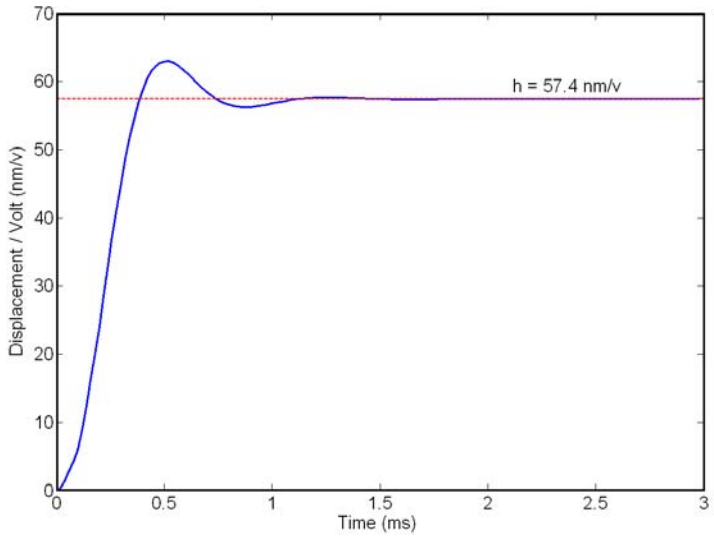

Figure 6.9. Response of PPLN to the unit step input voltage at marker #1dipected in Figure 6.6.

6.7. Conclusion

In this chapter, a new procedure was introduced to simultaneously detect the elastic and piezoelectric properties of materials. For this purpose, the whole PFM setup including microcantilever, sample and applied electrical field were modeled using an energy based approach. Using the method of assumed modes, the governing ordinary differential equations (ODEs) of the system and its state-space representation were derived under applied external voltage. Utilizing frequency response from experiment and theory, the spring constant of the PPLN was obtained through minimizing the percentage of modeling errors. Moreover, the step input response from experiment and theory are used to estimate the piezoelectric and damping coefficients of PPLN.

CHAPTER SEVEN

CONCLUSIONS AND FUTURE WORKS

A general and comprehensive framework was introduced for the forced vibration of flexible Euller Bernoulli beams with multiple jump discontinuities in their cross-section. A general formulation was derived for the characteristics matrix of beam using both boundary and continuity conditions. The governing ordinary differential equations (ODEs) of beam and their state-space representation were derived under distributed vertical loading condition. It was both analytically and experimentally shown that the presence of abrupt change in the cross-section of the beam can be significantly affected the natural frequencies and mode shapes of the beam. This approach was extended to vibration analysis of microcantilever Active Probes® fabricated with intentional geometrical discontinuities. Results obtained from experiment were compared with the commonly used uniform beam model as well as the proposed discontinuous beam model. It was shown that a significant enhancement on sensing accuracy of microcantilever Active Probes® can be achieved using the proposed discontinuous beam model compared to a uniform model when a multiple-mode operation is desired.

In the second part of this dissertation, a comprehensive model was proposed for vector PFM system under applied electrical loading. It was demonstrated that the PFM system can be governed by a set of partial differential equations (PDE) along with non-homogeneous and coupled boundary conditions. Using the method of assumed modes, the governing ordinary differential equations (ODEs) of the system and its state-space representation were derived under applied external voltage. The formulation was then

reduced to vertical PFM in order to detect the viscoelestic and piezoelectric properties of PPLN. For this purpose, the experimental and theoretical frequency responses along with minimizing the percentage of modeling error were utilized to obtain the optimal spring constant of PPLN. Finally, the step input response from experiment and theory were used to estimate the piezoelectric and damping coefficients of PPLN.

As future work, our developed model for PFM system can be utilized for data storage purpose in ferroelectric materials. In this regard, the information can be transferred to materials through external voltage which induces local dislocation in the materials. Utilizing the propsed modeling framework based on mechanical properties of materials before and after coding can be a new and novel strategy in order to decode data. Moreover, due to high sensitivity of microcantilever Active Probes®, our proposed dynamic modeling framework can be used to detect and characterize the growth rate of many biological species especially cancer cells. This model can also allow employment of this theory in AFM systems to replace laser-based detection mechanism with other alternative transductions.

APPENDIX

Sample Maple and Matlab Codes for Numerical Simulations

For numerical simulation and analysis of MCS, Maple and Matlab codes are utilized. A sample Maple code which is used in numerical analysis of vector PFM (presented in chapter 5) as well as a sample Matlab code which is utilized in dynamic response analysis of discontinuous EB beam (presented in chapter 3) have been attached in the next pages of this dissertation.

Maple Code for Coupled Longitudinal-Vertical Vibration of Microcantilever

```
> restart;
> eq_v := rho·diff(zz(x,t),t,t) + E·II·diff(zz(x,t),x,x,x,x) = 0;
> eq1 := diff(si(x),x,x,x,x) − λ^4·si(x) = 0;
>
> phi := x→K1·(sin(lambda·x) − sinh(lambda·x)) + K2·(cos(lambda
      ·x) − cosh(lambda·x))
> Lambda := x→K3·sin(λ^2·sqrt(II/A)·x)
> φ1 := x→diff(phi(x),x)
> φ2 := x→diff(phi(x),x,x)
> φ3 := x→diff(φ2(x),x)
> Λ1 := x→diff(Lambda(x),x)
> Λ2 := x→diff(Lambda(x),x,x)
> z := (x,t)→phi(x)·exp(I·omega·t)
> z1 := (x,t)→diff(z(x,t),x)
> z2 := (x,t)→diff(z(x,t),x,x)
> z3 := (x,t)→diff(z(x,t),x,x,x)
> G := (x,t)→Lambda(x)·exp(I·omega·t)
> G1 := (x,t)→diff(G(x,t),x)
> G2 := (x,t)→diff(G(x,t),x,x)
> bc1 := me·diff(z(L,t),t,t) − E·II·z3(L,t) + kz·z(L,t) + Cz
      ·diff(z(L,t),t);
> bc2 := me·diff(G(L,t),t,t) + E·A·G1(L,t) + kx·(G(L,t)
      + z1(L,t)·H) + Cx·(diff(G(L,t),t) + diff(z1(L,t),t)·H);
> bc3 := 1/H·E·II·z2(L,t) + kx·(G(L,t) + z1(L,t)·H) + Cx
      ·(diff(G(L,t),t) + diff(z1(L,t),t)·H);
> Cz := 0; Cx := 10^-10;
> A11 := eval(bc1,[K1=1,K2=0,K3=0,Cz=0])
> A12 := eval(bc1,[K1=0,K2=1,K3=0,Cz=0])
> A13 := eval(bc1,[K1=0,K2=0,K3=1,Cz=0])
> A21 := eval(bc2,[K1=1,K2=0,K3=0,Cx=0])
> A22 := eval(bc2,[K1=0,K2=1,K3=0,Cx=0])
> A23 := eval(bc2,[K1=0,K2=0,K3=1,Cx=0])
> A31 := eval(bc3,[K1=1,K2=0,K3=0,Cx=0])
> A32 := eval(bc3,[K1=0,K2=1,K3=0,Cx=0])
> A33 := eval(bc3,[K1=0,K2=0,K3=1,Cx=0])
> with(LinearAlgebra):
> V := Matrix([[A11,A12,A13],[A21,A22,A23],[A31,A32,A33]]);
> detv := Determinant(V,method=multivar);
```

```
> lambda := ( rho·ω^2 / (E·II) )^0.25 ;
> L := 460·10^-6; H := 20·10^-6; t := 0; b := 50·10^-6; tb := 2·10^-6; II
      := 1/12·b·tb^3; E := 120·10^9; rho := 2330·b·tb; me
      := evalf( 1/3·(50·10^-6)^2·H·Pi ); A := b·tb;
> kx := 3.2; kz := 3.2;
> eq := simplify(detv)
> with(RootFinding);
> omeg := Analytic( eq, omega, re = 100..5000000, im = -0.001
      ..0.001);
> omeg := sort([omeg], `<`);
> freq := evalf( omeg[1] / (2·Pi) )>


for i from 1 by 1 to 3 do
  ph := x→eval(phi(x), omega = omeg[i]);
 Lm := x→eval(Lambda(x), omega = omeg[i]);
oo := int(rho·(ph(x)^2), x = 0..L);
 ooo := rho·int(Lm(x)^2, x = 0..L);
 o := simplify(evalf(oo + ooo + me·ph(L)^2 + me·Lm(L)^2));
 ort := o = 1;
 ort1 := K1 = -eval( A12/A11, omega = omeg[i] )·K2;
 ort2 := K3 = evalf( -eval( 1/A23·(A21·K1 + A22·K2), omega
      = omeg[i] ) );
Kset := solve({ort, ort1, ort2}, [K1, K2, K3]);
assign( Kset );
 a[i] := K1; b[i] := K2; c[i] := K3;
 phim := (x, i)→eval(phi(x), [K1 = a[i], K2 = b[i], omega
      = omeg[i]]);
 Lambdam := (x, i)→eval(Lambda(x), [K3 = c[i], omega
      = omeg[i]]);
 unassign('K1');
 unassign('K2');
 unassign('K3');
end do:


> unassign('t')
```

```
> evalf(me·phim(L,1)·phim(L,2) + me·Lambdam(L,1)
      ·Lambdam(L,2) + int(rho·(phim(x,1)phim(x,2)),x=0..L)
      + rho·int(Lambdam(x,1)·Lambdam(x,2),x=0..L))

> phim(x,3)
> phim(x,2)
> phim(x,1)
> Lambdam(x,1)
> Lambdam(x,2)
> Lambdam(x,3)
> phim1 := x→diff(phim(x,1),x)
> phim1(L,1) := eval(phim1(x,1),x=L)
> phim2 := x→diff(phim(x,2),x)
> phim2(L,2) := eval(phim2(x,2),x=L)
> phim3 := x→diff(phim(x,3),x)
> phim3(L,3) := eval(phim3(x,3),x=L)
> Lambdam1 := x→diff(Lambdam(x,1),x)
> Lambdam1(L,1) := evalf(eval(Lambdam1(x,1),x=L))
> Lambam2 := x→diff(Lambdam(x,2),x)
> Lambdam2(L,2) := evalf(eval(Lambdam(x,2),x=L))
> Lambdam3 := x→diff(Lambdam(x,3),x)
> Lambdam3(L,3) := evalf(eval(Lambdam3(x,3),x=L))
> m := 0.001; B := 10^-8; C := 10^-8; mu := 0.01; R := 50·10^-6; Bet
      := 40000; ff := t→0;#v:=t→2·sin(100000·t);

> F1 := x→-(kx·H·(x^5 - 7/2·L·x^4 + 4·L^2·x^3 + 3/2 L^3·x^2))/(E·II·L^3);

>

> F3 := x→(kx·(x^2 - L·x))/(E·A·L);

> Ftip := t→-Bet·R·v(t); Myy := t→Ftip(t)·H; Ufric := t
      →(mu·Ftip(t))/kx;

> eq1 := (m + me + rho·L)·diff(d(t),t,t) + rho·int(phim(x,1)
      ·diff(q1(t),t,t) + phim(x,2)·diff(q2(t),t,t) + phim(x,3)
      ·diff(q3(t),t,t),x=0..L) + me·(phim(L,1)·diff(q1(t),t,t)
      + phim(L,2)·diff(q2(t),t,t) + phim(L,3)·diff(q3(t),t,t))
```

```
> eq2 := rho·diff(d(t),t,t) + rho·(diff(q1(t),t,t)·phim(x,1)
      + diff(q2(t),t,t)·phim(x,2) + diff(q3(t),t,t)·phim(x,3))
      + E·II·(diff(phim(x,1),x,x,x,x)·q1(t) + diff(phim(x,2),x,
      x,x,x)·q2(t) + diff(phim(x,3),x,x,x,x)·q3(t)) + B
      ·(diff(q1(t),t)·phim(x,1) + diff(q2(t),t)·phim(x,2)
      + diff(q3(t),t)·phim(x,3)) + C·(diff(q1(t),t)·diff(phim(x,
      1),x) + diff(q2(t),t)·diff(phim(x,2),x) + diff(q3(t),t)
      ·diff(phim(x,3),x));

> eq3 := rho·(Lambdam(x,1)·diff(T1(t),t,t) + Lambdam(x,2)
      ·diff(T2(t),t,t) + Lambdam(x,3)·diff(T3(t),t,t)) − E·A
      ·(diff(Lambdam(x,1),x,x)·T1(t) + diff(Lambdam(x,2),x,x)
      ·T2(t) + diff(Lambdam(x,3),x,x)·T3(t));

> eq21 := int(eq2·phim(x,1), x = 0..L)

> eq22 := int(eq2·phim(x,2), x = 0..L)

> eq23 := int(eq2·phim(x,3), x = 0..L)

> M11 := eval(eq1, [diff(d(t),t,t) = 1, q1(t) = 0, q2(t) = 0, q3(t)
      = 0])

> M12 := eval(eq1, [diff(d(t),t,t) = 0, q2(t) = 0, q3(t) = 0,
      diff(q1(t),t,t) = 1])

> M13 := eval(eq1, [diff(d(t),t,t) = 0, q1(t) = 0, q3(t) = 0,
      diff(q2(t),t,t) = 1])

> M14 := eval(eq1, [diff(d(t),t,t) = 0, q1(t) = 0, q2(t) = 0,
      diff(q3(t),t,t) = 1])

> M21 := eval(eq21, [diff(d(t),t,t) = 1, q1(t) = 0, q2(t) = 0, q3(t)
      = 0])

> M22 := evalf(eval(eq21, [diff(d(t),t,t) = 0, q1(t) = 0, q2(t) = 0,
      q3(t) = 0, diff(q1(t),t,t) = 1]))

> M23 := evalf(eval(eq21, [diff(d(t),t,t) = 0, q1(t) = 0, q2(t) = 0,
      q3(t) = 0, diff(q2(t),t,t) = 1]))

> M24 := evalf(eval(eq21, [diff(d(t),t,t) = 0, q1(t) = 0, q2(t) = 0,
      q3(t) = 0, diff(q3(t),t,t) = 1]))

> M31 := eval(eq22, [diff(d(t),t,t) = 1, q1(t) = 0, q2(t) = 0, q3(t)
      = 0])

> M32 := evalf(eval(eq22, [diff(d(t),t,t) = 0, q1(t) = 0, q2(t) = 0,
      q3(t) = 0, diff(q1(t),t,t) = 1]))

> M33 := evalf(eval(eq22, [diff(d(t),t,t) = 0, q1(t) = 0, q2(t) = 0,
      q3(t) = 0, diff(q2(t),t,t) = 1]))

> M34 := evalf(eval(eq22, [diff(d(t),t,t) = 0, q1(t) = 0, q2(t) = 0,
      q3(t) = 0, diff(q3(t),t,t) = 1]))
```

```
> M41 := eval(eq23, [diff(d(t), t, t) = 1, q1(t) = 0, q2(t) = 0, q3(t)
      = 0])

> M42 := evalf(eval(eq23, [diff(d(t), t, t) = 0, q1(t) = 0, q2(t) = 0,
      q3(t) = 0, diff(q1(t), t, t) = 1]))

> M43 := evalf(eval(eq23, [diff(d(t), t, t) = 0, q1(t) = 0, q2(t) = 0,
      q3(t) = 0, diff(q2(t), t, t) = 1]))

> M44 := evalf(eval(eq23, [diff(d(t), t, t) = 0, q1(t) = 0, q2(t) = 0,
      q3(t) = 0, diff(q3(t), t, t) = 1]))

> MM := Matrix([[M11, M12, M13, M14], [M21, M22, M23, M24],
      [M31, M32, M33, M34], [M41, M42, M43, M44]]);

> C11 := eval(eq1, [diff(d(t), t) = 1, q1(t) = 0, q2(t) = 0, q3(t) = 0 ])

> C12 := eval(eq1, [diff(d(t), t, t) = 0, q1(t) = 0, q2(t) = 0, q3(t) = 0,
      diff(q1(t), t) = 1])

> C13 := eval(eq1, [diff(d(t), t, t) = 0, q1(t) = 0, q2(t) = 0, q3(t) = 0,
      diff(q2(t), t) = 1])

> C14 := eval(eq1, [diff(d(t), t, t) = 0, q1(t) = 0, q2(t) = 0, q3(t) = 0,
      diff(q3(t), t) = 1])

> C21 := eval(eq21, [diff(d(t), t) = 1, q1(t) = 0, q2(t) = 0, q3(t)
      = 0])

> C22 := evalf(eval(eq21, [diff(d(t), t, t) = 0, q1(t) = 0, q2(t) = 0,
      q3(t) = 0, diff(q1(t), t) = 1])) + evalf(Cx·H·phim1(L, 1)
      ·(Lambdam(L, 1) + phim1(L, 1))) + evalf(Cz·phim(L, 1)
      ·phim(L, 1))

> C23 := evalf(eval(eq21, [diff(d(t), t, t) = 0, q1(t) = 0, q2(t) = 0,
      q3(t) = 0, diff(q2(t), t) = 1])) + evalf(Cx·H·phim1(L, 1)
      ·(Lambdam(L, 2) + phim2(L, 2))) + evalf(Cz·phim(L, 1)
      ·phim(L, 2))

> C24 := evalf(eval(eq21, [diff(d(t), t, t) = 0, q1(t) = 0, q2(t) = 0,
      q3(t) = 0, diff(q3(t), t) = 1])) + evalf(Cx·H·phim1(L, 1)
      ·(Lambdam(L, 3) + phim3(L, 3))) + evalf(Cz·phim(L, 1)
      ·phim(L, 3))

> C31 := eval(eq22, [diff(d(t), t) = 1, q1(t) = 0, q2(t) = 0, q3(t)
      = 0])

> C32 := evalf(eval(eq22, [diff(d(t), t, t) = 0, q1(t) = 0, q2(t) = 0,
      q3(t) = 0, diff(q1(t), t) = 1])) + evalf(Cx·H·phim2(L, 2)
      ·(Lambdam(L, 1) + phim1(L, 1))) + evalf(Cz·phim(L, 2)
      ·phim(L, 1))
```

```
> C33 := evalf(eval(eq22, [diff(d(t), t, t) = 0, q1(t) = 0, q2(t) = 0,
      q3(t) = 0, diff(q2(t), t) = 1])) + evalf(Cx·H·phim2(L, 2)
      ·(Lambdam(L, 2) + phim2(L, 2))) + evalf(Cz·phim(L, 2)
      ·phim(L, 2))

> C34 := evalf(eval(eq22, [diff(d(t), t, t) = 0, q1(t) = 0, q2(t) = 0,
      q3(t) = 0, diff(q3(t), t) = 1])) + evalf(Cx·H·phim2(L, 2)
      ·(Lambdam(L, 2) + phim2(L, 2))) + evalf(Cz·phim(L, 2)
      ·phim(L, 3))

> C41 := eval(eq23, [diff(d(t), t) = 1, q1(t) = 0, q2(t) = 0, q3(t)
      = 0])

> C42 := evalf(eval(eq23, [diff(d(t), t, t) = 0, q1(t) = 0, q2(t) = 0,
      q3(t) = 0, diff(q1(t), t) = 1])) + evalf(Cx·H·phim3(L, 3)
      ·(Lambdam(L, 1) + phim1(L, 1))) + evalf(Cz·phim(L, 3)
      ·phim(L, 1))

> C43 := evalf(eval(eq23, [diff(d(t), t, t) = 0, q1(t) = 0, q2(t) = 0,
      q3(t) = 0, diff(q2(t), t) = 1])) + evalf(Cx·H·phim3(L, 3)
      ·(Lambdam(L, 2) + phim2(L, 2))) + evalf(Cz·phim(L, 3)
      ·phim(L, 2))

> C44 := evalf(eval(eq23, [diff(d(t), t, t) = 0, q1(t) = 0, q2(t) = 0,
      q3(t) = 0, diff(q3(t), t) = 1])) + evalf(Cx·H·phim3(L, 3)
      ·(Lambdam(L, 3) + phim3(L, 3))) + evalf(Cz·phim(L, 3)
      ·phim(L, 3))

> CC := Matrix([[C11, C12, C13, C14], [C21, C22, C23, C24],
      [C31, C32, C33, C34], [C41, C42, C43, C44]]);

> K11 := eval(eq1, [d(t) = 1, q1(t) = 0, q2(t) = 0, q3(t) = 0])
> K12 := eval(eq1, [d(t) = 0, q2(t) = 0, q3(t) = 0, q1(t) = 1])
> K13 := eval(eq1, [d(t) = 0, q1(t) = 0, q3(t) = 0, q2(t) = 1])
> K14 := eval(eq1, [d(t) = 0, q1(t) = 0, q2(t) = 0, q3(t) = 1])
> K21 := eval(eq21, [d(t) = 1, q1(t) = 0, q2(t) = 0, q3(t) = 0])
> K22 := evalf(eval(eq21, [d(t) = 0, q2(t) = 0, q3(t) = 0, q1(t) = 1]))
> K23 := evalf(eval(eq21, [d(t) = 0, q1(t) = 0, q3(t) = 0, q2(t) = 1]))
> K24 := evalf(eval(eq21, [d(t) = 0, q1(t) = 0, q2(t) = 0, q3(t) = 1]))
> K31 := eval(eq22, [d(t) = 1, q1(t) = 0, q2(t) = 0, q3(t) = 0])
> K32 := evalf(eval(eq22, [d(t) = 0, q2(t) = 0, q3(t) = 0, q1(t) = 1]))
> K33 := evalf(eval(eq22, [d(t) = 0, q1(t) = 0, q3(t) = 0, q2(t) = 1]))
> K34 := evalf(eval(eq22, [d(t) = 0, q1(t) = 0, q2(t) = 0, q3(t) = 1]))
> K41 := eval(eq23, [d(t) = 1, q1(t) = 0, q2(t) = 0, q3(t) = 0])
> K42 := evalf(eval(eq23, [d(t) = 0, q2(t) = 0, q3(t) = 0, q1(t) = 1]))
> K43 := evalf(eval(eq23, [d(t) = 0, q1(t) = 0, q3(t) = 0, q2(t) = 1]))
> K44 := evalf(eval(eq23, [d(t) = 0, q1(t) = 0, q2(t) = 0, q3(t) = 1]))
> KK := Matrix([[K11, K12, K13, K14], [K21, K22, K23, K24], [K31,
      K32, K33, K34], [K41, K42, K43, K44]]);
```

```
> Y1 := (x, t) → rho·diff(Ufric(t), t, t)·F1(x) + E·II·Ufric(t)
      ·diff(F1(x), x, x, x, x) + B·diff(Ufric(t), t)·F1(x) + C
      ·diff(F1(x), x)·diff(Ufric(t), t);

> Y2 := (t) → ff(t) + diff(Ufric(t), t, t)·evalf(int(rho·F1(x), x = 0
      ..L));

> Y3 := (x, t) → rho·diff(Ufric(t), t, t)·F3(x) − E·A·Ufric(t)
      ·diff(F3(x), x, x);

>

> B1 := eval(Y2(t))
> B2 := int(Y1(x, t)·phim(x, 1), x = 0 ..L);
> B3 := int(Y1(x, t)·phim(x, 2), x = 0 ..L);
> B4 := int(Y1(x, t)·phim(x, 3), x = 0 ..L);
> FF := Transpose(Matrix([B1, B2, B3, B4]))
> FB11 := eval(FF[1, 1], [ff(t) = 1, v(t) = 0, diff(v(t), t) = 0,
      diff(v(t), t, t) = 0 ])

> FB12 := eval(FF[1, 1], [ff(t) = 0, v(t) = 1, diff(v(t), t) = 0,
      diff(v(t), t, t) = 0 ])

> FB13 := eval(FF[1, 1], [ff(t) = 0, v(t) = 0, diff(v(t), t) = 1,
      diff(v(t), t, t) = 0 ])

> FB14 := eval(FF[1, 1], [ff(t) = 0, v(t) = 0, diff(v(t), t) = 0,
      diff(v(t), t, t) = 1 ])

> FB21 := eval(FF[2, 1], [ff(t) = 1, v(t) = 0, diff(v(t), t) = 0,
      diff(v(t), t, t) = 0 ])

> FB22 := eval(FF[2, 1], [ff(t) = 0, v(t) = 1, diff(v(t), t) = 0,
      diff(v(t), t, t) = 0 ])

> FB23 := eval(FF[2, 1], [ff(t) = 0, v(t) = 0, diff(v(t), t) = 1,
      diff(v(t), t, t) = 0 ])

> FB24 := eval(FF[2, 1], [ff(t) = 0, v(t) = 0, diff(v(t), t) = 0,
      diff(v(t), t, t) = 1 ])

> FB31 := eval(FF[3, 1], [ff(t) = 1, v(t) = 0, diff(v(t), t) = 0,
      diff(v(t), t, t) = 0 ])

> FB32 := eval(FF[3, 1], [ff(t) = 0, v(t) = 1, diff(v(t), t) = 0,
      diff(v(t), t, t) = 0 ])

> FB33 := eval(FF[3, 1], [ff(t) = 0, v(t) = 0, diff(v(t), t) = 1,
      diff(v(t), t, t) = 0 ])

> FB34 := eval(FF[3, 1], [ff(t) = 0, v(t) = 0, diff(v(t), t) = 0,
      diff(v(t), t, t) = 1 ])

> FB41 := eval(FF[4, 1], [ff(t) = 1, v(t) = 0, diff(v(t), t) = 0,
      diff(v(t), t, t) = 0 ])
```

```
> FB42 := eval(FF[4,1], [ff(t) = 0, v(t) = 1, diff(v(t), t) = 0,
      diff(v(t), t, t) = 0 ])
> FB43 := eval(FF[4,1], [ff(t) = 0, v(t) = 0, diff(v(t), t) = 1,
      diff(v(t), t, t) = 0 ])
> FB44 := eval(FF[4,1], [ff(t) = 0, v(t) = 0, diff(v(t), t) = 0,
      diff(v(t), t, t) = 1 ])
> FB := Matrix([[FB11, FB12, FB13, FB14], [FB21, FB22, FB23,
      FB24], [FB31, FB32, FB33, FB34], [FB41, FB42, FB43, FB44]]
      );
> ZZ := Matrix(4, 4, 0);
> ZI := Matrix(4, 4, shape = identity);
> with(Student[LinearAlgebra]) :
> MK1 := MatrixInverse(MM); MK := MK1.KK; MC1
      := MatrixInverse(MM); MC := MC1.CC;
> AA := Matrix(8, 8, [[ZZ, ZI], [-MK, -MC]]);
> with(LinearAlgebra) :
> IsDefinite(KK);
> IsDefinite(MM);
> Eigenvalues(AA)
> BB := Matrix(8, 1, [[0], [0], [0], [0], [evalf(MatrixInverse(MM)
      .FF)]]);
> FBB := Matrix(8, 4, [[ZZ], [evalf(MatrixInverse(MM).FB)]])
> with(DEtools) :
> sol := t→evalf(matrixDE(AA, BB, t));
>
> phimatrix := Matrix([[phim(L, 1)], [phim(L, 2)], [phim(L, 3)]]);
> phimatrix := Matrix([[phim(L, 1)], [phim(L, 2)], [phim(L, 3)]]);
> matlabFile := cat(kernelopts(datadir), "data.mat") :
> ExportMatrix(da, AA, target = Matlab, format = rectangular);
> phimatrix := Matrix([[phim(L, 1)], [phim(L, 2)], [phim(L, 3)]]);
> matlabFile := cat(kernelopts(datadir), "data.mat") :
> ExportMatrix(da, AA, target = Matlab, format = rectangular);
```

Matlab Code for Discontinuous EB Beam

```
clc
clear all
close all

kk = 1;

for tp = 0:0.0005:0.002;

L1 = 0.1;
L2 = 0.2;
L = 0.3;

Eb = 200*10^9;  % beam madule of elasticity
Ep = 50*10^9; % pzt ....

ro_b = 7800; % beam density
ro_p = 7800; % pzt density

w = 0.01;   % width of structure
tb = 0.001; %thickness of beam
tp = 0.001; %thickness of pzt


% ------------***********
% ********** ------------

I1 = 1/12*w*tb^3;
I2 = 1/12*w*(tb+tp)^3;
I3 = I1;

E1 = Eb;
E2 = Eb;
E3 = Eb;

m1 = ro_b*tb*w;
m2 = ro_b*tb*w + ro_p*tp*w;
m3 = m1;
% ------------***********
% ********** ------------

alpha = (E1*I1)/(E2*I2);
G = (E2*I2)/(E3*I3);

i = 1;
for F = 0.0001:0.001:40
    F1 = F;
```

```
    F2 = F*((m2*E1*I1)/(m1*E2*I2))^0.25;
    F3 = F*((m3*E1*I1)/(m1*E3*I3))^0.25;


M=[sin(F1*L1)-sinh(F1*L1)  cos(F1*L1)-cosh(F1*L1)  -sin(F2*L1)
-cos(F2*L1)  -sinh(F2*L1)  -cosh(F2*L1)  0  0  0  0;
F1*cos(F1*L1)-F1*cosh(F1*L1)  -F1*sin(F1*L1)-F1*sinh(F1*L1)
-F2*cos(F2*L1)  F2*sin(F2*L1)  -F2*cosh(F2*L1)  -F2*sinh(F2*L1)  0  0
0  0;
-alpha*F1^2*(sin(F1*L1)+sinh(F1*L1))
 -alpha*F1^2*(cos(F1*L1)+cosh(F1*L1))  F2^2*sin(F2*L1)  F2^2*cos(F2*L1)
-F2^2*sinh(F2*L1)  -F2^2*cosh(F2*L1)  0  0  0  0;
-alpha*F1^3*(cos(F1*L1)+cosh(F1*L1) )  alpha*F1^3*(sin(F1*L1)-
sinh(F1*L1) )  F2^3*cos(F2*L1)  -F2^3*sin(F2*L1)  -F2^3*cosh(F2*L1)
-F2^3*sinh(F2*L1)  0  0  0  0;
0  0  sin(F2*L2)  cos(F2*L2)  sinh(F2*L2)  cosh(F2*L2)  -sin(F3*L2)
-cos(F3*L2)  -sinh(F3*L2)  -cosh(F3*L2);
0  0  F2*cos(F2*L2)  -F2*sin(F2*L2)  F2*cosh(F2*L2)  F2*sinh(F2*L2)
-F3*cos(F3*L2)  F3*sin(F3*L2)  -F3*cosh(F3*L2)  -F3*sinh(F3*L2);
0  0  -G*F2^2*sin(F2*L2)  -G*F2^2*cos(F2*L2)  G*F2^2*sinh(F2*L2)
G*F2^2*cosh(F2*L2)  F3^2*sin(F3*L2)  F3^2*cos(F3*L2)  -F3^2*sinh(F3*L2)
-F3^2*cosh(F3*L2);
0  0  -G*F2^3*cos(F2*L2)  G*F2^3*sin(F2*L2)  G*F2^3*cosh(F2*L2)
G*F2^3*sinh(F2*L2)  F3^3*cos(F3*L2)  -F3^3*sin(F3*L2)  -
F3^3*cosh(F3*L2)  -F3^3*sinh(F3*L2);
0  0  0  0  0  0  -F3^2*sin(F3*L)  -F3^2*cos(F3*L)
F3^2*sinh(F3*L)  F3^2*cosh(F3*L);
0  0  0  0  0  0  -F3^3*cos(F3*L)  F3^3*sin(F3*L)
F3^3*cosh(F3*L)  F3^3*sinh(F3*L)];

deter(i) = det(M);
    beta(i) = F;
    i = i+1;
end

% ------------------------ find beta and w -------------------------

j = 1;
for i = 1:length(deter)-1
     if sign(deter(i))~= sign(deter(i+1))
         a = beta(i);
         b = deter(i);
         c = beta(i+1);
         d = deter(i+1);

         beta1(j) = a + (abs(b/d)*(c-a))/(1+abs(b/d));
         w(j) = sqrt(beta1(j)^4*E1*I1/m1);
         j = j+1;
     end
end

% -------------------------- find A B C D ------------------------
```

```
for i = 1 : length(beta1)

    F1 = beta1(i);
    F2 = F1*((m2*E1*I1)/(m1*E2*I2))^0.25;
    F3 = F1*((m3*E1*I1)/(m1*E3*I3))^0.25;

M=[sin(F1*L1)-sinh(F1*L1)  cos(F1*L1)-cosh(F1*L1)    -sin(F2*L1)
-cos(F2*L1)  -sinh(F2*L1)   -cosh(F2*L1)           0       0    0   0;
F1*cos(F1*L1)-F1*cosh(F1*L1)   -F1*sin(F1*L1)-F1*sinh(F1*L1)
-F2*cos(F2*L1)   F2*sin(F2*L1)    -F2*cosh(F2*L1)    -F2*sinh(F2*L1)
0    0    0   0;
-alpha*F1^2*(sin(F1*L1)+sinh(F1*L1) )
-alpha*F1^2*(cos(F1*L1)+cosh(F1*L1))  F2^2*sin(F2*L1)  F2^2*cos(F2*L1)
-F2^2*sinh(F2*L1)   -F2^2*cosh(F2*L1)   0   0    0   0;
-alpha*F1^3*(cos(F1*L1)+cosh(F1*L1) )    alpha*F1^3*(sin(F1*L1)-
sinh(F1*L1) )   F2^3*cos(F2*L1)   -F2^3*sin(F2*L1)     -
F2^3*cosh(F2*L1)   -F2^3*sinh(F2*L1)     0       0    0   0;
0     0     sin(F2*L2)    cos(F2*L2)     sinh(F2*L2)       cosh(F2*L2)
-sin(F3*L2)     -cos(F3*L2)      -sinh(F3*L2)      -cosh(F3*L2);
0     0     F2*cos(F2*L2)       -F2*sin(F2*L2)          F2*cosh(F2*L2)
F2*sinh(F2*L2)   -F3*cos(F3*L2)   F3*sin(F3*L2)   -F3*cosh(F3*L2)
-F3*sinh(F3*L2);
0     0   -G*F2^2*sin(F2*L2)  -G*F2^2*cos(F2*L2)   G*F2^2*sinh(F2*L2)
G*F2^2*cosh(F2*L2)   F3^2*sin(F3*L2)   F3^2*cos(F3*L2)
-F3^2*sinh(F3*L2)  -F3^2*cosh(F3*L2);
0     0   -G*F2^3*cos(F2*L2)  G*F2^3*sin(F2*L2)    G*F2^3*cosh(F2*L2)
G*F2^3*sinh(F2*L2)    F3^3*cos(F3*L2)  -F3^3*sin(F3*L2)
-F3^3*cosh(F3*L2)  -F3^3*sinh(F3*L2);
0    0    0   0   0   0   -F3^2*sin(F3*L)   -F3^2*cos(F3*L)
F3^2*sinh(F3*L)   F3^2*cosh(F3*L);
0    0    0   0   0   0   -F3^3*cos(F3*L)   F3^3*sin(F3*L)
F3^3*cosh(F3*L)   F3^3*sinh(F3*L)];

    M1 = M(1:9,1:9);
    det(M);
    b = -M(1:9,10);
    P(10,i) = 1;
    P(1:9,i) = inv(M1)*b;
end

% -------------------- find and plot mode shapes --------------------
dx = 0.0001;
x = [0:dx:L];

for i = 1 : length(beta1)
    F1 = beta1(i);
    F2 = F1*((m2*E1*I1)/(m1*E2*I2))^0.25;
    F3 = F1*((m3*E1*I1)/(m1*E3*I3))^0.25;
   for j = 1 : length(x)
       if x(j) <= L1
```

```
            phi(i,j) = P(1,i)*sin(F1*x(j)) + P(2,i)*cos(F1*x(j)) -
P(1,i)*sinh(F1*x(j)) - P(2,i)*cosh(F1*x(j));
        end
        if (x(j) > L1) & (x(j) < L2)
            phi(i,j) = P(3,i)*sin(F2*x(j)) + P(4,i)*cos(F2*x(j)) +
P(5,i)*sinh(F2*x(j)) + P(6,i)*cosh(F2*x(j));
        end
        if x(j) >= L2
            phi(i,j) = P(7,i)*sin(F3*x(j)) + P(8,i)*cos(F3*x(j)) +
P(9,i)*sinh(F3*x(j)) + P(10,i)*cosh(F3*x(j));
        end
    end
end

% ---------------------- normalization of mode shapes

for i = 1 : length(beta1)
    F1 = beta1(i);
    F2 = F1*((m2*E1*I1)/(m1*E2*I2))^0.25;
    F3 = F1*((m3*E1*I1)/(m1*E3*I3))^0.25;
    integ = 0;

    for j = 1 : length(x)
        if x(j) <= L1
            integ = integ + m1*phi(i,j)^2;
        end
        if (x(j) > L1) & (x(j) < L2)
            integ = integ + m2*phi(i,j)^2;
        end
        if x(j) >= L2
            integ = integ + m3*phi(i,j)^2;
        end
    end
    cn(i) = sqrt(inv(dx*integ));
    phi_n(i,:) = cn(i)*phi(i,:);
end

phi_n_track1(kk,:) = phi_n(1,:);
phi_n_track2(kk,:) = phi_n(2,:);
phi_n_track3(kk,:) = phi_n(3,:);
phi_n_track4(kk,:) = phi_n(4,:);
%phi_track(kk,:) = phi;
kk = kk +1;
figure(1)
plot(x,phi(3,:),'g')
plot(x,phi(1,:),'b',x,phi(2,:),'r',x,phi(3,:),'g')
hold

figure(2)
plot(x,phi_n(1,:),'b',x,phi_n(2,:),'r',x,phi_n(3,:),'g')

end
```

REFERENCES

[1] Ilic, B., Czaplewski, D., Zalalutdinov, M., Craighead, H.G., Neuzil, P., Campagnolo, C., and Batt, C., 2001, "Single Cell Detection With Micromechanical Oscillators", *Journal of Vacuum Science and Technology B*, **19** (6), pp. 2825-2828

[2] Zhang, J., and Feng, H., 2004, "An Anti E. Coli 0157*,* H7 Antibody-immobilized Microcantilever for the Detection of Escherichia Coli (E. Coli)", *Analytical Sciences,* **20**, pp. 585-587.

[3] Gupta, A., Akin, D., and Bashir, A., 2004, "Detection of Bacterial Cells and Antibodies using Surface Micromachined Thin Silicon Cantilever Resonators", *Journal of Vacuum Science and Technology B*, **22** (6), pp. 2785-2791.

[4] Gupta, A., Akin, D., and Bashir, R., 2004, "Single Virus Particle Mass Detection using Microresonators with Nanoscale Thickness", *Applied Physics Letters,* **84** (11)*,* pp. 1976-1978.

[5] Gunter, R.L., Zhine, R., Delinger, W.G., Manygoats, K., Kooser, A., and Porter, T.L., 2004, "Investigation of DNA Sensing using Piezoresistive Microcantilever Probes", *IEEE Sensors Journal,* **4** (4)*,* pp. 430-433.

[6] Su, M., Li, S., and Dravid, V., 2003, "Microcantilever Resonance-Based DNA Detection with Nanoparticle Probes", *Applied Physics Letters,* **82** (20)*,* 3562-3564.

[7] Subramanian, A., Oden, P.I., Kennel, S.J., Jacobson, K.B., Warmack, R.J., Thundat, T., and Doktycz, M.J., 2002, "Glucose Biosensing using an Enzyme-Coated Microcantilever", *Applied Physics Letters,* **81** (2)*,* pp. 385-387.

[8] Tees, D.F.J., Waugh, R.E., and Hammer, D.A., 2001, "A Microcantilever Device to Assess the Effect of Force on the Lifetime of Selectin-Carbohydrate Bonds", *Biophysical Journal,* **80***,* pp. 668–682.

[9] Lee, J.H., Kim, T.S., and Yoon, K.H., 2004, "Effect of Mass and Stress on Resonant Frequency Shift of Functionalized $Pb(Zr_{0.52}\ Ti\ _{0.48})O_3$ Thin Film Microcantilever for the Detection of C-Reactive Protein", *Applied Physics Letters,* **84** (16)*,* pp. 3187-3189.

[10] Pinnaduwage, L.A., Yi, D., Tian, F., Thundat, T., and Lareau, R.T., 2004, "Adsorption of Trinitrotoluene on Uncoated Silicon Microcantilever Surfaces", *Langmuir,* **20***,* pp. 2690-2694.

[11] Tang, Y., Fang, J., Xu, X., Ji, H.F., Brown, G.M., and Thundat, T., 2004, "Detection of Femtomolar Concentrations of HF using an SiO_2 Microcantilever", *Analytical Chemistry,* **76***,* pp. 2478-2481.

[12] Ji, H.F., Finot, E., Dabestani, R., Thundat, T., Brown, G.M., and Britt, P.F., 2000, "A Novel Self-Assembled Monolayer (SAM) Coated Microcantilever for Low Level Cesium Detection", *Chemical Communications,* **6**, pp. 457–458.

[13] Ji, H.F., Thundat, T., Dabestani, R., Brown, G.M., Britt, P.F., and Bonnesen, P.V., 2001, "Ultrasensitive Detection of CrO_4^{2-} using a Microcantilever Sensor", *Analytical Chemistry,* **73***,* pp.1572-1576.

[14] Yang, Y., Ji, H.F., and Thundat, T., 2003, "Nerve Agents Detection using a Cu^{2+}/L-Cysteine Bilayer-Coated Microcantilever", *Journal of American Chemical Society*, **125***,* pp. 1124-1125.

[15] Yan, X., Tang, Y., Ji, H., Lvov, Y., and Thundat, T., 2004, "Detection of Organophosphates using an Acetyl Cholinesterase (AChE) Coated Microcantilever", *Instrumentation Science and Technology,* **32** (2)*,* pp. 175–183.

[16] Liu, K., and Ji, H.F., 2004, "Detection of Pb^{2+} using a Hydrogel Swelling Microcantilever Sensor", *Analytical Sciences ,* **20***,* pp. 9-11.

[17] Dutta, P., Senesac, L.R., Lavrik, N.V., Datskos, P.G., and Sepaniak, M.J., 2004, "Response Signatures for Nanostructured, Optically-Probed, Functionalized Microcantilever Sensing Arrays", *Sensor Letters,* **2***,* pp. 1–8.

[18] Zhang, Y., Ji, H.F., Snow, D., Sterling, R., and Brown, G.M., 2004, "A pH Sensor-based on a Microcantilever Coated with Intelligent Hydrogel", *Instrumentation Science and Technology,* **32** (4)*,* pp. 361–369.

[19] Corbeil, J.L., Lavrik, N.V., and Rajic, S., 2002, " 'Self-Leveling' Uncooled Microcantilever Thermal Detector", *Applied Physics Letters*, **81** (7), pp. 1306-1308.

[20] Lee, C.Y., and Lee, G.W., 2003, "Micromachine-Based Humidity Sensors with Integrated Temperature Sensors for Signal Drift Compensation", *Journal of Micromechanics and Microengineering,* **13***,* pp. 620–627.

[21] Boskovic, S., Chon, J.W.M., Mulvaney, P., and Sader, J.E., 2002, "Rheological Measurements using Microcantilevers", *Journal of Rheology*, **46** (4)*,* pp. 891-899.

[22] Yinon, J., 2003, "Detection of Explosives by Electronic Noses", *Analytical Chemistry A,* **75** (5)*,* pp. 98A-105A.

[23] Thundat, T., Oden, P.I., and Warmack, R.J., 1997, "Microcantilever Sensors", *Microscale Thermophysical Engineering,* **1***,* pp. 185-199.

[24] Janata, J., 1989, "Principles of Chemical Sensors", Plenum Press, New Yourk.

[25] Bodenhofer, K., Hierlemann, A., Noetzel, G., Weimar, W., Gopel, W., 1996, "Performances of Mass-Sensitive Devices for Gas Sensing: Thickness Shear Mode and Surface Acoustic Wave Transducers", *Anal Chem*, **68**, pp. 2210-2218.

[26] Murray, RW., Dessy, RE., Heineman, WR., Janata, J., Seitz, WR., 1989, in: M. J. Comstock (Ed.), ACS Symposium Series, ACS, Washington, DC, p. 403.

[27] Carrascosa, LG., Moreno, M., Alvarez, A., Lechuga, LM., 2006, "Nanomechanical biosensors: a new sensing tool", *Trend Chem*, **25**, pp. 196-206.

[28] McFarland, A., Poggi, M., Bottomley, L., and Colton J., 2004, "Production and Characterization of Polymer Microcantilevers", *Review of Scientific Instruments,* **75** (8)*,* pp. 2756-2758.

[29] Zhang X.R, and Xua, X., 2004, "Development of a Biosensor-based on Laser-Fabricated Polymer Microcantilevers", *Applied Physics Letters*, **85** (12), pp. 2423-2425.

[30] Ji, F., 2005, "Ultrasensitive Nanomechanical Sensors for Biomedical, pharmaceutical and Biodefense Applications", http://mycenit.latech.edu/bioresearch/download/ji.ppt. (Accessed 09/12/2005).

[31] Datskos, P.G., Thundat, T., and Lavrik, N.V., 2004, "Micro and Nanocantilever Sensors", *Encyclopedia of Nanoscience and Nanotechnology,* **X***,* pp. 1–10.

[32] Chen, G.Y., Thundat, T., Wachter, E.A., and Warmack, R.J., 1995, "Adsorption-Induced Surface Stress and its Effects on Resonance Frequency of Microcantilevers", *Journal of Applied Physics,* **77** (8)*,* pp. 3618-3622.

[33] Sader, JE., 2001, "Surface stress induced deflections of cantilever plates with applications to the atomic force microscope: rectangular plates", *J Appl Phys*, **89**, 2911.

[34] Sader, JE., 2002, "Surface stress induced deflections of cantilever plates with applications to the atomic force microscope: V-shaped plates", *J Appl Phys*, **91**, 9354.

[35] Dareing, D.W., and Thundat, T., 2005, "Simulation of Adsorption-Induced Stress of a Microcantilever Sensor", *Journal of Applied Physics,* **97***,* 043526.

[36] Ren, Q., and Zhao, Y.P., 2004, "Influence of Surface Stress on Frequency of Microcantilever-based Biosensors", *Microsystem Technologies*, **10***,* pp. 307–314.

[37] Chen, G.Y., Thundat, T., Wachter, E.A., and Warmack, R.J., 1995, "Adsorption-Induced Surface Stress and its Effects on Resonance Frequency of Microcantilevers", *Journal of Applied Physics,* **77** (8)*,* pp. 3618-3622.

[38] Ziegler, C., 2004, "Cantilever-Based Biosensors", *Analytical and Bioanalytical Chemistry,* **379,** pp. 946-959.

[39] Rasmussen, P.A., Grigorov, A.V., and Boisen, A., 2005, "Double Sided Surface Stress Cantilever Sensor", *Journal of Micromechanics and Microengineering,* **15***,* pp. 1088–1091.

[40] Goeders, KM., Colton, JS., Bottomley, A., 2008, "Microcantilevers: Sensing Chemical Interactions via Mechanical Motion", *Chem Rev*, **108**, pp. 522-542.

[41] Thundat, T., and Warmack, R.J., Chen, G.Y., Allison, D.P., 1994, "Thermal and Ambient-Induced Deflections of Scanning Force Microscope Cantilevers", *Applied Physics Letters*, **64** (21), pp. 2894-2896.

[42] Liy, B.Q, Lin, J., and Wang, W., 1996, "Thermomechanical Deflection of Microcantilever Beams in Scanning Force Microscopes", *Journal of Micromechanics and Microengineering,* **6***,* pp. 330-336.

[43] Sepaniak, M., Datskos, P., Lavrik, N., and Tipple, C., 2002, "Microcantilever Transducers: A New Approach in Sensor Technology", *Analytical Chemistry,* **74** (21), pp. 568A -575A.

[44] Jalili, N., Laxminarayana, K., 2004, "A Review of Atomic Force Microscopy Imaging Systems: Application to Molecular Metrology and Biological Sciences", *Mechatronic*, **14**, pp. 907-945.

[45] Basso, M., Giarre, L., Dahleh, M., Mezic, I., 1998, "Numerical Analysis of Complex Dynamics in Atomic Force Microscopes", *Proc IEEE Conf Control Appl. Trieste, Italy, September*, pp. 1026–1030.

[46] Fung, R., Huang, S., 2001, "Dynamic Modeling and Vibration Force Microscope", *ASME J Vib Acoust*, **123**, pp. 502-509.

[47] Salapaka, M., Chen, D., 1998, "Stability and sensitivity analysis of periodic orbits in tapping mode atomic force microscopy", *Proc Conf Decision Control. Tampa FL*, pp. 2047.

[48] Noy, A., Vezenov, DV., Lieber, C., 1997, "Chemical Force Microscopy", *Annu Rev Mater Sci*, **27**, pp. 381-421.

[49] Xie, WC., Lee HP., Lim, SP., 2003, "Nonlinear Dynamic Analysis of MEMS Switches by Nonlinear Modal Analysis", *Nonlinear Dynamics,* **31**, 243–256.

[50] Mahmoodi, SN., Jalili, N., 2007, "Coupled Flexural-Torsional Nonlinear Vibrations of Piezoelecrically-actuated Microcantilevers with Application to Friction Force Microscopy", *Accepted to ASME J Vib Acoust*.

[51] Flynn, AM, Tavrow, LS., Bart, SF., Brooks, RA., Ehrlich, DJ., Udayakumar, KR., Cross, LE., 1992, "A Micromachined Sensor Array Using Thin Film Resonators", *J MEMS*, **1**, pp. 44-51.

[52] Lugienbuhl, P., Collins, SD., Racine, GA., Gretillat, MA., Rooij, NFD., Brooks, KG., Setter, N., 1998, "Ultrasons Flexural Lamb-Wave Actuators based on PZT Thin Film", *Sens Actuat A*, **64**, pp. 41-49.

[53] Xia, J., Burns, S., Porter, M., Xue, T., Liu, G., Wyse, R., Thielen, C., 1995, "A Micromachined Sensor Array Using Thin Film Resonantors", *IEEE Inter Freq Symposium*, San Francisco, pp. 879-884.

[54] Gruverman, A., Kholkin, A., 2006, "Nanoscale Ferroelectrics: Processing, Characterization and Future Trends", *Rep Prog Phys,* 69, pp. 2443-2474.

[55] Tybell, T., Paruch, P., Giamarchi, T., Triscone, J-M., 2002, "Domain Wall Creep in Epitax Ferroelectric $Pb(Zr_{0.2}Ti_{0.8})O_3$ Thin Film", *Phys Rev Lett*, **89**, pp. 097601.

[56] Terabe, K., Nakamura , M., Takekawa, S., Kitamura, K., Higuchi, S., Gotoh, Y., Cho, Y., 2003, "Microscale to Nanoscale Ferroelectric Domain and Surface Engineering of a Near Stoichiometric $LiNbO_3$ Crystal," *Appl Phys Lett*, **82**, pp. 433 – 435.

[57] Kalinin, S., Bonnell, D., Alvarez, T., Lei, X., Hu, Z., Ferris, J., 2004, "Atomic Polarization and Local Reactivity on Ferroelectric surfaces: A New Route toward Complex Nanostructures", *Nano let*, **2**, pp. 589.

[58] Kanilin, S., Karapetian, E., Kachanov, M., 2004, " Nanoelectromechanics of Piezoresponse Force Microscopy", *Physical Review B*, **70**, pp. 184101.

[59] Hong, S., Woo, J., Shin, H., Joen, J., Pak, Y., Colla, E., Settar, N., Kim, E., and No, K., 2001, "Principle of Ferroelectric Domain Imaging Using Atomic Force Microscopy", *J Appl Phys,* **89**, pp. 1377.

[60] Felten, F., Schneider, GA., 2004, "Modeling and Measurement of Surface Displacements in $BaTio_3$ Bulk Material in Piezoresponse Force Microscopy", *J Appl Phys*, **96**, pp. 563.

[61] Datskos, PG., Sauers, I., 1999, "Detection of 2-Mercaptoethanol using Gold-Coated Micromachined Cantilevers", *Sensors and Actuators B,* **61***,* pp. 75–82.

[62] Wachter, EA., Thundat, T., Oden, PI., Warmick, RJ., Datskos, PG., Sharp, SL., 1996, "Remote Optical detection using Microcantilevers", *Review of Scientific Instruments,* **67***,* pp. 3434-3439.

[63] Goedeke, SM., Allison, SW., Farahi, RH., Rajic, S., and Datskos, PG., "Dual-Fiberoptic Microcantilever Proximity Sensor", *http://www.ornl.gov/~webworks/cppr/y2001/pres/111270.pdf* (Accessed 09/12/2005).

[64] Onol, T., Esashi, M., 2004, "Mass Sensing with Resonating Ultra-Thin Silicon Beams detected by a Double-Beam Laser Doppler Vibrometer", *Measurement Science and Technology,* **15***,* pp. 1977–1981.

[65] Helm, M., Servant, JJ., Saurenbach, F., Berger, R., 2005, "Read-out of Micromechanical Cantilever Sensors by Phase Shifting Interferometry", *Applied Physics Letters,* **87***,* pp. 064101.

[66] Song, Y., Bhushan, B., 2006, "Coupling of Cantilever Lateral Bending and Torsion in Torsional Resonance and Lateral Excitation modes of Atomic Force Microscopy", *J Appl Phys,* **99**, pp. 094911.

[67] Khaled, A-RA., Vafai, K., Yang, M., Zhang, X., Ozkan, CS., 2003, "Analysis Control and Augmentation of Microcantilever Deflection in Bio-sensing Syatem", *Sens Actuat B: Chem*, **94**, pp. 103-115.

[68] Sheng, Y., Xi, N., Wejinya, UC., LI, WJ., 2004, "High Sensitivity 2-D Force Sensor for Assembly of Surface MEMS Devices", *IEEE/RSJ Conf Intell Robot Sys,* Sedai, Japan, pp. 3363-3368.

[69] Chu Duc, T., Creemer, JF., 2007, "Piezoresistive Cantilever Beam for Force Sensing in Two Dimensions", *IEEE SENSORS J*, **7**, pp. 1530.

[70] Adams, JD., Parrott, G., Bauer, C., Sant, T., Manning, L., Jones, M., Rogers, B., McCorkle, D., and Ferrell, TL., 2003, "Nanowatt Chemical Vapor detection with a Self-Sensing Piezoelectric Microcantilever Array", *Appl Phys Lett,* **83** (16)*,* pp. 3428-3430.

[71] Dosch, J. J., Inman, D. J., and Garcia, E., 1992, "A Self-Sensing Piezoelectric Actuator for Collocated Control,'' *J Intell Mater Syst Struct*, 3(1), pp. 166-185.

[72] Manalis, SR., Minne, SC., Quate, CF., 1996, "Atomic force microscopy for high speed imaging using cantilever win an integrated actuator and sensor", *Appl Phys Lett*, **68**, pp. 871.

[73] Rogers, B., Manning, L., Sulchek, T., Adams, JD., 2004, "Improving tapping mode atomic force microscopy with piezoelectric cantilevers", *Ultramicroscopy*, **100**, 267.

[74] Gurjar, M., Jalili, N., 2007, "Toward Ultra Small Mass Detection Using Adaptive Self-Sensing Piezoelectrically Driven Microcantilevers", *IEEE/ASME Transaction on Mechatronichs,* **12(6)***,* pp. 1083.

[75] Dosch, JJ., Inman, DJ., Garcia, E., 1992, "A Self-Sensing Piezoelectric Actuator for Collocated Control", *J Intel Mater Sys Struc*, **3(1)**, pp. 166-185.

[76] Mahmoo, SN., Jalili, N., 2007, "Non-linear Vibrations and Frequency Response Analysis of Piezoelectrically Driven Microcantilevers", *J Non-linear Mech*, **42(4)**, pp.577-587.

[77] Koplow, MA., Bhattacharyya, A., Mann, BP., 2006, "Closed Form Solutions for the Dynamic Response of Euler-Bernoulli Beams with Step Changes in Ccross Section", *J Sound Vib*, **295**, pp. 214-225.

[78] Martinez-Castro, AE., Museros, P., Castillo-Linares, A., 2006, "Semi-Aanalytical Solution in the Time Domain for Non-Uniform Multi-Span Bernoulli-Euler Beams Transverse by Moving Loads", *J Sound Vib*, **294**, pp. 278-297.

[79] Meirovitch, L., 1996, "Elements of Vibration Analysis", 2nd ed., *McGraw-Hill, Inc.*, New York.

[80] Bishop, R., Johnson, D., 1960, "The Mechanics of Vibration", *Cambridge University Press*, Cambridge.

[81] Krishman, A., Geetha, G., Malathi, P., 1998, "Use of Finite Difference Method in the Study of Stepped Beams", *Inter J Mech Eng Edu*, **26**, pp. 11-24.

[82] Ju, F., Lee, HP., Lee, KH., 1994, "On the Free Vibration of Stepped Beams", *Inter Solid Struc*, **31**, pp. 3125-27.

[83] Bapat, CN., Bapat, C., 1987, "Natural Frequencies of a Beam with Non-Classical Boundary Conditions and Concentrated Masses", *J Sound Vib*, **112(1)**, pp. 177-82.

[84] Naguleswaran, S., 2002, "Natural Frequencies, Sensitivity, and Mode Shape Details of an Euler–Bernoulli Beam with One-Step Change in Cross Section with Ends on Classical Supports", *J Sound Vib*, **252**, pp. 751-767.

[85] Tsukazan, T., 2005, "The Use of a Dynamical Basis for Computing the Modes of a Beam System with a Discontinuous Cross-Section", *J Sound Vib*, **281**, pp. 1175–1185.

[86] M.A. De Rosa, MA., 1994, "Free Vibration of Stepped Beams with Elastic Ends", *J Sound Vib*, **173(4)**, pp. 557-63.

[87] Popplewell, A., Daqing, C., 1996, "Free Vibrations of a Complex Euler-Bernoulli Beam", *J Sound Vib*, **190(5)**, pp. 852-6.

[88] Jang, SK., Bert, CW., 1989, "Free Vibrations of Stepped Beams: Exact and Numerical Solutions", *J Sound Vib*, **130(2)**, pp. 342-6.

[89] Levinson, M., 1976, "Vibrations of Stepped Strings and Beams", *J Sound Vib*, **49(2)**, pp. 287-91.

[90] Naguleswaran, S., 2002, "Vibration of an Euler-Bernoulli Beam on the Elastic End Supports and with up to Three Changes in Cross-Section", *Inter J Mech Sci*, **44**, pp. 2541-91.

[91] Maurini, C., Porfiri,M., Pouget,J., 2006, "Numerical Methods for Modal Analysis of Stepped Piezoelectric Beams", *J Sound Vib*, **298**, pp. 918-933.

[92] Jalili, N., Dadfarnia, M., Dawson, DM., 2004, "A Fresh Insight in to the Microcantilever-Sample Interaction Problem in Non-Contact Atomic Force Microscopy", *ASME J Dyn Sys Measur Cont*, **126**, pp. 327-335.

[93] Nagashima, N., Matsuoka, S., Miyahara, K., 1996, "Nanoscopic Hardness Measurement by Atomic Force Microscope'', *JSME Interl J, Series A: Mech Mater Eng*, **39**, pp. 456–462.

[94] Gahlin, R., Jacobson, S., 1998, "Novel Method to Map and Quantify Wear on a Micro-Scale", *Wear*, **222**, pp. 93–102.

[95] Miyahara, K., Nagashima, N., Ohmura, T., Matsuoka, S., 1999, "Evaluation of Mechanical Properties in Nanometer Scale Using AFM-based Nanoindentation Tester", *Nanostruct Mater*, **12**, pp. 1049–1052.

[96] Ziegler, C., 2004, "Cantilever-based Bbiosensors", *Anal Bioanal Chem*, **379**, pp. 946-959.

[97] Dareing, DW., Thundat, T., 2005, "Simulation of Adsorption-induced Stress of a Microcantilever Sensor", *J Appl Phys*, **97**, pp. 043526.

[98] McFarland, AW., Poggi, MA., Doyle, MJ., Bottomley, LA, Colton, JS., 2005, "Influence of Surface Stress on the Resonance Behavior of Microcantilevers", *Appl Phys Lett*, **87**, pp. 053505.

[99] Ren, Q., Zhao, Y-P., 2004, "Influence of Surface Stress on Frequency of Microcantilever-based Biosensors", *Microsyst Technol*, **10**, pp. 307–314.

[100] Wu, G., Ji, H., Hansen, K., Thundat, T., Datar, R., Cote, R., Hagan, MF., Chakraborty, AK., Majumdar, A., 2001, "Origin of Nanomechanical Cantilever Motion Generated from Bimolecular Interactions", *Proc Natl Acad Sci* , **98**, pp. 1560–1564.

[101] Braun, T., Barwich, V., Ghatkesar, MK., Bredekamp, AH., Gerber, C., Hegner, M., et al., 2005, "Micromechanical Mass Sensors for Biomolecular Detection in a Physiological Environment", *Phys Rev*, **72**, pp. 031907.

[102] Thundat, T., Warmack, RJ., Chen, GY., Allison, DP., 1994, "Thermal and Ambient-induced Deflections of Scanning Force Microscope Cantilevers", *Appl Phys Lett*, **64**, pp. 2894–8.

[103] Berger, R., Gerber, Ch., Gimzewski, JK., 1996, "Thermal Analysis using a Micromechanical Calorimeter", *Appl Phys Lett*, **69**, pp. 40–2

[104] Grigorov, AV., Davis, ZJ., Rasmussen, PA., Boisen, A., 2004, "A Longitudinal Thermal Actuation Principle for Mass Detection using a Resonant Microcantilever in a Fluid Medium", *Microelectr Eng*, **73**, pp. 881–6.

[105] Susuki, Y., 1996, "Novel Microcantilever for Scanning Thermal Imaging Microscopy", *Jpn J Appl Phys*, **35**, pp. L352–6.

[106] Majumdar, A., Lai, J., 1995, "Chandrachood M, Nakabeppu O, Wu Y and Shi Z, Thermal Imaging by Atomic Force Microscopy using Thermocouple Cantilever Probes", *Rev Sci Instr*, **66**, pp. 3584–6.

[107] Shi, L., Plyasunov, S., Bachtold, A., McEuen, PL., Majumdar, A., 2000, "Scanning Thermal Microscopy of Carbon Nanotubes using Batch-fabricated Probes", *Appl Phys Lett*, **77**, pp. 4295–7.

[108] Lee, H-C., Park, J-H., Park, Y-H.,, 2007, "Development of Shunt Type Ohmic RF MEMS Switches Actuated by Piezoelectric Cantilever", *Sensors and Actuat A*, **136**, pp. 282–290.

[109] Chu, C-H., Shih, W-P., Chung, S-Y., Tsai, H-C., Shing, T-K., Chang, P-Z., 2007, " A Low Actuation Voltage Electrostatic Actuator for RF MEMS Switch Applications", *J Micromech Microeng*, **17**, pp. 1649–1656.

[110] Jalili, N., Laxminarayana, K., 2004, "A Review of Atomic Force Microscopy Imaging Systems: Application to Molecular Metrology and Biological Sciences", *Mechatronics*, **14**, pp. 907-945.

[111] Mahmoodi, SN., Afshari, M., Jalili, N., 2008, "Nonlinear Vibrations of Piezoelectric Microcantilevers for Biologically-induced Surface Stress Sensing", *Commun Nonlinear Sci Num Sim*, 3, pp. 1964-1977.

[112] Afshari, M., Jalili, N., "Towards Non-linear Modeling of Molecular Interactions Arising from Adsorbed Biological Species on the Microcantilever Surface", *Inter J Non-linear Mech*, **42**, pp. 588-595.

[113] Hosseini, M., Jalili, N., 2007, "Thermal Effects Investigation of Microcantilevers Actuated by Boron-Nitride Nanotube", *Proceedings of SPIE*, San Diego, CA.

[114] Salehi-Khojin, A., Jalili, N., 2007, "An Analytical Modeling Framework for Piezoelectric based Microcantilever Actuator-Sensor with Consideration of Thermal Effects", *Proceedings of 2007ASME Inter Mech Eng Congress & Exposition*, Seattle, WA.

[115] Dadfarnia, M., Jalili, N., Xian, B., Dawson, DM., 2004, "A Lyapunov-based Piezoelectric Controller for Flexible Cartesian Robot Manipulators", *ASME J Dyn Sys, Measur Con*, **126**, pp. 347-358.

[116] Bashash, S., Salehi-Khojin, A., Jalili, N., 2007, "A New Framework for Modal Analysis and Forced Vibrations of Flexible Euler-Bernoulli Beams with Multiple Cross-Sectional Discontinuities", *Under review in J Sound Vib*.

[117] Matyas, J., 1965, "Random Optimization", *Automation and Remote Control*, **22**, pp. 246-253.

[118] Alexe, M., and Gruverman, A., 2004, "Nanoscale Characterization of Ferroelectric Materials", *Springer Verlag*, Berlin.

[119] Hong, S., 2003, "Nanoscale Phenomena in Ferroelectric Thin films", *Kluwer Academic Publishers*, Boston.

[120] Guthner, P., 1992, "Dransfeld K. Local Poling of Ferroelectric Polymers by Scanning Force Microscopy", *Appl Phys Lett*, **61(9)**, pp. 1137–9.

[121] Tybell, T., Paruch, P., Giamarchi, T., and Triscone, J.-M., 2002, "Domain Wall Creep in Epitax Ferroelectric $Pb(Zr_{0.2}Ti_{0.8})O_3$ Thin Film" *Phys Rev Lett*, **89**, pp. 097601.

[122] Terabe, K., Nakamura, M., Takekawa, S., Kitamura, K., Higuchi, S., Gotoh, Y., Cho, Y., 2003, "Microscale to Nanoscale Ferroelectric Domain and Surface Engineering of a Near Stoichiometric LiNbO3 Crystal," *Appl Phys Lett*, **82(3)**, pp. 433 – 435.

[123] Kalinin, S., Bonnell, D., Alvarez, T., Lei, X., Hu, Z., and Ferris, J., 2004, "Atomic Polarization and Local Reactivity on Ferroelectric surfaces: A New Route toward Complex Nanostructures", *Nano lett*, **2**, pp. 589.

[124] Kanilin, S., Karapetian, E., Kachanov, M., 2004, "Nanoelectromechanics of Piezoresponse Force Microscopy" *Physical Review B*, **70**, pp. 184101.

[125] Gruverman, A., and Kalinin, S., 2006, "Piezoresponse Force Microscopy and Recent Advances in Nanoscale Studies of Ferroelectrics", *J Mater Sci*, **41**, pp. 107-116.

[126] Guthner, P., Dransfeld, K., 1992, "Local Poling of Ferroelectric Polymers by Scanning Force Microscopy", *Appl Phys Lett*, **61**, pp. 1137.

[127] Gruverman, A., Tokumoto,H., *et al*., 1997, " Nanoscale Imaging of Domain Dynamics and Retention in Ferroelectric Thin Film", *Appl Phys Lett*, **71**, pp. 3492.

[128] Hidaka, T., Maruyama, M., *et al*., 1996, " Formation and Observation of 50 nm Polarized Domains in Pb Zr_{1-x} Ti_xO_3 Thin Filmsusing Scanning Probe Microscope", *Appl Phys Lett*, **68**, pp. 2358.

[129] Felten, F., Schneider, G., Saldana, J., and Kalinin, S., 2004, "Modeling and Measurement of Surface Displacement in $BaTiO_3$ Bulk Material in Piezoresponse Force Microscopy", *J Appl Phys*, **96(1)**, pp. 563.

[130] Hong, S., Woo, J., Shin, H., Joen, J., Pak, Y., Colla, E., Settar, N., Kim, E., and No, K., 2001, "Principle of Ferroelectric Domain Imaging Using Atomic Force Microscopy", *J Appl Phys*, **89(2)**, pp. 1377.

[131] Kalinin, S., Rodriguez, B., Jesse, S., Seal, K., Proksch, R., Hohlbauch, S., Revenko, I., Thompson, G., Vertegel, A., 2007, "Towards Local Electromechanical Probing of Cellular and Biomolecular Systems in a Liquid Environment", *Nanotechnology*, **18**, pp. 424020.

[132] Kalinin, S., Rodriguez, B., Jesse, S., Shin, J., et al, 2006, "Vector Piezoresponse Force Microscopy", *Microsc Microanal,* **12**, pp. 206-220.

[133] Papadopoulos, C.A., Dimarogonas, A.D., 1987, "Coupled Longitudinal and Bending Vibrations of a Rotating Shaft with an Open Crack", *J Sound and Vibration*, **117**, pp. 81-93.

[134] Papadopoulos, C.A., Dimarogonas, A.D., 1987, "Coupling of Bending and Torsional Vibration of a Cracked Timoshenko Shaft', *Arch Appl Mech,* **57**, pp. 257-266.

[135] Papadopoulos, C.A., Dimarogonas, A.D., 1992, "Coupled Vibration of Cracked Shafts", *J Vib Acoust*, **114**, pp. 461-467.

[136] Chasalevris, A.C., Papadopoulos, C.A., 2008, "Coupled Horizontal and Vertical Bending Vibrations of a Stationary Shaft with Two Cracks", *J Sound Vib*, **309**, pp. 507-528.

[137] Darpe, A.K., Gupta, K., Chawla, A., 2004, "Coupled Bending, Longitudinal and Torsional Vibrations of Cracked Rotor", *J Sound Vib*, **269**, pp. 33-60.

[138] Dokumaci, E., 1987, "An Exact Solution for Coupled Bending and Torsion Vibration of Uniform Beams Having Single Cross-Sectional Symmetry", *J Sound Vib*, **119**, pp. 443-449.

[139] Bishop, R.E.D., Cannon, S.M., Miao, S., 1989, "On the Coupled Bending and Torsional Vibration of Uniform Beam", *J Sound Vib*, **131**, pp. 457-464.

[140] Banerjee, J.R., Guo, S., Howson, W.P., 1996, "Exact Dynamic Stiffness Matrix of a Bending-Torsion Coupled Beam including Wraping", *Comput Struc*, **59**, pp. 612-621.

[141] Bercin, A.N., Tanaka, M., 1997, "Coupled Flexural-Torsional Vibrations of Timoshenko Beams", *J Sound Vib*, **207**, pp. 47-59.

[142] Gokdag, H., Kopmaz, O., 2005, "Coupled Bending and Torsional Vibrations of a Beam with Tip and In-Span Attachments", *J Sound Vib*, **287**, pp. 591-610.

[143] Kalinin, S., and Bonnell, D., 2002,"Imaging Mechanism of Piezoresponse Force Microscopy of Ferroelectric Surfaces", *Phys Rev*, **65**, pp. 125408.

[144] Kouno, E., 1984, "Fast response piezoelectric actuator for servo correction of systematic errors in precision machining," *CIRP Annals*, **33**, pp. 369-372.

[145] Mason, WP., 1981, "Piezoelectricity, its history and applications," *Journal of Acoustical Society of America*, **70**, pp. 1561-1566.

[146] Berlincourt, D., 1981, "Piezoelectric ceramics: characteristics and applications," *Journal of Acoustical Society of America*, **70**, pp. 1586-1595.

[147] Myers, LE., Bosenberg, WR., 1997, "Periodically poled lithium niobate and quasi-phase-matched optical parametric oscillators", *IEEE Journal of Quantum Electronics*, **33(10)**, pp. 1663-1672.